

USE OF DETACHED EDDY SIMULATION FOR AERODYNAMICS AND
AEROACOUSTICS OF BLADE SECTIONS

A THESIS SUBMITTED TO
THE GRADUATE SCHOOL OF NATURAL AND APPLIED SCIENCES
OF
MIDDLE EAST TECHNICAL UNIVERSITY

BY

KENAN CENGİZ

IN PARTIAL FULFILLMENT OF THE REQUIREMENTS
FOR
THE DEGREE OF DOCTOR OF PHILOSOPHY
IN
AEROSPACE ENGINEERING

MARCH 2018

Approval of the thesis:

**USE OF DETACHED EDDY SIMULATION FOR AERODYNAMICS AND
AEROACOUSTICS OF BLADE SECTIONS**

submitted by **KENAN CENGİZ** in partial fulfillment of the requirements for the
degree of **Doctor of Philosophy** in **Aerospace Engineering Department, Middle
East Technical University** by,

Prof. Dr. Halil Kalıpçılar
Dean, Graduate School of **Natural and Applied Sciences**

Prof. Dr. Ozan Tekinalp
Head of Department, **Aerospace Engineering**

Prof. Dr. Yusuf Özyörük
Supervisor, **Aerospace Engineering Department, METU**

Examining Committee Members:

Prof. Dr. İsmail Hakkı Tuncer
Aerospace Engineering Department, METU

Prof. Dr. Yusuf Özyörük
Aerospace Engineering Department, METU

Prof. Dr. Nafiz Alemdaroğlu
School of Civil Aviation, Atılım University

Assoc. Prof. Dr. Cüneyt Sert
Mechanical Engineering Department, METU

Assist. Prof. Dr. Sıtkı Uslu
Mechanical Engineering Department,
TOBB University of Economics and Technology

Date:

I hereby declare that all information in this document has been obtained and presented in accordance with academic rules and ethical conduct. I also declare that, as required by these rules and conduct, I have fully cited and referenced all material and results that are not original to this work.

Name, Last Name: KENAN CENGİZ

Signature :

ABSTRACT

USE OF DETACHED EDDY SIMULATION FOR AERODYNAMICS AND AEROACOUSTICS OF BLADE SECTIONS

Cengiz, Kenan

Ph.D., Department of Aerospace Engineering

Supervisor : Prof. Dr. Yusuf Özyörük

March 2018, 119 pages

Investigation of noise generation mechanisms due to turbulence necessitates resolution of eddies in space and time. Among the broad-band noise simulation tools, direct numerical simulation (DNS) is the most comprehensive one. However, it is prohibitively expensive. At the other extreme, unsteady Reynolds-averaged Navier-Stokes (URANS) based solvers, which are widely used in industry, can merely be reliable for attached flows. Besides, the inherent time-averaging procedure destroys the unsteadiness of eddies in most of the scales. Moreover, large-eddy simulation (LES) is still expensive in Reynolds numbers of industrial interest. At that point, use of hybrid RANS/LES approaches come to aid for capturing broad range of spectrum at acceptable costs. As a non-zonal variant, detached-eddy simulation (DES) has increasingly become useful in determination of noise generation mechanisms. There are commercial codes with DES modules. However, because of highly dissipative and dispersive low-order schemes of such codes, direct simulation of noise requires extremely fine meshes. Therefore, the aim of this thesis is to develop a low-dissipative low-dispersive high-order finite volume code to solve the compressible Navier-Stokes

equations with DES capability, which will enable resolving eddies that are responsible for aeroacoustic noise generation around bodies.

Thanks to an enhancement over DES, the model becomes more viable in attached flow problems, with a swifter switch to LES mode towards the outer boundary layer. Several validation studies reveal the solver's low-dissipation qualities. Finally, noise from a wing section is investigated. This is an important step towards design of quieter wind turbine blades. Ffowcs Williams and Hawkings acoustic analogy is utilized for prediction of the noise at far locations. Both the aerodynamic and aeroacoustic results show good agreements with the benchmark data, for markedly less computational cost than an LES study.

Keywords: airfoil noise, detached-eddy simulation, low dispersion, low dissipation, acoustic analogy

ÖZ

KANAT KESİTLERİNİN AERODİNAMİK VE AEROAKUSTİK İNCELENMESİNDE AYRIK ÇEVİRİNTİ BENZETİMİ

Cengiz, Kenan

Doktora, Havacılık ve Uzay Mühendisliği Bölümü

Tez Yöneticisi : Prof. Dr. Yusuf Özyörük

Mart 2018 , 119 sayfa

Türbülans kaynaklı gürültünün incelenmesi zamansal ve uzaysal bağlamda yüksek çözünürlük gerektirir. Geniş bantlı gürültü benzetimi araçlarından biri olan doğrudan sayısal benzetim (DNS) en kapsayıcı olanıdır. Ancak, yüksek çözünürlük gereksiniminden ötürü mühendislik problemlerinde kullanılamaz. Diğer uça ise sanayi tarafından yaygınca kullanılmakta olan Reynolds ortalama Navier-Stokes (RANS) yaklaşımı vardır. Onun kullanımı ise tutunan akış problemleriyle sınırlı olmakla birlikte, zaman-ortalama yaklaşımı türbülans içeriğindeki salınımları yok eder. Büyük çevrinti benzetimi (LES) ise daha mühendislik problemleri için pahalı olmayı sürdürmektedir. Bu noktada yardıma melez RANS/LES yetişir. Bu yöntem, sınır tabakayı RANS ile çözmek yoluyla, geniş bantlı bir gürültü benzetimini daha ucuza sağlayabilir. Bir melez RANS/LES yöntemi olarak ayrik çevrinti benzetimi (DES), yapılan geliştirmelerle gürültü benzetimi alanında giderek daha çok kullanılmaya başlamıştır. DES yetisi tecimsel kodlarda bulunsa da, bu kodlardaki düşük mertebeli yüksek yitimli sayısal ayriklaştırmalar çok ağ noktası gerektirmektedir. İşte bu yüzden bu çalışmanın amacı, düşük yitimli düşük dağılmalı yüksek mertebeli ve DES destekli

bir akış çözücüsü geliştirmektir. Böylece, bir nesne üzerindeki gürültü kaynaklarını oluşturan çevrintiler çözümlenebilecektir.

DES için yeni önerilmiş bir geliştirme, modeli tutunan akışlarda bile işlevsel kılmaktadır. Yapılan doğrulama çalışmaları göstermektedir ki çözücü gerçekten de düşük yitimli bir davranıştır. Ayrıca bir kanat kesidi gürültüsü problemi de çözülmüştür. Bu gibi problemlerin çözümü, rüzgar türbini kanat tasarımı çalışmalarına yönelik önemli adımlardır. Hesaplanan akış üzerinden uzaktaki gürültüyü kestirmek için Ffowcs Williams & Hawkings akustik anoloji yöntemi kullanılmıştır. Elde edilen aerodinamik ve aeroakustik sonuçlar literatürdeki deney ve benzetim verileriyle örtüşmektedir. Üstelik bu, LES yaklaşımına kıyasla çok daha ucuza getirilmektedir.

Anahtar Kelimeler: kanat gürültüsü, ayrık çevrinti benzetimi, yüksek mertebeli ayrıklaştırma, akustik anoloji

babaanneme..

ACKNOWLEDGEMENTS

First of all, I would like to thank my advisor, Dr. Yusuf Özyörük, for his guidance and support throughout the thesis work. I am also deeply thankful to him for the grant of his precious time and unlimited supply of coffee. In those times in the coffee shops, his ideas led me through the difficulties when I was stuck. The most essential guidance for me has been the time when he once said “If someone had done it, we can do it.”. I also thank Dr. İsmail H. Tuncer and Dr. Cüneyt Sert for attending my semi-annual progress meetings, where they guided me in my work with their CFD experience. I am also grateful to Dr. Alemdaroğlu and Dr. Uslu who served in my thesis defense committee. Their comments and suggestions improved my thesis further to this final state.

Computational resources granted by RÜZGEM (METUWiND) is gratefully acknowledged. Without them, this thesis would not be possible. Financial support by TÜBİTAK under the 1001 program (project grant no:112M106) received in the solver development phase of the thesis work is also acknowledged. Funding by my mother in the following phases is most gratefully acknowledged. She has literally become a great science promoter, indeed.

Buradan sonrasını ilgili kişilerin anadilinde yazıyorum. Öncelikle yıllar süren çalışmalarım boyunca desteklerini eksik etmeyip sevgileriyle bana güç veren aileme sonsuz gönül borcumu belirtmeliyim. Arkamda onlar olmadan böylesine bir risk almazdım doğrusu.

Kıvanç duyarak söylemeliyim ki yaptığım çalışmalarda arkamdan gelen, benden öğrenen, bana öğreten ve başlattıklarını sürdüren biri var: Özgür Yalçın. Çalışmalarına olan ilgisi, katkıları ve başlattıklarını sürdürüyor olması beni gönendirmekle birlikte, çalışmalarına sağladığı bu süreğenlikle, ülkedeki akademik ortamlarda çokça yaygın olan her yeni gelenin sıfırdan başlaması yanlışına karşı koymamız, tez yolunda geçen bunca sefil yıllarıma bir anlam kazandırıyor. Başarılar dilerim Özgür!

Bölümde çalıştığım zamanlarda bana şen bir ortam yaratıp yalnız olmadığımı bana gösteren Özgür H., Özgür Y., Özgür T., Özge S.Ö., Özcan, Emre, Hazal, Arda, Levent, Berk, Engin, Tansu ve daha nicesi, çok sağolun!

Kütüphanede çalışırken bana eşlik eden diğer tez sürüngen arkadaşlarım Erdem, Hande ve Erkan'a yoldaşlıkları için teşekkürler. Ayrıca Walter Benjamin'in boyun sağlığımın daha da kötüye gitmesini önlemeye yönelik desteğini unutmayacağım (betikleri bilgisayarımın altına destek oldu).

Çalışmak dışındaki zamanlarımda yakınımda olup arkadaşlıklarını esirgemeyen aşır kardeşliğinin önemini burada da vurgulamalıyım. Umutsuz zamanlarımda bolca moral veren Gönenç'i de unutmamalı. Umarım bir gün yine birlikte çalabiliriz. Ayrıca kapitan Kemal'le yaptığımız spor etkinlikleri bana hep iyi geldi. Adını yazmadığım diğer tüm sevgili arkadaşlara ve Yalçın'a da çok teşekkürler.

Son olarak, bu satırları yazdığım sırada yitirdiğimiz babaannem Neriman Cengiz'i anmak istiyorum. Tüm özverisiyle beni büyüttü, korudu ve sevdi. Bu tezi ona adıyorum.

TABLE OF CONTENTS

ABSTRACT	v
ÖZ	vii
ACKNOWLEDGEMENTS	x
TABLE OF CONTENTS	xii
LIST OF TABLES	xvi
LIST OF FIGURES	xvii
LIST OF ABBREVIATIONS	xxi
CHAPTERS	
1 INTRODUCTION	1
1.1 Motivation	1
1.2 Airfoil Self-noise	2
1.3 Detached-eddy Simulation and Its Use in Aeroacoustics	4
1.4 High-order Methods and Their Benefits on Resolving Turbulence and Noise Prediction	8
1.5 Acoustic Analogies and Prediction of the Far-field Noise	11
1.6 Overview and Accomplishments	14
2 METHODOLOGY	17
2.1 The Favre-averaged Navier-Stokes Equations	17

2.2	Fourth-order accurate low-dissipation low-dispersion finite volume method	19
2.3	Scalar Artificial Dissipation	21
2.4	Spalart-Allmaras turbulence modeling and Delayed Detached Eddy Simulation (DDES)	22
2.4.1	Standard form of the S-A model	23
2.4.2	A modification to S-A turbulence model	24
2.4.3	Zonal Detached-eddy Simulation (<i>imode</i> = 2) and Some Improvements	25
2.4.4	Shear Layer Adapted Length Scale for the DDES (SLADDES)	27
2.5	Dissipation, Dispersion and Stability Of The Numerical Scheme	29
2.6	Dual-time Stepping Strategy	34
2.7	Local Preconditioning for the Dual Time Algorithm	36
2.7.1	Low Speed Preconditioning	37
2.7.2	Determination of preconditioning parameter (ϵ)	39
2.7.3	Jacobi Preconditioning	40
2.7.4	Preconditioning Squared	41
2.7.5	Implementation of Preconditioning Squared	42
2.7.6	Blended Matrix Dissipation Form	44
2.7.7	Performance of Preconditioning Squared	44
2.8	Implicit Residual Smoothing	46
2.9	Parallelization	47
3	VERIFICATION AND VALIDATION OF THE FLOW SOLVER THROUGH BENCHMARK CASES	51

3.1	Preliminary 2-D Cases	51
3.1.1	Isentropic Vortex Convection	51
3.1.2	Inviscid transonic flow over RAE2822 airfoil	56
3.1.3	Couette flow	56
3.1.4	Laminar flow over a flat plate	58
3.1.5	Symmetric airfoil in laminar flow	58
3.1.6	Lid-driven cavity flow	60
3.1.7	Turbulent flow on flat plate	62
3.2	Code Verification in 3-D using Method of Manufactured So- lutions	63
4	UNSTEADY TURBULENT FLOW BENCHMARK PROBLEMS	65
4.1	NACA0012 airfoil at $\alpha = 45^\circ$	65
4.2	Decaying homogeneous-isotropic turbulence	67
4.3	Turbulent flow in a channel ($Re_\tau = 395$)	69
5	AEROACOUSTIC COMPUTATIONS AROUND AIRFOILS	75
5.1	Development of the Frequency-domain Ffowcs Williams-Hawkings Solver	75
5.2	Validation of the Ffowcs Williams-Hawkings Solver	78
5.2.1	A Moving Monopole Source	78
5.2.2	A Moving Dipole Source	80
5.3	Signal Processing Framework	80
5.4	Seo and Moon's Long Span Correction to Sound Pressure Levels	82
5.5	Noise Prediction from NACA0012 ($\alpha = 5.4^\circ$, $Re = 416000$, $M = 0.116$)	84

6	CONCLUSIONS	95
6.1	The Development and Validation of the Flow Solver: METUDES	95
6.2	Noise Simulation around NACA0012 Airfoil Section	97
6.3	Recommendations For Future Research	97
	REFERENCES	99
	APPENDICES	
A	VARIABLE TRANSFORMATIONS	115
	CURRICULUM VITAE	117

LIST OF TABLES

TABLES

Table 1.1 Comparison of floating point operations for discretization of a first derivative with 1% error of $\bar{k}\Delta x/k\Delta x$	9
Table 2.1 CPU time comparison for $0.24L/c$ time advancement	45
Table 4.1 Lift and drag coefficients of NACA0012, $M = 0.5$, $Re = 2 \times 10^6$, $\alpha = 45^\circ$	67
Table 4.2 Computed friction Reynolds number Re_τ with several approaches. Channel dimensions are $L_x = 2\pi H$; $L_y = 2H$; $L_z = \pi H$. The nominal value dictated by body force is $Re_\tau = 395$	71
Table 5.1 Grid configurations considered	85

LIST OF FIGURES

FIGURES

Figure 1.1 Self-noise noise sources of an airfoil in subsonic flow	3
Figure 1.2 Ratio of effective (i.e. numerical) wavenumber \bar{k} to true wavenumber k vs. number of points per wave ($NPPW = 2\pi/k\Delta x$)	9
Figure 1.3 Permeable surface around an aerodynamic body	13
Figure 2.1 Control volumes used apart from regular cell-based V_i^h	20
Figure 2.2 Comparison of the three spatial schemes: (a) effective wavenumber vs. physical wave number (b) group velocity vs. wavenumber	31
Figure 2.3 Visualizations of (a) dissipation and (b) dispersion error for combinations of different spatial and time schemes ($CFL = 1.5$).	31
Figure 2.4 Stability analysis and wave dissipation of the DRP scheme using RK4 and LDDRK6 ($\varepsilon_6 = 1/1024$).	32
Figure 2.5 Implicit backward Euler temporal scheme with fourth-order DRP spatial scheme (a) dissipation, (b) phase error.	34
Figure 2.6 Sources of convergence breakdown for Euler and Navier-Stokes equations	37
Figure 2.7 Performance comparison for a $0.1c$ span transient viscous calculation of NACA0012 case under a free stream of $M = 0.1$, $CFL = 3000$. .	46
Figure 2.8 Communication between two partitions through ghost cells.	48
Figure 2.9 Sample block decomposition.	49

Figure 2.10 Parallel speed-up curves for 1-D, 2-D and 3-D decomposition of a block with 88^3 cells.	49
Figure 3.1 Non-uniform Cartesian mesh	52
Figure 3.2 Temperature contour of the isentropic vortex using symmetry-preserving and Jameson-type schemes	54
Figure 3.3 Step-size vs. root-mean-square of differences of isentropic vortex convection solutions from analytical values of dimensionless velocities u and v , temperature, entropy.	55
Figure 3.4 Transonic flow simulation on RAE2822 airfoil ($M = 0.725$, $\alpha =$ 2.92°)	57
Figure 3.5 Couette flow simulations	58
Figure 3.6 Flat plate simulation setup	59
Figure 3.7 Blasius velocity profiles (a,b) and shear coefficient distribution (c) .	59
Figure 3.8 Grid (a), pressure coefficient (b) and residual drop (c) on NACA0012 airfoil ($M = 0.5$, $Re = 5000$)	60
Figure 3.9 Geometric centerline (a), u-velocity (b) v-velocity comparison at $Re = 100$ (25×25 grid points) and (c,d) at $Re = 1000$ (49×49 grid points) with Ghia's data	61
Figure 3.10 (a) Friction coefficient results of fine-mesh CFL3D (545×385) and the current code (69×49), (b) dimensionless boundary layer velocity and the law of the wall at $x = 0.97008$ m location	62
Figure 3.11 Full Navier-Stokes fourth-order DRP solution of the manufactured case (b) on non-uniform grid (a)	64
Figure 4.1 Mesh around NACA0012 airfoil ($193 \times 101 \times 31$ points, first cell height $y^+ \approx 1$)	66

Figure 4.2	Instantaneous views from the NACA0012 airfoil simulation (at $\alpha = 45^\circ$, $Re = 2 \times 10^6$, $M = 0.5$)	66
Figure 4.3	Lift and drag coefficients of NACA0012 vs. time ($M = 0.5$, $Re = 2 \times 10^6$, $\alpha = 45^\circ$)	67
Figure 4.4	Velocity vector field by the DNS of Wray	68
Figure 4.5	Energy spectra of an initially isotropic turbulence at three time levels: a) ++; DNS results on 512^3 grid (known as Wray1997 unpublished data set), -; current solution on 32^3 grid, ---; current solution on 64^3 grid, b) inviscid solution	68
Figure 4.6	Visualization of LES (dark region, $f_d \geq 0.8$) and RANS (light region, $f_d \leq 0.8$) zones of ZDES ($imode = 2$) at an instant at $z = 0$	71
Figure 4.7	Using SLADDES on grid $32 \times 64 \times 32$ (a) Instantaneous x -momentum field, (b) an iso-surface of Q-criterion	72
Figure 4.8	Visualization of subgrid length scale reduction in SLADDES approach on grid $32 \times 64 \times 32$	72
Figure 4.9	Dimensionless mean velocity profile (a) and Reynolds stress terms (b,c,d)	74
Figure 5.1	Ffowcs Williams-Hawkings solver integration surface for the moving dipole and monopole source tests	79
Figure 5.2	(a) Pressure signal at $R = 50l$, $\theta = 0^\circ$ and (b) directivity comparison of a monopole solution in a mean flow with $M = 0.5$	79
Figure 5.3	(a) Pressure signal at $R = 50l$, $\theta = 100^\circ$ and (b) directivity comparison of a dipole solution in a mean flow with $M = 0.5$	80
Figure 5.4	a) a sinusoidal signal (solid curve) and $1/2$ overlapping Hanning windows (dashed curves); b) corresponding filtered signal	81

Figure 5.5	<i>left</i> : asymmetric mesh setup G3 (every 2 nd point shown); <i>right</i> : Rounded trailing edge of NACA0012 (all points shown)	85
Figure 5.6	A preliminary study on coarse mesh (G1): Q-criterion ($Q = 0$) isosurface around the trailing edge using: a) ZDES, b) SLADDES	86
Figure 5.7	Isosurface of λ_2 colored by velocity magnitude (grid G3)	86
Figure 5.8	$-C_p$ (a) and C_f (b) around the airfoil	87
Figure 5.9	Dimensionless velocity profile on the suction side (grid G3)	88
Figure 5.10	Contour of $\partial p / \partial t$ around the airfoil (G3 grid)	89
Figure 5.11	a) Mean eddy viscosity contour and streamlines in the vicinity of the trailing edge, b) streamlines of the recirculation bubble obtained via LES appearing on the trailing edge	89
Figure 5.12	a) Surfaces used in FW-H acoustic analogy, b) SPL predictions on the surfaces with $\Delta f = 439.3$ Hz by an observer at $(c, 8c)$ at midspan . . .	91
Figure 5.13	a) Spanwise coherence for several frequencies; b) —: coherence length by $L_c = L_0 \exp(-A(f - f_0))$ formula, - -: corresponding SPL correction	92
Figure 5.14	Comparison of sound pressure levels at $(c, 8c)$ in third octave bands with NASA experiments and Wolf's LES+FWH results	92
Figure 5.15	Directivity at $r = 1.22$ m ($8c$) distance to the trailing edge. —: 879 Hz ($kc = 2.45$), $-\cdot-$: 2636 Hz ($kc = 7.36$), —: 5272 Hz ($kc = 14.73$)	93

LIST OF ABBREVIATIONS

CAA	Computational Aeroacoustics
CFD	Computational Fluid Dynamics
CFL	Courant–Friedrichs–Lewy
DDES	Delayed Detached-eddy Simulation
DES	Detached-eddy Simulation
DNS	Direct Numerical Simulation
DRP	Dispersion Relation Preserving
FFT	Fast Fourier Transform
FWH	Ffowcs Williams-Hawkings
IDDES	Implicit Delayed Detached-eddy Simulation
ILES	Implicit Large-eddy Simulation
LES	Large-eddy Simulation
RANS	Reynolds-averaged Navier-Stokes Equations
SA	Spalart-Allmaras
SLADDES	Shear-layer-adaptive Delayed Detached-eddy Simulation
SPL	Sound Pressure Level
URANS	Unsteady Reynolds-averaged Navier-Stokes Equations
WMLES	Wall-modeled Large-eddy Simulation
ZDES	Zonal Detached-eddy Simulation

CHAPTER 1

INTRODUCTION

1.1 Motivation

A more extensive public acceptance of wind turbines necessitates less noise emissions, which has been an issue for nearby residents since wind farms and residential areas happened to coincide because of the rapid enlargement of both such that some residents in the neighborhood complain about noise. They report that particularly under nocturnal conditions, it sounds like a never-arriving train ruining night-sleeps of the people living up to 1.5 km [1]. Evidently, the first solution to this problem that springs to mind is controlling the noise emission from the turbines. Determination of the noise sources, and designs lowering them have been a hot topic [1], particularly the aerodynamic-related noise sources are more intensely focused due to their significance. Numerical simulation using the first principles is an indispensable tool to investigate the aerodynamic noise sources around a wind turbine blade, despite the inevitable challenge of resolving complex unsteady flow structures accurately in an acceptable computation time span [2]. The turbulent character of the flow is the basis of the broadband noise [3], usually being the dominant source over blade-thickness noise, trailing-edge bluntness noise etc., particularly for larger wind turbines [4]. Broad-band noise has been simulated in three main approaches: Reynolds-averaged Navier-Stokes (RANS) based turbulence modeling [5], large/detached eddy simulation (LES/DES), and direct numerical simulation (DNS). DNS is the most general one among these, involving no turbulence model at all. However, it is impracticable for general problems due to the need for tremendous number of cells and too small time steps to resolve the whole spectrum and time scales. Nevertheless, in literature, applications of DNS appear, but usually limited to simple geometry and low Reynolds

number flows such as channel flow (for a prominent exception to this, see [6]). On the other hand, RANS based solvers can be very versatile particularly in fully-attached or shallowly-separated flow cases. They are widely used in industrial applications for a reason, indeed. Nonetheless, the inherent time-averaging procedure eliminates the unsteadiness in small scales of turbulence, which most of the time renders it inappropriate for simulation of flow noise generation. LES is a natural choice for free shear layers, with successful applications to airfoils and wind turbines [2, 7, 8]. However, feasibility of LES for mid-to-high Reynolds number boundary layer flows is still troublesome, even since the classical paper by Spalart *et al.* [9]. At that point, use of hybrid RANS/LES methods serves well both for capturing broad range of spectrum at an acceptable cost. In particular, a wall-modeled large eddy simulation (WMLES) [10] and DES in its WMLES mode [11, 12] have been the most cost-effective and user-friendly approaches towards noise simulation using first principles. In fact, they have a promising prospect towards resolving turbulent boundary layer flows for the next 20-30 years [13].

There are commercial codes like Fluent [14] which include LES/DES and RANS modules. However, because of low-order discretization approach of such codes, direct simulation of noise requires either very fine meshes or the range of the predicted noise frequency must be limited to low values because of numerical dispersion and dissipation of the waves. When high-order methods are used, such errors are lowered, and the need for very fine meshes can be relaxed. Therefore, the aim in this dissertation is to develop a high-order finite volume code to solve the Navier-Stokes equations with DES capability which will enable us to obtain turbulent vortical structures that are responsible for aeroacoustic noise generation around wind turbine blade sections. The acoustic emission due to the unsteady flow around blade sections will then be computed at observer locations using acoustic analogies.

1.2 Airfoil Self-noise

Airfoil noise is mainly due to interactions of boundary layers with the trailing edge, inflow turbulence and the resulting wake. Airfoil self-noise however, is defined as the noise without inflow turbulence or unsteadiness. That is, it is the noise the airfoil in

a smooth flow emits by itself only. Brooks *et al.* [15] identifies five flow conditions that are responsible for airfoil self-noise in subsonic regime (see Figure 1.1):

- (a) Turbulent boundary layer—trailing edge noise,
- (b) laminar boundary layer—vortex shedding noise,
- (c) separation—stall noise,
- (d) trailing edge bluntness—vortex shedding noise,
- (e) tip vortex formation noise.

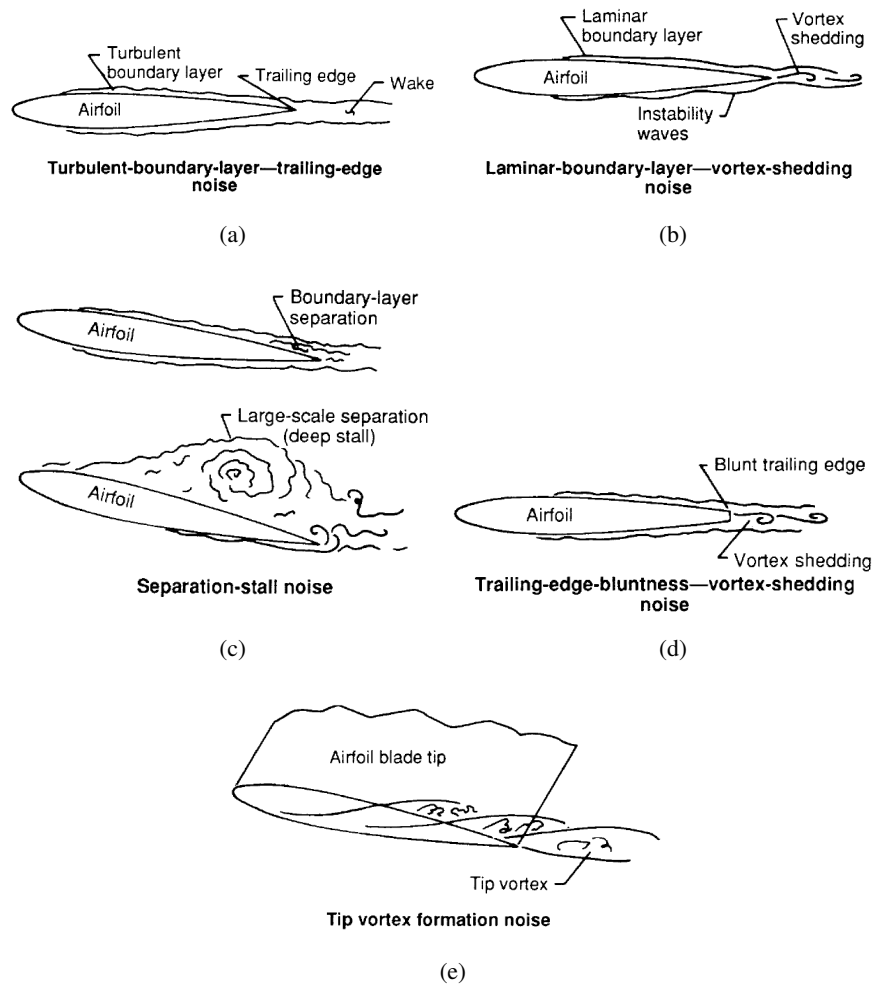


Figure 1.1: Self-noise noise sources of an airfoil in subsonic flow (reproduced from [15])

All these sources of noise are known to contribute to the broadband noise from a wing or blade. Some of the sources could be responsible for tonal noise as well (such

as (b),(d)). Prediction and control of noise from these sources are significant for airframe, fan, turbofan, helicopter rotor, and wind turbine blade designs. Conditions (a) & (b) are related to trailing edge noise, which can be described as scattering of pressure fluctuations as the unsteady boundary layers pass through the trailing edge. In fact, trailing edge noise is the primary noise source from a modern wind turbine [3].

The report by Brooks *et al.* [15], as well as more recent measurements regarding wind turbine airfoils [16, 17], documents a large set of airfoil self-noise measurements for use in development of a semi-empirical prediction model. Despite the abundance of such measurement-based models, they must be supported by numerical prediction databases to provide more detailed information of the flow. Moreover, numerical prediction is indispensable tool for understanding of the flow mechanisms behind noise control devices such as trailing-edge serrations.

Wind turbine flows are nearly incompressible, and determining the noise sources by incompressible flow equations requires special care since sound speed is infinite in such formulations. Thus, phase information throughout the scattering body is not available for non-compact sources despite its significance. In such situations, a specially tailored Green's function becomes crucial [18, 19] when describing the noise in terms of surface integral. For example in trailing-edge noise applications, solution of Ffowcs Williams-Hawkings equations necessitate the Green's function for infinite thin half-plane instead of the free-space Green's function [20, 21, 22, 23]. In the current study, however, the compressible flow equations are used, and such special treatments are not needed (see [24] as a similar approach). That is, the free-space Green's function is used in surface integral formulations.

1.3 Detached-eddy Simulation and Its Use in Aeroacoustics

Detached Eddy Simulation (DES [9]) is considered as a hybrid method such that turbulent boundary layer part of the flow (i.e. fully modeled part) is simulated with a common RANS model, and the region of interest (i.e. resolved region) with a LES-like mode of the RANS model. In fact, the RANS model equation behaves

like a Smagorinsky LES model [25] in LES mode of the DES. This behavior is observed when the production and destruction terms of the model equation are in equilibrium [26], occurring when the model length scale gets close to a LES-like grid filter. Thanks to the special length scale definition, DES smoothly switches between RANS and LES length scales. This is an automated process as opposed to other hybrid methods where a user decision is necessary to determine the RANS and LES zones. A single seamless model equation formulation between the two zones is another advantage over other hybrid RANS-LES approaches.

DES has been evolving since its introduction in 1997 [9]. Initially, it was limited to strongly separated flows, not being safe at all for use in other type of flows. The reasons for the strict limitation may be listed as below:

1. Modeled stress depletion (or grid induced separation, consequently),
2. unphysical damping of eddy viscosity in LES mode,
3. log-layer mismatch,
4. gray area problem (i.e. delay of transition to LES mode in shear layers)

Most of these shortcomings are discussed in detail by Mockett [26], and summarized by U.Michel *et al.*, P.R. Spalart and Strelets *et al.* [27, 28, 29] in their reviews.

Delayed Detached Eddy Simulation (DDES) was a significant improvement for simulation of attached flows, where boundary layers are shielded by a function to prevent early transitions caused by “ambiguous grid densities”. The shield cures the modeled stress depletion, or being an unphysical outcome, grid-induced separation is overcome as demonstrated in the work by Spalart *et al.* [30]. In the same work additionally, use of a correction function (Ψ) prevented unphysical damping by eddy viscosity caused by the low-Re functions of the RANS model being erroneously active in the LES mode. Transition to from RANS to the LES mode in the DDES framework, nevertheless, had been merely dependent on mesh because of the length scale definition Δ_{max} [30, 31], resulting in a “gray area” between the RANS and the LES region. This was remedied by the zonal hybrid RANS/LES approaches, such as [32, 33]. In these approaches, RANS and LES regions are determined a priori, and induction of

synthetic turbulence at the interface is crucial to start instabilities, i.e. to trigger LES content. Despite its success, decision burden on the interface determination (namely, the zonal approach) and quality concerns on the synthetic turbulence has been significant drawbacks [33]. Thus, they are far from being generally applicable to complex geometries, rather being “channel-friendly” [11].

Log-layer mismatch has been remedied by the improved DDES (IDDES)[11] which also handles the aforementioned issues. It features some blending functions to correct the mismatch effectively. The gray area problem is cured in the wall-modeled LES (WMLES) mode while overcoming issues (1) & (2) in the DDES mode in a blended fashion. Note that the wall modeled LES mode is active only when there is a turbulent content in the inflow, and as long as the mesh resolution in the region is close to the requirements of a LES. Despite the fact that IDDES might be considered as an overall solution to most of the listed issues, the complexity is a disadvantage. Besides, the last issue in the list remains to be solved more effectively.

A cure to the last shortcoming, delay of transition to the LES mode in shear layers, has been proposed recently by Shur *et al.* [34], and tested on several benchmark problems successfully. It merely consists of an upgrade to the vorticity aligned length scale definition Δ_ω [35, 31], combined with a function to properly reduce it locally, to obtain a shear layer adapted length scale. The new length scale definition is perceived as a reduction to eddy viscosity in regions where a purely 2-D shear is supposed to incite Kelvin-Helmholtz instabilities. Consequently the instabilities are not hampered, and LES content can arise rapidly thanks to implicit LES (ILES) nature of the model in the regions in question. The delayed detached-eddy simulation approach employing this shear layer adapted length scale definition is denoted throughout this dissertation as SLADDES for convenience. In the present study, the WMLES mode is intended to be unleashed without inlet turbulence forcing, through combining the virtues of SLADDES with minimized numerical discretization error.

Wall-modeled Large-eddy Simulation (WMLES) has been a promising research area in recent years, heralding affordable resolution of turbulence in Reynolds number ranges of engineering interests. It was estimated by Choi and Moin [36] that simulation of a high Reynolds number boundary layer flow requires a grid point num-

ber of $N \sim Re_x$ for WMLES whereas, $N \sim Re_x^{13/7}$ for wall-resolved LES, and $N \sim Re_x^{37/14}$ for resolving Kolmogorov length scale, i.e. DNS. WMLES can be considered in two categories: hybrid RANS/LES, LES with wall stress models. DES approach belongs to the former category. In the present study, only nonzonal DES approaches are considered. In the latter category, LES is solved throughout the domain without solution of any sort of RANS model equations, where the effects of walls are accounted through boundary conditions. Despite many successful applications, the robustness of the latter approach is yet to be improved in several flow complexities such as separation due to a mild adverse pressure gradient, transition, boundary layer—shock interaction, wall heat transfer. See the recent reviews [37, 38, 39] for insight into the topic, progress made and future directions.

Detached-eddy simulation methods have been increasingly employed in various noise prediction problems [40, 41, 42, 43, 44, 45], although not as common as LES methods probably because of the fact that it is not the original application area. Nevertheless, DES may well be viable in noise prediction problems as long as the shortcomings explained above are overcome to some extent. Essentially, the trait to prefer DES over LES in such problems is that DES grants the freedom to choose the range of scales that are to be resolved, unlike LES methods where the maximum grid spacing is strictly determined by standard LES requirements. In addition to the freedom in range of the scales to be resolved, DES methods also allow the user to determine the region to be resolved. For example, in mixed-type problems such as cavity noise problems, where the dominant noise sources are undoubtedly in the separated flow over the cavity, the attached flow over the wall in the upstream can conveniently be simulated in RANS mode using quite coarse meshes. All in all, DES methods enable the user to lessen computational requirements of a particular noise problem considerably, as long as the location of the noise sources and the range of the scales of the important sources are known in advance.

The main challenge for a DES user, provided the above shortcomings are remedied, is to design the grid [40]. In its LES mode, It must be fine enough to resolve small scale instabilities in shear layers. When a permeable surface is used for acoustic predictions, the grid spacing must also be sufficiently small inside the integration surface so that sound propagation is captured in all directions inside the surface. The former,

which is related with resolution and modeling of aeroacoustic sources, depends on both the turbulence modeling and the numerical scheme, whereas the latter is only related with the dissipation and dispersion characteristics of the numerical scheme. All these topics will be discussed in the next chapter.

1.4 High-order Methods and Their Benefits on Resolving Turbulence and Noise Prediction

High-order methods are not mostly available in commercial flow solvers. In industrial applications, second-order methods have been considered well-established and practical in terms of robustness, compactness, and ease of implementation. On the other hand, high-order methods, referred here to third or higher order methods, are known to be stiff, and require more floating point operations per degree of freedom as well as larger memory [46]. Nevertheless, it was reported in ADIGMA project [47] that for a given accuracy, high-order methods involved 5-10 folds fewer grid points for certain aerodynamic tests. Following the ADIGMA project, IDIHOM project [48] scrutinized industrialization of high-order methods, where highly efficient strong algorithms were considered crucial to support the cost reductions by loosened grid requirements. Despite computational cost reductions for a given accuracy, it was concluded that such methods and algorithms were not mature enough for efficient use in industrial codes.

The computational gains by using high-order methods are particularly significant in aeroacoustic noise generation and propagation studies. This may be conveniently shown by a simple Fourier analysis of a first derivative centrally discretized by finite difference method. Note that first derivative terms are common in flow equations, being mostly seen in convective terms. Figure 1.2 shows results of a Fourier analysis of centrally discretized first derivative for second, fourth, and a low-dispersion-optimized (based on DRP, explained in the next paragraph) fourth order spatial accuracy. The first impression is that, as the number of points representing one wave is reduced, the accuracy of wavenumber decreases for all of the methods. Observe that higher-order schemes have a slower decay of accuracy towards lower points per wave (NPPW), such that a selected error percentage requires more points for the second-

order spatial scheme.

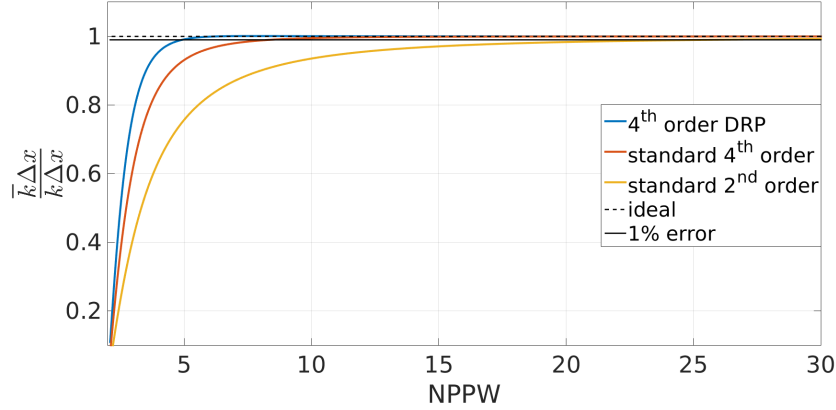


Figure 1.2: Ratio of effective (i.e. numerical) wavenumber \bar{k} to true wavenumber k vs. number of points per wave ($NPPW = 2\pi/k\Delta x$)

Table 1.1 compares the computational costs of the spatial schemes used for discretization of first derivative. The costs are shown only for 1% wave error, where corresponding number of points per wave values are extracted from Figure 1.2. The benefit of the fourth-order DRP is particularly immense on 3-D. Notice that a lower error percentage would emphasize the cost benefit of the higher order schemes even more.

Table 1.1: Comparison of floating point operations for discretization of a first derivative with 1% error of $\bar{k}\Delta x/k\Delta x$

	2^{nd} order	4^{th} order	4^{th} order DRP
NPPW required in 1-D for 1% error	25.63	8.349	4.915
FLOPS on 1-D for one point	3	5	7
FLOPS on 2-D for one point	5	9	13
FLOPS on 3-D for one point	7	13	19
FLOPS on 1-D, with 1% error	$2.24C_{1D}$	$1.21C_{1D}$	C_{1D}
FLOPS on 2-D, with 1% error	$10.5C_{2D}$	$1.20C_{2D}$	C_{2D}
FLOPS on 3-D, with 1% error	$52.2C_{3D}$	$3.35C_{3D}$	C_{3D}

In LES applications, numerical discretization errors can be at the same magnitude order with the subgrid-scale model stresses [49], ruining the work of the subgrid model.

Classically, central schemes have been recommended for LES to overcome this pitfall, instead of upwinding and flux-splitting methods. Still, sufficiency of standard second-order central scheme for LES is doubtful [50, 49]. In fact, since the standard scheme might produce spurious kinetic energy on grid non-uniformities, use of artificial diffusion is essential to ensure numerical stability, inducing some extra diffusion, which could also interfere with subgrid-scale model. In order to prevent this, one remarkable approach is to utilize the numerical dissipation error as a substitute to the subgrid scale model stresses [51, 52], hence no subgrid modeling is required. Another approach, which is adopted in the current study, is to minimize the numerical errors to eliminate the interference with the subgrid-scale models.

In standard finite volume and finite difference discretizations, local conservation of mass, momentum and total energy is ensured, while kinetic energy and internal energy (i.e. sound velocity) are not conserved by convection locally. This situation stems from the fact that the discretization operators do not retain the symmetry properties of the differential operators they are based upon [53]. In particular, from a mathematical perspective, the convective operator is skew-symmetric, and diffusive operator is positive-definite symmetric. Accordingly, to preserve the symmetry in the discrete system, the corresponding discrete operators must represent skew-symmetric and positive-definite symmetric coefficient matrices, respectively. This situation is elegantly explained by Verstappen and Veldman [53]. In inviscid cases where no change of total enthalpy is expected, unphysical generation of kinetic energy due to lack of discrete symmetry disrupts numerical stability. Besides, in viscous cases, the unphysical production or dissipation of kinetic energy could interfere with turbulent subgrid-scale stresses [54], ruining huge amount of cpu-time spent for LES. In literature, skew-symmetric forms of convective terms have been implemented for compressible or incompressible flows via finite difference formulations [55, 53, 56, 57]. They enhance stability and accuracy such that need for artificial dissipation can sometimes be eliminated unlike conventional central discretizations [57]. This is a valuable merit because of computational overhead, and possibly induced inaccuracies by the artificial dissipation. For compressible flows, Kok [54] developed a high-order scheme which locally conserves (by convection) mass, momentum and total energy without sacrificing conservation of kinetic energy, internal energy and sound velocity

locally on structured curvilinear grids with fourth-order accuracy and low-dispersive discretization. Modesti and Pirozzoli [58] developed a low-diffusion finite volume scheme for use on unstructured meshes that conserves kinetic energy on smooth flow regions and switches to AUSM flux scheme in flow discontinuities to ensure stability. Rozema *et al.* [59] developed Kok’s [54] symmetry preserving high-order method even further such that temporal discretization preserves symmetry as well as the spatial discretization. They used a new form of compressible flow equations to realize this goal. Nevertheless, the symmetry-preserving time-stepping involves solution of an implicit system, which was reported to be expensive [59]. Instead, for LES use, they made use of a regular explicit low-storage Runge-Kutta time stepping because taking small time steps keeps the error insignificant.

In this dissertation, the spatial discretization method employed is based on the fourth-order finite volume approach by Kok [54] with low dissipation and low dispersion benefits. The low-dissipation feature is based on symmetry-preserving central discretization, where skew symmetry of convective terms are preserved such that the scheme becomes energy-preserving. The low-dispersion feature comes from dispersion-relation-preserving optimization (DRP) by Tam and Webb [60], where extra points on the stencil are used for low-dispersion optimization. In fact, for large eddy simulations, and theoretically in LES regions of RANS/LES hybrid models, both features reduce numerical errors which may interfere with the subgrid-scale model [54, 49]. Note that the figures in Table 1.1 are mostly related with dispersion of waves. Avoidance from non-physical dissipation of waves is also crucial, not only because the dissipation errors may interfere with subgrid-scale models, but also because they might hinder triggering of flow instabilities [61]. Dissipation of waves by the current numerical method is scrutinized in Section 2.5.

1.5 Acoustic Analogies and Prediction of the Far-field Noise

Despite the ability to compute sound at near-field directly [8, 62], prediction of sound radiation up to an observer at a far distance directly from unsteady flow field is generally unfeasible, because propagation of sound requires impractically fine meshes (see Figure 1.2). Instead, acoustic analogies are devised and employed for sound propa-

gation simulations to far distances. Most acoustic analogies are based on Lighthill's equation [63], which is derived from Navier-Stokes equations without any special assumptions. In fact, Lighthill's equation is an inhomogeneous wave equation form of the equations of gas dynamics, in other words, an acoustic analogy is constructed from the equations of gas dynamics. Thus, a complex aeroacoustic problem is restated as a linear acoustics problem in a uniform medium, involving acoustic sources throughout the medium that would induce the same sound on the observer. Consequently, the difficulty of solving gas dynamics equations is transferred to computing of the sources. Nonetheless, clever assumptions made on the sources considering the characteristics of the flow problem have clearly paved the way for feasible far field sound prediction methodologies in industrial applications (see the reviews [64, 65, 66, 67]). The acoustic analogies are widely utilized in framework of the hybrid methods, where the acoustic sources are described by CFD, and major part of the propagation is simulated through acoustic analogies or CAA methods. In this dissertation, only Ffowcs Williams-Hawkings (FWH) acoustic analogy [68] is considered, leaving CAA tools (linearized Euler equations, acoustic splitting etc.) and other acoustic analogies out of focus. The hybrid method in focus is commonly abbreviated as CFD-FWH.

In the present work, Ffowcs Williams-Hawkings acoustic analogy is used for far field sound radiation from the turbulent flow around wing sections. It is a generalization of Lighthill's equation, exactly formulating the aeroacoustic noise due to flow around solid bodies in arbitrary motion, taking into account all sorts of sound sources. A reformulation even allows use of permeable integration surfaces [69, 70]. Proper assumptions made owing to characteristics of the flow simplifies the use of FWH equation. For example, in low-Mach constant wind speed applications, neglecting volume sources becomes handy such that sound radiation from a wing section to a far observer can be computed efficiently. In fact, volume sources are quadrupoles, and they are inefficient radiators at low speeds. This simplification is investigated by Wolf [71] extensively with two Mach numbers, through comparisons of results by computations of the volume sources included and excluded.

Figure 1.3 illustrates common use of the permeable surface encompassing the noise sources around a body. Theoretically, using the well-defined solid body surface is also

possible. However, in most cases, it is impracticable to compute volume sources (i.e. quadrupoles) in the entire 3-D flow region [72]. The permeable integration surface must enclose all the flow-acoustic interactions and flow non-uniformities for reliable aerodynamic noise computations, if such volume sources and refraction effects are non-negligible. This need was demonstrated by Singer *et al.* [73, 74] in their early work through use of various integration surfaces. Moreover, placing the surface in the surrounding uniform flow requires resolution of the acoustic waves in the frequency range of interest up to the surface [75], which could be costly in some cases, particularly those involving strong wakes. The permeable FWH formulations, without volume sources but using integration surfaces that cover all the significant sources, are considered the most efficient in general applications, such as wind turbines [2, 5], helicopter rotor noise [64], landing gear noise [76, 77], cavity noise [78], etc.

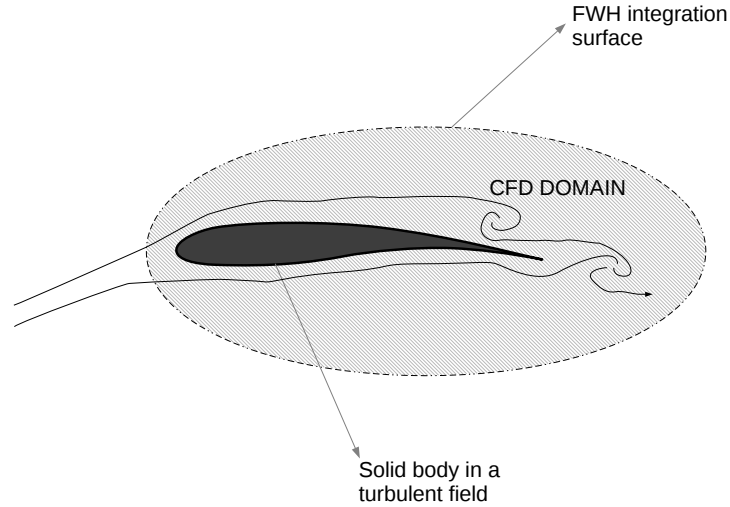


Figure 1.3: Permeable surface around an aerodynamic body

In low-Mach flows around solid bodies, neglecting the volume sources is an efficient approach because quadrupole sources are usually weak compared to loading noise sources (i.e. dipoles) [79, 66]. Nevertheless, the wakes (i.e. non-acoustic disturbances) passing through the integration surface might cause spurious noise that contaminates broadband noise computation on the far observer [75]. This is naturally expected to be canceled by the incorporation of the volume sources, which could be costly as previously discussed. In order to obviate the need for incorporation of the volume sources, several correction methods are proposed in the literature (e.g.

[72, 80]). All in all, use of acoustic analogies necessitate rigorous consideration of many issues depending on the problem characteristics.

1.6 Overview and Accomplishments

The essence of the current work is to develop from scratch a compressible flow solver called METUDES. It is designed for aeroacoustic purposes, being based on a set of advanced features and models. The set of features brought together in the framework of METUDES are listed below:

- Fourth-order low-dissipation low-dispersion spatial discretization proposed by Kok [54] on curvilinear grids,
- Dual-time strategy in time discretization combined with both low-Mach and Jacobi preconditioners (called “preconditioning squared”) by Turkel [81],
- A blended matrix dissipation form by Potsdam *et al.* [82] devised for proper scaling of artificial dissipation,
- Implicit residual smoothing for convergence acceleration,
- A positive-value-restricting modification to the Spalart-Allmaras turbulence model proposed by Crivellini *et al.* [83, 84], which is expected not only to aid in transition to turbulence, but also enhance stability of the turbulence model.
- An upgrade to the delayed detached eddy model, known as the ZDES in *imode* = 2 [31], is implemented.
- A recently proposed enhanced version of the DDES [34] is implemented which involves a smart modification to the subgrid length scale of delayed detached eddy simulation (DDES). Originally, it is referred as “shear layer adapted length scale”. In this dissertation, the model is denoted as SLADDES for convenience.
- Subgrid length scale is corrected by a factor $\bar{\Psi}$ to avoid misbehavior in the LES zone [85].
- A subroutine that generates synthetic turbulence for use as initial flow whenever necessary, due to Davidson [86, 87].

- Development of a Ffowcs-Hawkings equation solver. The efficient frequency domain formulation by Lockard [88] is implemented for 3-D surfaces, and parallelized effectively via shared memory model of OpenMP [89].

All these features are expected to aid in aeroacoustic simulations using first principles. In this study, the enhanced version of the DDES proposed by Shur *et al.* [34] (referred in the present work as SLADDES, i.e. shear layer adapted DDES) is tested and compared with the zonal DES (ZDES) by Deck [31] in its second mode, i.e. its nonzonal mode. Then, aeroacoustic investigation of an untripped airfoil is conducted using SLADDES approach. The main objective is to assess the combined effect of the high-order low-dissipation low-dispersion solver with some of the most recent DES approaches. In particular, the main contribution of this dissertation is encouragement of transition to LES mode by the non-dissipative numerical scheme and the shear layer adapted DDES model collaboratively, in order to obtain sound sources around airfoils in mid-to-high Reynolds number ranges in an affordable way.

In Chapter 2, the governing equations are presented, the numerical scheme is explained and assessed in terms of dissipation and dispersion characteristics. In Chapter 3, the methodology is validated via benchmark flow cases with simple 2-D flow configurations. Then, an intense verification of the code is made using the method of manufactured solutions. In Chapter 4, the flow solver is tested with unsteady 3-D turbulence problems, where the benefits of the numerical scheme and the turbulence closure are demonstrated. In Chapter 5, firstly, an efficient implementation of permeable Ffowcs Williams-Hawkings equation is explained and validated with analytical sources. Then, the signal processing procedure adopted is described. Lastly, flow and noise around a mid-Re airfoil is investigated using the tools gathered.

Finally, Chapter 6 summarizes and concludes the dissertation.

CHAPTER 2

METHODOLOGY

This chapter presents the theoretical background of the flow solver and implementation of the various numerical methods and models that are involved. Firstly, the governing equations are presented. Then, the spatial discretization scheme is explained briefly, followed by dispersion and dissipation characteristics of the scheme. After that, the time-integration method is constructed in a stepwise manner. Lastly, parallel implementation of the solver is described.

2.1 The Favre-averaged Navier-Stokes Equations

Since the full set of Navier-Stokes equations cannot be solved directly for engineering flow applications, contribution of small scales are filtered out to be modeled. This is done by time averaging of the flow variables, resulting in an updated set of equations with some extra terms to be modeled. For incompressible flows, Reynolds-averaged (time-averaged) Navier-Stokes equations (RANS) emerge in such an approach, whereas for compressible flow applications, Favre-averaged (density-weighted time averaged) Navier-Stokes equations are more convenient. The governing Favre-averaged equations for the fluid motion in a Cartesian coordinate system are given as

$$\frac{\partial \mathbf{Q}}{\partial t} + \frac{\partial(\mathbf{E} - \mathbf{E}_v)}{\partial x} + \frac{\partial(\mathbf{F} - \mathbf{F}_v)}{\partial y} + \frac{\partial(\mathbf{G} - \mathbf{G}_v)}{\partial z} = 0 \quad (2.1)$$

where \mathbf{Q} is the vector of the conserved variables; whereas $(\mathbf{E}, \mathbf{F}, \mathbf{G})$ and $(\mathbf{E}, \mathbf{F}, \mathbf{G})_v$ represents the convective and viscous flux terms, respectively. The terms are ex-

pressed in Favre-averaged form as

$$\begin{aligned}
\mathbf{Q} &= \begin{Bmatrix} \bar{\rho} \\ \bar{\rho}\tilde{u} \\ \bar{\rho}\tilde{v} \\ \bar{\rho}\tilde{w} \\ \bar{\rho}\tilde{E} \end{Bmatrix}, \mathbf{E} = \begin{Bmatrix} \bar{\rho}\tilde{u} \\ \bar{\rho}\tilde{u}^2 + \bar{p} \\ \bar{\rho}\tilde{u}\tilde{v} \\ \bar{\rho}\tilde{u}\tilde{w} \\ (\bar{\rho}\tilde{E} + \bar{p})\tilde{u} \end{Bmatrix}, \mathbf{E}_{\mathbf{v}} = \begin{Bmatrix} 0 \\ \bar{\tau}_{xx} \\ \bar{\tau}_{xy} \\ \bar{\tau}_{xz} \\ \bar{\tau}_{xx}\tilde{u} + \bar{\tau}_{xy}\tilde{v} + \bar{\tau}_{xz}\tilde{w} - \bar{q}_x \end{Bmatrix}, \\
\mathbf{F} &= \begin{Bmatrix} \bar{\rho}\tilde{v} \\ \bar{\rho}\tilde{v}\tilde{u} \\ \bar{\rho}\tilde{v}^2 + \bar{p} \\ \bar{\rho}\tilde{v}\tilde{w} \\ (\bar{\rho}\tilde{E} + \bar{p})\tilde{v} \end{Bmatrix}, \mathbf{F}_{\mathbf{v}} = \begin{Bmatrix} 0 \\ \bar{\tau}_{yx} \\ \bar{\tau}_{yy} \\ \bar{\tau}_{yz} \\ \bar{\tau}_{yx}\tilde{u} + \bar{\tau}_{yy}\tilde{v} + \bar{\tau}_{yz}\tilde{w} - \bar{q}_y \end{Bmatrix}, \\
\mathbf{G} &= \begin{Bmatrix} \bar{\rho}\tilde{w} \\ \bar{\rho}\tilde{w}\tilde{u} \\ \bar{\rho}\tilde{w}\tilde{v} \\ \bar{\rho}\tilde{w}^2 + \bar{p} \\ (\bar{\rho}\tilde{E} + \bar{p})\tilde{w} \end{Bmatrix}, \mathbf{G}_{\mathbf{v}} = \begin{Bmatrix} 0 \\ \bar{\tau}_{zx} \\ \bar{\tau}_{zy} \\ \bar{\tau}_{zz} \\ \bar{\tau}_{zx}\tilde{u} + \bar{\tau}_{zy}\tilde{v} + \bar{\tau}_{zz}\tilde{w} - \bar{q}_z \end{Bmatrix}, \quad (2.2)
\end{aligned}$$

where the tilde and the overbar represents Favre filtering and regular filtering of a variable, respectively. In addition, the state equation may be used to define the total energy per unit mass in terms of primitive variables

$$\tilde{E} = \frac{\bar{p}}{\bar{\rho}(\gamma - 1)} + \frac{1}{2}(\tilde{u}^2 + \tilde{v}^2 + \tilde{w}^2) \quad (2.3)$$

Finally, the shear stress tensor and the heat flux vector is calculated as

$$\bar{\tau}_{ik} = (\mu_{dyn} + \mu_{turb}) \left[\left(\frac{\partial \tilde{u}_i}{\partial x_k} + \frac{\partial \tilde{u}_k}{\partial x_i} \right) - \frac{2}{3} \delta_{ik} \frac{\partial \tilde{u}_j}{\partial x_j} \right] \quad (2.4a)$$

$$\bar{q}_k = - \left(\frac{\mu_{dyn}}{Pr(\gamma - 1)} + \frac{\mu_{turb}}{Pr_t(\gamma - 1)} \right) \frac{\partial \tilde{T}}{\partial x_k} \quad (2.4b)$$

Note here that the term (μ_{turb}) apparently is an additional term when compared with the laminar Navier-Stokes equations. In fact, it represents the effect of smaller-than-filter turbulent fluctuations. In Favre-averaged Navier-Stokes equations after necessary simplifications, it emerges as $-\rho \overline{u_i' u_j'}$ which is to be modeled to enclose the system of equations. By the Boussinesq eddy viscosity hypothesis, it is interpreted as an extra stress $\widetilde{\tau_{ij}^{turb}} = -\rho \overline{u_i'' u_j''} \approx \mu_{turb} \left[\left(\frac{\partial \tilde{u}_i}{\partial x_k} + \frac{\partial \tilde{u}_k}{\partial x_i} \right) - \frac{2}{3} \delta_{ik} \frac{\partial \tilde{u}_j}{\partial x_j} \right]$, as appears in the total stress equation (Eq.2.4).

2.2 Fourth-order accurate low-dissipation low-dispersion finite volume method

The discretization of the governing equations (Eq.2.2) is performed using finite volume method on curvilinear grids. Following Kok's methodology (see [54] for derivations and insight), the Euler equations can be defined in a special form,

$$D_i \Phi = \frac{d\rho_i \Phi_i}{dt} + \nabla_i \mathbf{F} = 0, \quad (2.5)$$

$$\text{where } \Phi_i = \begin{pmatrix} 1 \\ u_i \\ v_i \\ w_i \\ E_i \end{pmatrix}, \quad \mathbf{F} = \begin{pmatrix} \overline{\rho \mathbf{U}} \\ \overline{\rho \mathbf{U} \bar{u}} + \bar{p} \vec{i} \\ \overline{\rho \mathbf{U} \bar{v}} + \bar{p} \vec{j} \\ \overline{\rho \mathbf{U} \bar{w}} + \bar{p} \vec{k} \\ \overline{\rho \mathbf{U} \tilde{E}} + \tilde{p} \mathbf{U} \end{pmatrix}.$$

Here, the following averagings applied on faces of cells are essentially used in the derivation of the skew-symmetric forms on structured meshes,

$$\bar{u}_f = \frac{1}{2}(u_{i,j,k} + u_{i+1,j,k}) \quad (2.6a)$$

$$\widetilde{uv}_f = \frac{1}{2}(u_{i,j,k}v_{i+1,j,k} + u_{i+1,j,k}v_{i,j,k}) \quad (2.6b)$$

defined on the face between cells $V_{i,j,k}$ and $V_{i+1,j,k}$ without loss of generality. Here, the overbar and tilde has nothing to do with filtering notations used in the previous section. Notice in the averaged flux that for the sake of symmetry preservation, density goes with the convection velocity instead of ϕ in face average calculations.

Fourth-order accuracy can be achieved through use of a larger cell. Flux computations are simply done in the same manner on the grid, but with $3h$ cell size. Afterwards, the leading error term of the second-order scheme is canceled via Richardson extrapolation [53]. Eventually, the fourth-order accurate gradient operator is nothing but a linear combination of the two second-order operators. Thus, the flux balance and volume discretization can be found as,

$$B_i^{4th} = \frac{9}{8}B_i^h - \frac{1}{8 \cdot 3^d}B_i^{3h} \quad (2.7a)$$

$$V_i^{4th} = \frac{9}{8}V_i^h - \frac{1}{8 \cdot 3^d}V_i^{3h} \quad (2.7b)$$

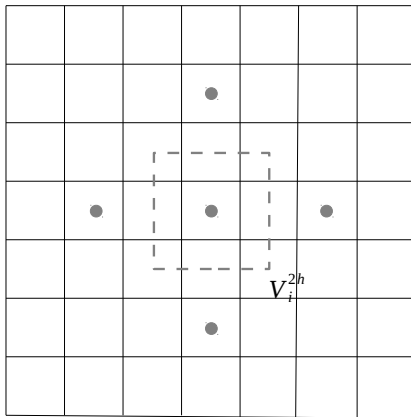
This procedure is applied to the viscous flux term as well.

Dispersion-relation preserving methodology can be devised in the same manner. Another larger cell would act as an extra degree of freedom resembling the extra points for DRP in finite difference stencils [60]. Here, since the finite volume description is cell-centered, a cell with $2h$ size has corners falling on neighboring cell centers (see Figure 2.1). Note that to maintain the fourth-order accuracy, a fourth-order accurate approximation is necessary for the metrics on the cell-centers. The fourth-order DRP discretization turns out to be a linear combination of h , $2h$ and $3h$ cell-sized second-order discretizations of volume and flux,

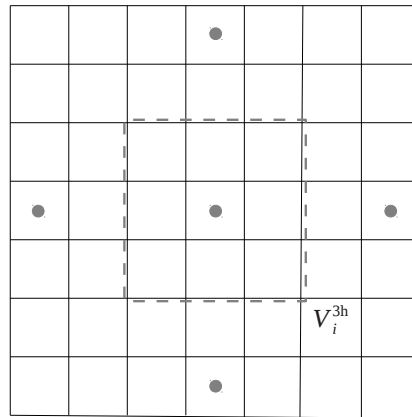
$$B_i^{DRP} = \beta \left(\frac{4}{3} B_i^h - \frac{1}{3 \cdot 2^d} B_i^{2h} \right) + (1 - \beta) \left(\frac{9}{8} B_i^h - \frac{1}{8 \cdot 3^d} B_i^{3h} \right) \quad (2.8a)$$

$$V_i^{DRP} = \beta \left(\frac{4}{3} V_i^h - \frac{1}{3 \cdot 2^d} V_i^{2h} \right) + (1 - \beta) \left(\frac{9}{8} V_i^h - \frac{1}{8 \cdot 3^d} V_i^{3h} \right) \quad (2.8b)$$

where d is the dimension of the problem. Here, taking $\beta = 0$ brings back the basic fourth-order discretization. In fact, it is the reserved parameter for optimization to achieve Tam and Webb's DRP discretization for finite difference methods. On uniform Cartesian grid, since FVM and central FDM discretizations turns out to be equivalent discrete equations, a choice of $\beta = 2.00047085298$ matches the FVM to low-dispersion optimized scheme of Tam and Webb.



(a) Control volume with $2h$ size for use in DRP.



(b) Control volume with $3h$ size for fourth-order accuracy.

Figure 2.1: Control volumes used apart from regular cell-based V_i^h

Unless otherwise is stated, time marching procedure is chosen to be the low-storage four-stage Runge-Kutta scheme [90] with fourth-order accuracy (for linear prob-

lems) and good stability behavior. Time integration lacks symmetry preserving and dispersion-relation preserving features unlike the spatial scheme. However, for an unsteady turbulent flow, the time step required already relieves the accuracy concerns when explicit time integration techniques are used.

2.3 Scalar Artificial Dissipation

The high-order scheme needs some artificial dissipation to damp spurious high-frequency waves. The classical JST dissipation model [91], which is designed for second-order cell-based finite volume schemes, is adapted here to the fourth-order scheme

$$\mathcal{L}_{AD}W_{i,j,k} = (D_\xi^2 + D_\eta^2 + D_\zeta^2 + D_\xi^6 + D_\eta^6 + D_\zeta^6)W_{i,j,k} \quad (2.9)$$

where ξ , η and ζ are the curvilinear directions. This is subtracted from the flux balance (Eq.2.8a). Notice that second-order differences (D_ξ^2 , etc.) are blended in the model for transonic flows, which is the essence of the JST scheme. In the present study, a non-dissipative discretization is used (see [92] for proof), which involves a cell-based discretization with symmetric operators. In ξ direction it reads,

$$D_\xi^4 W_{i,j,k} = \frac{\partial^2}{\partial \xi^2} \left[\lambda_{i,j,k} \epsilon_{i,j,k}^{(4)} \frac{\partial^2}{\partial \xi^2} \right] W_{i,j,k} \quad (2.10)$$

which can be adapted to the sixth difference as

$$D_\xi^6 W_{i,j,k} = \frac{\partial^2}{\partial \xi^2} \left[\lambda_{i,j,k} \epsilon_{i,j,k}^{(6)} \frac{\partial^4}{\partial \xi^4} \right] W_{i,j,k} \quad (2.11)$$

Here the derivatives are discretized by central finite difference approximations. $\epsilon^{(6)}$ and $\epsilon^{(4)}$ are constant scaling factors. λ is the eigenvalue scaling, computed from the spectral radii in all directions:

$$\lambda_\xi = |\mathbf{V} \cdot \mathbf{A}_\xi^h| + c \|\mathbf{A}_\xi^h\| \quad (2.12a)$$

$$\lambda_\eta = |\mathbf{V} \cdot \mathbf{A}_\eta^h| + c \|\mathbf{A}_\eta^h\| \quad (2.12b)$$

$$\lambda_\zeta = |\mathbf{V} \cdot \mathbf{A}_\zeta^h| + c \|\mathbf{A}_\zeta^h\| \quad (2.12c)$$

where \mathbf{V} is the velocity vector, c is sound speed and \mathbf{A}_ξ^h is the local area vector in ξ direction. An eigenvalue scaling adaptive to the mesh anisotropy is proposed by

Martinelli [93],

$$(\bar{\lambda}_\xi)_{i,j,k} = \phi_{i,j,k}(r_\eta, r_\zeta)(\lambda_\xi)_{i,j,k} \quad (2.13a)$$

$$\phi_{i,j,k}(r_\eta, r_\zeta) = 1 + (r_\eta)_{i,j,k}^\psi + (r_\zeta)_{i,j,k}^\psi \quad (2.13b)$$

where $r_\eta = \lambda_\eta/\lambda_\xi$ and $r_\zeta = \lambda_\zeta/\lambda_\xi$. The constant ψ is taken as $1/2$.

The second difference operator is useful for supplying entropy condition in shock regions and ensuring stability in stagnation points,

$$D_\xi^2 Q_{i,j,k} = \frac{\partial}{\partial \xi} \left[\lambda_{i,j,k} \epsilon_{i,j,k}^{(2)} \frac{\partial}{\partial \xi} \right] W_{i,j,k} \quad (2.14)$$

where the inner derivative is discretized using first-order accurate forward difference and the outer using backward difference. The determination of the coefficient $\epsilon_{i,j,k}^{(2)}$ differs from the classical JST scheme [91]. The classical JST pressure sensor is given as,

$$s_{JST} = \frac{|p_{i+1,j,k} - 2p_{i,j,k} + p_{i-1,j,k}|}{p_{i+1,j,k} + 2p_{i,j,k} + p_{i-1,j,k}} \quad (2.15)$$

which activates the second difference operator at high gradient regions such as shocks. In continuous regions however, since the classical JST scheme [91] does not completely switch off the second difference (with $\mathcal{O}(\Delta x^3)$ order of error), it might cause a slight interference with the high-order scheme. Instead, the following switch, proposed by Kok [94], is used

$$\epsilon_{i,j,k}^{(2)} = \min(20s_{JST}^2, s_{JST}) \quad (2.16)$$

This was shown to preserve the order of accuracy for the fourth-order scheme.

The scalar artificial dissipation formulation described here is used only when the explicit time integration is employed. On the other hand, a matrix dissipation is used with the backward implicit time integration (in the dual time framework, see Section 2.6).

2.4 Spalart-Allmaras turbulence modeling and Delayed Detached Eddy Simulation (DDES)

The closure to the Favre-averaged Navier-Stokes equations is handled using a one-equation turbulence model. The discretization of the model equation is performed via

simple second-order accurate central discretization, because it is known that high-order methods are not as robust in non-smooth regions, which is very common in turbulence model equations [46]. The non-smoothness in turbulence equation might reduce convergence speed of the entire set of flow equations. Besides, accuracy of eddy viscosity in the flow equations are not considered important, compared to the main variables in flow equations themselves.

Below, the construction of the detached-eddy model is presented stepwise.

2.4.1 Standard form of the S-A model

The one-equation turbulence model developed by Spalart and Allmaras [95] is chosen for DES purposes. The turbulence working variable transport equation is given below,

$$\frac{D\tilde{\nu}}{Dt} = \Psi + \Pi - \Phi + \Theta \quad (2.17)$$

where the diffusion, production, destruction and trip terms in standard form are defined respectively as,

$$\begin{aligned} \Psi &= \nabla \cdot \left(\frac{\nu + \tilde{\nu}}{\sigma} \nabla \tilde{\nu} \right), \quad \Pi = c_{b1}(1 - f_{t2})\tilde{S}\tilde{\nu} + \frac{c_{b2}}{\sigma} |\nabla \tilde{\nu}|^2 \\ \Phi &= (c_{w1}f_w - \frac{c_{b1}}{\kappa^2}f_{t2}) \left[\frac{\tilde{\nu}}{d_w} \right]^2, \quad \Theta = f_{t1}(\Delta u)^2 \end{aligned} \quad (2.18)$$

In this study, the trip term Θ is not used and the function f_{t2} is taken to be zero. After solving this transport equation, one can compute the turbulent viscosity through the turbulence working variable $\tilde{\nu}$, to obtain total viscosity assuming the Boussinesq hypothesis:

$$\mu_{turb} = \rho f_{v1} \tilde{\nu}, \quad f_{v1} = \frac{\chi^3}{\chi^3 + c_{v1}^3}, \quad \chi = \frac{\tilde{\nu}}{\nu}, \quad \nu = \frac{\mu_{dyn}}{\rho} \quad (2.19a)$$

$$\mu_{tot} = \mu_{dyn} + \mu_{turb} \quad (2.19b)$$

The production term follows from the modified vorticity $\tilde{S} = S + \frac{\tilde{\nu}}{\kappa^2 d_w^2} f_{v2}$ and the vorticity is $S = \nabla \times \vec{V}$. d_w is defined as the distance to the nearest wall. The remaining function is calculated as $f_{v2} = 1 - \frac{\chi}{1 + \chi f_{v1}}$. The function f_w in destruction term is found from

$$f_w = g \left[\frac{1 + c_{w3}^6}{g^6 + c_{w3}^6} \right]^{1/6}, \quad g = r + c_{w2}(r^6 - r), \quad r = \min \left(\frac{\tilde{\nu}}{\tilde{S} \kappa^2 d_w^2}, r_{max} \right) \quad (2.20)$$

The related constants are fixed as below:

$$\sigma = 2/3, \quad c_{b1} = 0.1355, \quad c_{b2} = 0.622, \quad \kappa = 0.41, \quad c_{w1} = \frac{c_{b1}}{\kappa^2} + \frac{1 + c_{b2}}{\sigma}, \quad (2.21)$$

$$c_{w2} = 0.3, \quad c_{w3} = 2, \quad c_{v1} = 7.1, \quad r_{max} = 10$$

On the wall, since there can not be turbulence, one should take $\tilde{\nu} = 0$. In fully turbulent free stream boundary, it is common to take $\tilde{\nu}$ in the order of ν_∞ to continuously supply turbulent flow, whereas $\tilde{\nu} \ll 0.1\nu_\infty$ is necessary under tripped conditions. Eventually, the model equation is closed. Hence, total shear stress and total heat flux in filtered form are computed as,

$$\bar{\tau}_{ik} = (\mu_{dyn} + \mu_{turb}) \left[\left(\frac{\partial \tilde{u}_i}{\partial x_k} + \frac{\partial \tilde{u}_k}{\partial x_i} \right) - \frac{2}{3} \delta_{ik} \frac{\partial \tilde{u}_j}{\partial x_j} \right] \quad (2.22a)$$

$$\bar{q}_k = - \left(\frac{\mu_{dyn}}{Pr(\gamma - 1)} + \frac{\mu_{turb}}{Pr_t(\gamma - 1)} \right) \frac{\partial \tilde{T}}{\partial x_k} \quad (2.22b)$$

In most cases, turbulent heat transfer corresponds to a turbulent Prandtl number of $Pr_t = 0.9$.

2.4.2 A modification to S-A turbulence model

The above form is designated as the standard form [96]. A recent modification by [83, 84] is designed as a cure for negative $\tilde{\nu}$ values through simply avoiding negative-valued computations and withcoming numerical difficulties. The source term, $\Pi - \Phi$ of the convection equation is rearranged and redefined as,

$$\Pi - \Phi = \begin{cases} \left[(1 - f_{t2}) \frac{c_{b1}}{\kappa^2 r} - c_{w1} f_w + f_{t2} \frac{c_{b1}}{\kappa^2} \right] \left(\frac{\tilde{\nu}}{d_w} \right)^2 + \frac{c_{b2}}{\sigma} |\nabla \tilde{\nu}|^2 & \tilde{\nu} \geq 0 \\ 0 & \tilde{\nu} < 0 \end{cases} \quad (2.23)$$

and the diffusion term is modified to be

$$\Psi = \nabla \cdot \left(\frac{\nu + \max[\tilde{\nu}, 0]}{\sigma} \nabla \tilde{\nu} \right) \quad (2.24)$$

In addition, the function r is redefined as

$$r^* = \left(\frac{S \kappa^2 d_w^2}{\tilde{\nu}} + f_{v2} \right)^{-1} \quad (2.25a)$$

$$r = \begin{cases} r_{max} & r^* < 0 \\ \min(r^*, r_{max}) & r^* \geq 0 \end{cases} \quad (2.25b)$$

Last but not the least, the evaluation of turbulent viscosity is limited to positive values as well,

$$\mu_{turb} = \rho f_{v1} \max(\tilde{\nu}, 0) \quad (2.26)$$

all the remaining functions and constants being kept as they are. It was reported [84] that this modification has an apparent transition behavior, essentially in case of flows with laminar separation. For attached flows however, transition must be induced in other ways. In this study, transition is expected to be realized via DDES and triggered through induction of synthetic turbulence upon the initial or inlet conditions. Note also that the laminar suppression term f_{t2} is ignored.

The DES approaches in the following sections are both based on this modified form of SA equation.

2.4.3 Zonal Detached-eddy Simulation ($imode = 2$) and Some Improvements

Detached-eddy Simulation, in a crude explanation, is switching from RANS mode to LES mode away from a wall boundary, and keeping in RANS mode near the wall. Thanks to implicit filtering of the Navier-Stokes equations, implementation of the model solely necessitates the switch for the model length scale, where RANS model acts like a LES subgrid model away from the wall surface. In the original detached-eddy simulation (known as DES97), the switch is defined by [9],

$$l_{DES97} = \min(l_{RANS}, l_{LES}) \quad (2.27)$$

where the length scales of the SA-RANS and LES modes are defined as $l_{RANS} = d_w$, $l_{LES} = C_{DES}\Delta$, respectively. Here, Δ can be perceived as a LES filter width with the conventional DES definition being maximum grid distance in three directions, i.e. $\Delta = \max(\Delta_1, \Delta_2, \Delta_3)$. C_{DES} is a coefficient to be calibrated.

Delayed Detached Eddy Simulation is a modification to the regular DES which tunes RANS-LES switching [85], by forcing to keep in RANS mode inside boundary layers. In fact, for many cases it overcomes the modeled stress depletion and the grid induced separation problems of DES97 [85, 97]. The implementation is done by

simply replacing the RANS length scale (d_w in the case of SA-DDES) with

$$l_{DDES} = l_{RANS} - f_d \max(0, l_{RANS} - l_{LES}) \quad (2.28)$$

where

$$l_{RANS} = d_w \quad (2.29)$$

$$l_{LES} = C_{DES} \Delta \quad (2.30)$$

$$f_d = 1 - \tanh([8r_d]^3) \quad (2.31)$$

$$r_d = \frac{\nu_t + \nu}{(U_{i,j} U_{i,j})^{0.5} \kappa^2 d_w^2} \quad (2.32)$$

The coefficient $C_{DES} = 0.65$ has been set as a calibration based on decaying isotropic turbulence. Here, the classical DDES takes the subgrid length-scale as $\Delta = \Delta_{max} = \max(\Delta_1, \Delta_2, \Delta_3)$. A known weakness of DDES is that development of instabilities are delayed because of damping effects of the RANS model, such that transition to LES mode is not quick enough [98]. This phenomenon, named as the gray area problem, is overcome in zonal DES (ZDES in $imode = 2$) approach [98, 31] through assigning LES-like grid spacing function, $\Delta_{vol} = (\Delta_1 \Delta_2 \Delta_3)^{1/3}$ above a pre-determined $f_{d0} = 0.8$, which roughly marks the edge of the boundary layer. Furthermore, the subgrid length-scale function in this region can be replaced with an improvement defined by [35],

$$\Delta_\omega = \sqrt{N_1^2 \Delta_2 \Delta_3 + N_2^2 \Delta_1 \Delta_3 + N_3^2 \Delta_1 \Delta_2} \quad (2.33)$$

where $\mathbf{N} = \frac{\vec{\omega}}{||\vec{\omega}||}$ is the unit vector aligned with the vorticity vector. Such a formulation does not only depend on the mesh, but also on the flow variables.

Another improvement to the DDES model is “the extended” DDES (EDDES), which mainly follows ZDES approach. It is designed to combine best features of DDES and ZDES. The sole improvement on ZDES ($imode = 2$) is assigning the near-wall functions of the S-A model to their asymptotic values in the LES zone,

$$f_{v1} = 1, \quad f_{v2} = 0, \quad f_w = 1 \quad (2.34)$$

in an attempt to ease the transition to LES mode and to cure the gray area problem. Equating the near-wall functions (i.e. the low-Re terms) in LES mode to their asymptotic values disables the low-Re influences on the subgrid model. However, this causes a discontinuity of the turbulence viscosity on the LES-RANS interface. It

is reported that this modification may corrupt the boundary layer [31] despite all the reports demonstrating its success [99, 100, 101, 102]. In this study, a correction to the subgrid length-scale $l_{LES} = C_{DES}\Psi\Delta$ (see Eq. (2.28), (2.30)), proposed by Spalart *et al.* [85], is used instead. The function Ψ is derived as,

$$\Psi^2 = \min \left[10^2, \frac{1 - \frac{c_{b1}}{c_{w1}\kappa^2 f_w^*} [f_{t2} + (1 - f_{t2})f_{v2}]}{f_{v1} \max(10^{-10}, 1 - f_{t2})} \right] \quad (2.35)$$

This procedure is applied to DDES by Travin *et al.* within the concept of hybrid modeling [103]; and by Shur *et al.* in “improved DDES” (IDDES) approach [11]. It is shown that the modification eliminates the low-Re terms of the RANS model in the LES zone, and unlike EDDES approach, it provides a smooth transition for the terms in the interface.

Note that in the current study, zonal DES is not fully utilized because zonal features are not used at all. In fact, only $imode = 2$ is employed throughout all domains. Determining various zones and assigning proper model modes would require an extra decisive making burden for the user, which is not desired most of the time, owing mostly to the fact that an improper or mistaken assignment may mislead the solver to undesired results.

2.4.4 Shear Layer Adapted Length Scale for the DDES (SLADDES)

A recently proposed remedy by Shur *et al.* [34] to delay of transition from RANS to LES mode is implemented as well. It consists of redefinition of the length scale not only depending on the vorticity but also three-dimensionality of the local flow. Firstly, the vorticity dependent length scale definition given in Eq. 2.33 is improved further:

$$\tilde{\Delta}_\omega = \frac{1}{\sqrt{3}} \max_{n,m=1,8} |\mathbf{I}_n - \mathbf{I}_m| \quad (2.36)$$

where $\mathbf{I}_n = \mathbf{n}_\omega \times \mathbf{r}_n$ and \mathbf{n}_ω is the unit vorticity vector. \mathbf{r}_n is the position vector for the vertices of the cell ($n = 1, ..8$ for hexahedral cells). This formulation removes dependency of subgrid viscosity on cell length (mostly $\Delta_{max} = \Delta z$ for a shear layer in xy plane) in vorticity direction, which had been a problem in shear layers where the planar shear is expected to initiate transition to the LES mode. Instead, the sub-grid viscosity is based on the maximum dimension on the shear plane in a quasi-2D

region. Still, the resulting reduction of the subgrid viscosity is not sufficient to initiate the transition in quasi-2D regions. An ILES-like behavior is desired in such regions to allow Kelvin-Helmholtz instabilities to take over. The so-called ‘‘Vortex Tilting Measure’’ is defined to detect such regions,

$$VTM = \frac{\sqrt{6}|(\hat{\mathbf{S}} \cdot \boldsymbol{\omega}) \times \boldsymbol{\omega}|}{\omega^2 \sqrt{3tr(\hat{\mathbf{S}}^2) - [tr(\hat{\mathbf{S}})]^2}} \quad (2.37)$$

It yields zero when the vorticity is aligned with any eigenvectors of the strain; nonzero when the deformation tensor tilts the vorticity vector. VTM is facilitated in the function

$$F_{KH}(\langle VTM \rangle) = \max \left[F_{KH}^{min}, \min \left\{ F_{KH}^{max}, F_{KH}^{min} + \frac{F_{KH}^{max} - F_{KH}^{min}}{a_2 - a_1} (\langle VTM \rangle - a_1) \right\} \right] \quad (2.38)$$

where the angle brackets, $\langle \cdot \rangle$, means the value is averaged among neighboring cells. Averaging is necessary for smoothing the distribution since it is reported that VTM may have downward excursions locally. F_{KH} function is a simplistic function depending on VTM with the sole purpose of reducing the subgrid viscosity properly. $F_{KH}^{max} = 1$ recovers the original length scale while $F_{KH}^{min} = 0.1$, and $a_1 = 0.15$, $a_2 = 0.3$ are constants adjusted through numerical experiments. Accordingly, F_{KH} varies linearly between $\langle VTM \rangle = 0.15$ and $\langle VTM \rangle = 0.3$ yielding values ranging from 0.1 to 1. Hence, the ultimate subgrid length scale is calculated by

$$\Delta_{SLA} = \tilde{\Delta}_\omega F_{KH}(\langle VTM \rangle) \quad (2.39)$$

The resulting length scale serves as a reduction to the vorticity-oriented length scale, $\tilde{\Delta}_\omega$, by up to one order in regions where Kelvin-Helmholtz instabilities are expected to occur, thus leaving ground to transition to resolved 3-D turbulent mode. However, for wall bounded flows, this reduction should be inactivated to keep the boundary layer shielded as done in standard DDES with Δ_{max} . The following limitation to F_{KH} is proposed for that purpose,

$$F_{KH}^{lim} = \begin{cases} 1.0 & f_d < 0.99 \\ F_{KH} & f_d \geq 0.99 \end{cases} \quad (2.40)$$

As a result, this version of DDES has proven success (by Shur *et al.* [34]) not only in free shear layers, but also in wall bounded flows, jet flows, decaying turbulence and backward facing step flows.

The set of features brought together in this work from the aforementioned DES modes are listed below:

- A stabilizing modification to the Spalart-Allmaras turbulence equation,
- An upgrade to the delayed detached eddy simulation model, known as the ZDES in $imode = 2$ [31], is implemented. Moreover, roughly outside the boundary layer ($f_d > 0.8$), a vorticity aligned subgrid length scale, denoted as Δ_ω (see Eq. (2.33)), is chosen instead of Δ_{vol} of the original ZDES($imode = 2$).
- A recently proposed enhanced version of the DDES [34] is implemented, denoted here as SLADDES.
- Subgrid length scale is corrected by a factor Ψ to avoid misbehavior in the LES zone.

2.5 Dissipation, Dispersion and Stability Of The Numerical Scheme

Dispersion and dissipation characteristic can be examined using the 1-D linear advection equation as a model equation,

$$\frac{\partial u}{\partial t} + a \frac{\partial u}{\partial x} = 0 \quad (2.41)$$

where a is a constant wave speed. Since (fourth-order) central differencing schemes will be used, to stabilize when necessary, an artificial dissipation term is included for filtering spurious short waves,

$$\frac{\partial u}{\partial t} + a \frac{\partial u}{\partial x} - \varepsilon_6 \frac{a}{\Delta x} \frac{\partial^6 u}{\partial \xi^6} = 0 \quad (2.42)$$

where the dissipation coefficient is a constant, commonly taken as $\varepsilon_6 = 1/512$ for a fourth-order accurate scheme. ξ is the correspondence to x in computational domain such that $\Delta \xi = 1$. In wavenumber space, spatial derivative transfer functions of the

standard second, fourth-order, fourth-order DRP and the artificial dissipation terms are found by taking $u_j^{(n)} = \tilde{u} \exp [i(kx_j - kat^{(n)})]$,

$$D_{2nd} = u_j^{(n)} (-\exp(-ik\Delta x) + \exp(ik\Delta x)) / (2\Delta x) \quad (2.43a)$$

$$D_{4th} = u_j^{(n)} (-\exp(2ik\Delta x) + 8\exp(ik\Delta x) - 8\exp(-ik\Delta x) + \exp(-2ik\Delta x)) / (12\Delta x) \quad (2.43b)$$

$$D_{DRP} = u_j^{(n)} (c_{-3} \exp(-3ik\Delta x) + c_{-2} \exp(-2ik\Delta x) + c_{-1} \exp(-ik\Delta x) + c_{+1} \exp(ik\Delta x) + c_{+2} \exp(2ik\Delta x) + c_{+3} \exp(3ik\Delta x)) / \Delta x \quad (2.43c)$$

$$D_{AD} = \frac{\varepsilon_6 a}{\Delta x} u_j^{(n)} (\exp(-3ik\Delta x) - 6\exp(-2ik\Delta x) + 15\exp(-ik\Delta x) - 20 + 15\exp(ik\Delta x) - 6\exp(2ik\Delta x) + \exp(3ik\Delta x)) / \Delta \xi^6 \quad (2.43d)$$

where the optimizing coefficients c_{-3}, c_{-2}, \dots are calculated by Tam [104]. Figure 2.2a shows the deviation of the effective wavenumber $\bar{k}\Delta x$ of the spatial scheme from the true wavenumber in Fourier space, whereas Figure 2.2b shows the group velocity (concept used by Tam *et al.* [105]) of the three spatial schemes considered. Thus, it is obvious that the fourth-order DRP scheme for the first derivative outperforms.

Applying a compact m-stage Runge-Kutta time integration, in wavenumber space the solution in next time level is found as,

$$\begin{aligned} \tilde{u}_{(0)} &= \tilde{u}^{(n)} \\ \tilde{u}_{(s)} &= \tilde{u}^{(n)} - \alpha_{(s)} \sigma (D_{DRP}(\tilde{u}_{(s-1)}) - D_{AD}(\tilde{u}_{(0)})) \Delta x; \quad s = 1, m \\ \tilde{u}^{(n+1)} &= \tilde{u}_{(m)} \end{aligned}$$

where $\sigma = a\Delta t / \Delta x$ is the CFL number. Effect of spatial discretization scheme together with the time integration can be monitored by changing the discrete differential operator (D_{DRP} , D_{4th} or D_{2nd}) and the m-stage low-storage Runge-Kutta constants ($\alpha_{(s)}$; $s = 1, m$). For the linear advection equation advects waves as they are, all the magnitudes and speeds of the waves are expected to be preserved. Hence, the dissipation and phase error after one time step can be computed using this exact solution in wave space. For a fixed $CFL = 1.5$, the resulting dissipation and dispersion error can be seen from Figure 2.3. Despite the fact that the discrete derivative using the

DRP scheme surpasses the standard one (see Figure 2.2), it only thrives when used with a low-dispersion low-dissipation time integration method (LDDRK6 [106]), and vice versa. For instance, observe that the second-order scheme performs similarly with both time integration methods under the present conditions.

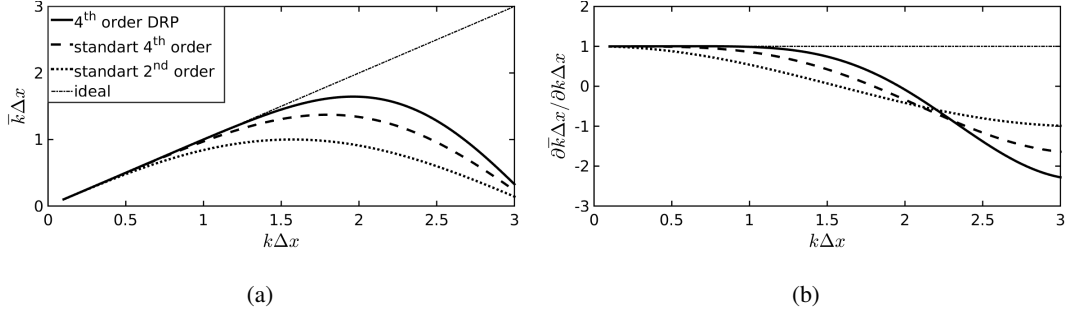


Figure 2.2: Comparison of the three spatial schemes: (a) effective wavenumber vs. physical wave number (b) group velocity vs. wavenumber

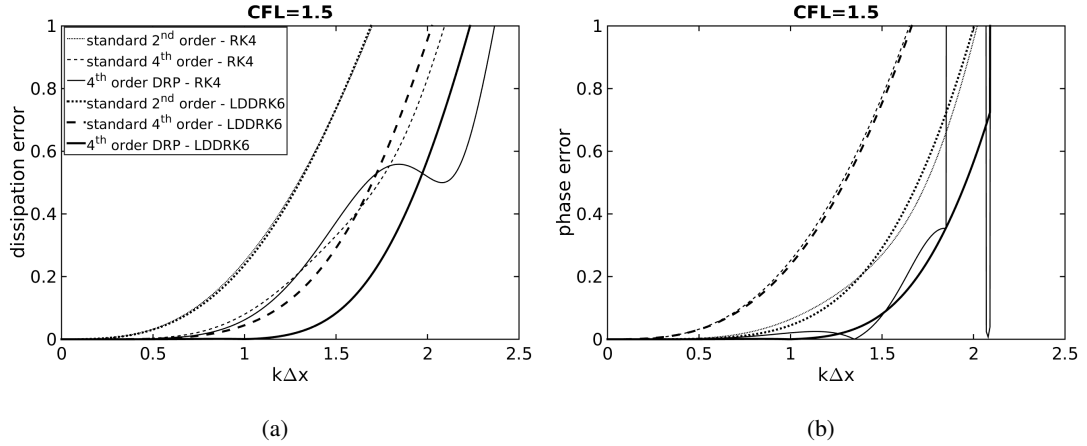


Figure 2.3: Visualizations of (a) dissipation and (b) dispersion error for combinations of different spatial and time schemes ($CFL = 1.5$).

Figure 2.4 illustrates dissipation impact of the DRP scheme using two time integration methods, with a small amount of artificial dissipation $\varepsilon_6 = 1/1024$ to damp spurious short waves. Observe that instabilities arise approximately above $CFL = 1.7$ and $CFL = 1.2$ for the case of RK4 and LDDRK6, respectively. For a given CFL, LDDRK6 scheme causes much less dissipation when used with the fourth-order DRP scheme, as expected. However, care must be taken to select the time integration to be

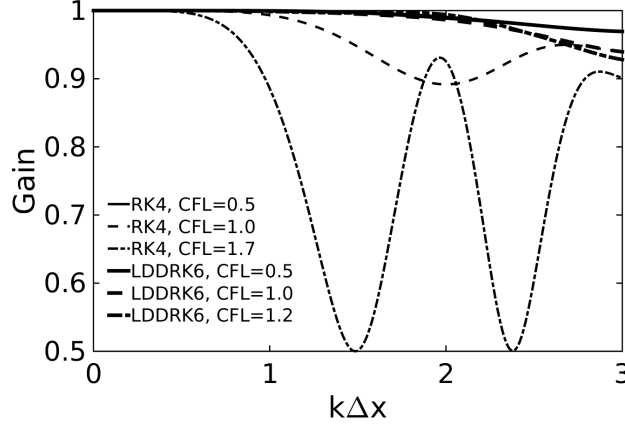


Figure 2.4: Stability analysis and wave dissipation of the DRP scheme using RK4 and LDDRK6 ($\varepsilon_6 = 1/1024$).

used, because both time step limit and computational burden per step are aspects that need attention. In fact, when wall-bounded unsteady flows are solved with explicit methods, time step limit is the prime concern owing to the fact that smallest cells limit the time step too harshly. Therefore, dispersion and dissipation may not be a problem, as most of the wave spectrum is conserved throughout larger convection-dominated cells. A time integration with a good (stability limit)/(computational cost) balance should be the choice to reduce the computation time. In boundary layers, where the smallest cell is naturally found, a time integration scheme with largest stability limit for the diffusion term should be the best choice. LDDRK5 [106] is a good choice for such efficiency, or even Martinelli-Jameson RK5 is the utmost scheme [107, 93]. Still, the explicit method is inefficient when solving compressible Navier-Stokes equations on wall-bounded flows due to strict time step restriction imposed by CFL condition, whereas an implicit method has no such restrictions. Thus, an implicit method combined with dual time stepping approach is crucial, allowing feasible time step sizes. Note that the step size should be bounded above by the time scale of flow unsteadiness of interest, instead of being strictly limited by stability limit in explicit time integration methods.

In the next section, a dual time stepping method is constructed for more efficient time integration in viscous flows. Let us first investigate the dispersion and dissipation characteristics of the second-order backward Euler method, which is the most com-

mon time integration scheme in implementations of dual time stepping approaches. Consider, once more, the linear advection equation (Eq. 2.41) as the model equation. An implicit backward Euler discretization with second order accuracy would read

$$\frac{3u_j^{(n+1)} - 4u_j^{(n)} + u_j^{(n-1)}}{2\Delta t} + aD(u_j^{(n+1)}) = 0 \quad (2.44)$$

where D is the discretization of the convection term that will be selected from Eq.'s 2.43. Generally speaking, let

$$D(u_j^{(n)}) = \frac{u_j^{(n)}}{\Delta x} \sum_{m=-p}^r a_m \exp(mik\Delta x)$$

Through taking $u_j^{(n)} = \tilde{u} \exp[i(kx_j - kat^{(n)})]$ as before, dividing both sides of Eq. 2.44 with $u_j^{(n)}$ yields the amplification definition $G = u^{(n+1)}/u^{(n)} = u^{(n)}/u^{(n-1)}$,

$$\frac{3G - 4 + 1/G}{2\Delta t} + \frac{aG}{\Delta x} \sum_{m=-p}^r a_m \exp(mik\Delta x) = 0$$

and making use of the definition of Courant number $\sigma = a\Delta t/\Delta x$, the amplification equation yields,

$$\left(\frac{3}{2} + \sigma \sum_{m=-p}^r a_m \exp(mik\Delta x) \right) G^2 - 2G + \frac{1}{2} = 0$$

One root of the quadratic equation seems to give physically meaningful results:

$$G = \frac{2 + \sqrt{4 - (3 + 2A)}}{3 + 2A} \quad (2.45)$$

where $A = \sigma \sum_{m=-p}^r a_m \exp(mik\Delta x)$. The amplification $|G|$ and phase deviation $\frac{\angle G}{-\sigma k \Delta x}$ of the 2nd order accurate implicit backward Euler method, combined with the fourth-order DRP spatial discretization, is demonstrated in Figure 2.5 for several CFL numbers. Because the method strongly dissipates waves in high CFL values, the convection-dominated region should be handled with a local CFL number of order one. Besides, the viscous regions, i.e. deep inside boundary layers, dispersion and dissipation of waves is irrelevant unless DNS or LES is being considered. To put it simply, upper limit of time step in a wall-bounded unsteady flow simulation should correspond to a local CFL number of order one in the region where convection starts to dominate. In hybrid RANS/LES terms, local CFL should be small enough in regions where the solution switches to LES mode.

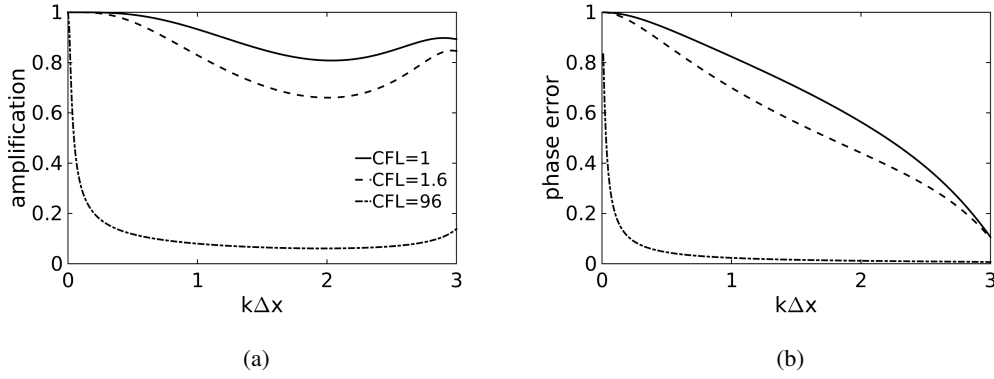


Figure 2.5: Implicit backward Euler temporal scheme with fourth-order DRP spatial scheme (a) dissipation, (b) phase error.

2.6 Dual-time Stepping Strategy

Explicit time-stepping schemes can be very restricting since dimensions of the smallest cell determines the largest possible time step that gives a CFL number of the order of unity. In viscous wall-bounded flows the time step restriction is quite troublesome. In such cases, implicit schemes are preferred. Dual time-stepping method, proposed by Jameson [108], is based on an implicit second-order backward differencing scheme which can be shown as

$$\frac{3W^{(n+1)} - 4W^{(n)} + W^{(n-1)}}{2\Delta t} = -R^{(n+1)} \quad (2.46)$$

where R is the residual, which is equal to flux balance divided by volume of the cell in a finite volume perception. This equation can be solved iteratively in an explicit manner by introducing a pseudo-time (denoted by τ) integration

$$\frac{\partial W^{(n+1)}}{\partial \tau} + \frac{3W^{(n+1)} - 4W^{(n)} + W^{(n-1)}}{2\Delta t} + R^{(n+1)} = 0 \quad (2.47)$$

where the new residual $R^* = \frac{3W^{(n+1)} - 4W^{(n)} + W^{(n-1)}}{2\Delta t} + R^{(n+1)}$ is supposed to go zero as the iterations converge, satisfying the main unsteady equation (Eq. 2.46). The semi-discrete form above can be solved iteratively in a multistage Runge-Kutta framework with m stages,

$$W^{(k+1)} = W^{(0)} - \alpha_k \Delta \tau \left(R^{(k)} + \frac{c_t W^{(k+1)} - E(W^{(n)}, \dots)}{\Delta t} \right) \quad (2.48)$$

in a similar fashion with the explicit time integration algorithm (see Section ?). Superscript k stands for the pseudo-time iteration index whereas n is the physical time iteration index. Note here that the backward time scheme is generalized for convenience (accordingly, $c_t = \frac{3}{2}$, $E = 2W^{(n)} - \frac{1}{2}W^{(n-1)}$ currently). As the iteration is converged, $R^{(k+1)} \approx R^{(n+1)}$ and $W^{(k+1)} \approx W^{(n+1)}$. The residual term can be linearized as $R^{(k+1)} \approx R^{(k)} + \frac{\partial R^{(k)}}{\partial \tau} \Delta \tau$ where the derivative tends to zero during convergence. Therefore, in the above equation, $R^{(k)}$ may be taken instead.

One important thing to note is that the order of time accuracy is determined only by the backward differencing formula (Eq. 2.46) thanks to the fact that the accuracy issue of the pseudo-time integration is eliminated when the residual sufficiently converges to zero. The difficulty in the above formulation is that $W^{(k+1)}$ on the right-hand side is not known. One can simply assume it to be $W^{(k)}$ (as done for $R^{(k+1)}$) relying on the convergence of the subiterations. However it is reported that convergence can be troublesome when the pseudo time step locally happens to be in the same order with the physical time [109]. Instead, replacing $n + 1$ by $k + 1$ on the left-hand side allows implicit treatment of the term such that

$$W^{(k+1)} = W^{(0)} - \alpha_k \Delta \tau \left(R^{(k)} + \frac{c_t W^{(k)} - E(W^{(n)}, \dots)}{\Delta t} \right) - \alpha_k c_t \Delta \tau \frac{W^{(k+1)} - W^{(k)}}{\Delta t} \quad (2.49)$$

as suggested by Melson and Sanetrik [110]. Hence, restrictions on pseudo-time step are banished. Note that the last term vanishes under convergence together with the second term. Arranging the terms and defining the modified residual as $(R^*)^{(k)} = R^{(k)} + \frac{c_t W^{(k)} - E(W^{(n)}, \dots)}{\Delta t}$ gives

$$(1 + \alpha_k c_t \frac{\Delta \tau}{\Delta t}) W^{(k+1)} = W^{(0)} - \alpha_k \Delta \tau (R^*)^{(k)} + \alpha_k c_t \frac{\Delta \tau}{\Delta t} W^{(k)} \quad (2.50)$$

Solving the above equation iteratively is performed through a 5-stage Runge-Kutta with Martinelli-Jameson coefficients [107, 93] $\alpha = \{1/4, 1/6, 3/8, 1/2, 1\}$ and $\beta = \{1, 0, 0.56, 0, 0.44\}$ designed for larger stability for diffusion terms and high damping efficiency for multigrid. Upon splitting the flux balance into convective and diffusive flux balances, $R = R_c + R_d$, a stage in a general case is given as,

$$W^{(k+1)} = W^{(0)} - \alpha_k \Delta \tau \left[R_c^{(k)} + \beta_k R_d^{(k)} + (1 - \beta_k) R_d^{(k-1)} \right] \quad (2.51)$$

Accordingly, the diffusive fluxes are only computed on the odd stages and combined

with their previous evaluations with weighting coefficients. Application of the above formulation to Eq. 2.50 is straightforward.

2.7 Local Preconditioning for the Dual Time Algorithm

Particularly in low Mach number flows, the acoustic speeds are far higher than convective speeds. Hence, for an explicit time scheme with a Courant number in the order of one, the time step is severely restricted by the acoustic speed, resulting in dramatically slow convergence of the solution. Apart from that, condition number of the system increases abruptly in the incompressible limit which results in very poor convergence. These problems are the major shortcomings of compressible flow solvers intended for solution of domains with a low speed region (e.g. turbomachinery flows, wind turbine rotor flows, vertical landing simulations). Preconditioning the equation system is a crucial way to accelerate convergence to a steady solution by minimizing the discrepancy between acoustic and convective speeds, i.e. gathering the eigenvalues together on the complex plane. Hence the stiffness of the problem is reduced and convergence is accelerated, and in some cases convergence is ensured. The diagram in Figure 2.6 due to Pierce [111] clearly describes the convergence issues particularly in multigrid methods. Mesh-aligned artificial dissipation, matrix dissipation, residual smoothing, low speed preconditioning and Jacobi preconditioning are several numerical solutions addressed to overcome such convergence slowing or breaking obstacles.

Another benefit of preconditioning an unsteady problem is accuracy. In fact, rescaling of the eigenvalues provides proper scaling of the artificial dissipation for all the equations [112], whereas the traditional dissipation schemes are over-dissipative in low-Mach regimes.

Last but not the least, preconditioning also enhances high wave frequency damping ability of the smoother, which is an essential element in multigrid algorithms. It was shown by Darmofal *et al.* [112] through Fourier footprint analysis of the discrete spatial operator that the eigenvalues are clustered around highly damping regions on the complex plane, improving damping of high frequency error modes.

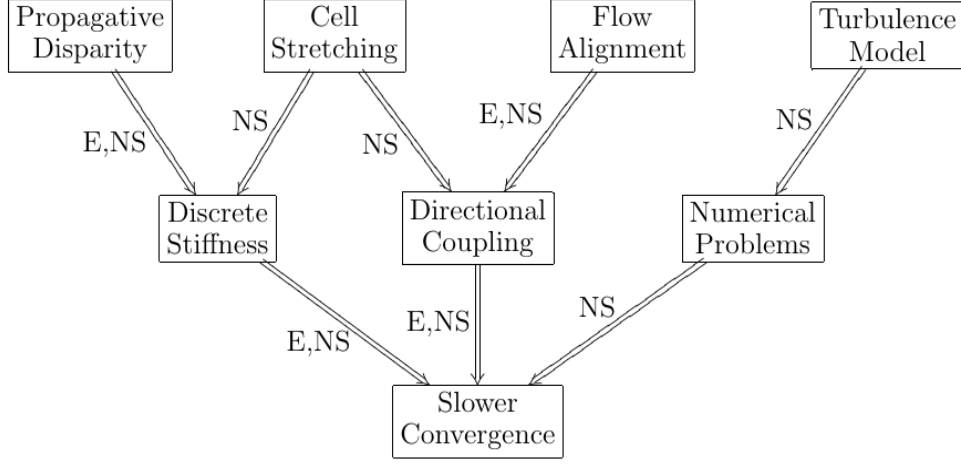


Figure 2.6: Sources of convergence breakdown for Euler and Navier-Stokes equations [111]

The benefits of local preconditioning are valid as well for time dependent problems in a dual time stepping context [113, 114]. Except, an additional condition is necessary for the preconditioning parameter.

Two types of preconditioners are considered in this study: low speed preconditioning and Jacobi preconditioning. These two types are then conveniently combined under the name “squared preconditioning” [81, 114].

2.7.1 Low Speed Preconditioning

At low Mach numbers, propagation speeds of convective and acoustic waves become disparate. This results in a very stiff behavior of the Euler equations. The stiffness is usually measured with the condition number, which is simply defined as the ratio of the largest possible to the smallest possible absolute eigenvalues of the system. It can be shown that

$$K(A) = \frac{\max(|\lambda|)}{\min(|\lambda|)} = \begin{cases} \frac{M+1}{M}, & M \leq 0.5 \\ \frac{M+1}{|M-1|}, & M \geq 0.5 \end{cases} \quad (2.52)$$

for a Jacobian matrix A [112]. It is apparently large at low Mach numbers, even it diverges in the Mach numbers close to zero and one. Hence the equations are ill-conditioned around $M = 0$ and $M = 1$. The main purpose of low-Mach precon-

ditioners is to reduce the condition number ideally towards 1, i.e. to minimize the gap between the eigenvalues of the system.

All preconditioners have robustness issues to some extent. They perform poorly around stagnation points and flow irregularities. They necessitate proper restrictions on their parameters. Turkel preconditioner [115] proved to be somewhat robust at the expense of optimality. A variant of this preconditioner, Weiss-Smith preconditioner [116], is considered in this study due to its simplicity, having only one parameter. It is conveniently defined in entropy variables as,

$$P_e = \begin{pmatrix} \epsilon & 0 & 0 & 0 & 0 \\ 0 & 1 & 0 & 0 & 0 \\ 0 & 0 & 1 & 0 & 0 \\ 0 & 0 & 0 & 1 & 0 \\ 0 & 0 & 0 & 0 & 1 \end{pmatrix} \quad (2.53)$$

where $\epsilon = \mathcal{O}(M^2)$ is the preconditioning parameter which will be defined later. Note that the variable sets can be converted from one another through transformation matrices (see Appendix A).

Starting from the unpreconditioned discrete Euler equations in differential form with dual time stepping strategy, and sticking to the central dissipation scheme discussed in Sec. 2.3,

$$W^{(k+1)} - W^{(k)} + \Delta\tau \left[\frac{c_t W - E(W^{(n)}, ..)}{\Delta t} + A_x \frac{\partial W}{\partial x} + A_y \frac{\partial W}{\partial y} + A_z \frac{\partial W}{\partial z} - \mu_a \left\{ \frac{\partial^2}{\partial x^2} \left(|\mathbf{A}_x| \frac{\partial^4 W}{\partial x^4} \right) + \frac{\partial^2}{\partial y^2} \left(|\mathbf{A}_y| \frac{\partial^4 W}{\partial y^4} \right) + \frac{\partial^2}{\partial z^2} \left(|\mathbf{A}_z| \frac{\partial^4 W}{\partial z^4} \right) \right\} \right]^{(k)} = 0 \quad (2.54)$$

where the spatial derivatives are shown in continuous form for compactness. The spectral radii ($\rho(A_x), ..$) in the artificial viscosity have been replaced with cut-off absolute value matrix, in the framework of matrix dissipation model of the JST scheme (see Sec.2.3). The second derivative terms can be added as well for shock capturing. Following the interpretation of Hosseini [117], preconditioning is applied as a modification to the characteristics of the equations as follows

$$\begin{aligned}
W^{(k+1)} - W^{(k)} + \Delta\tau P \left[\frac{c_t W - E}{\Delta t} + A_x \frac{\partial W}{\partial x} + A_y \frac{\partial W}{\partial y} + A_z \frac{\partial W}{\partial z} \right. \\
\left. - \mu_a \left\{ \frac{\partial^2}{\partial x^2} \left(P^{-1} |P A_x| \frac{\partial^4 W}{\partial x^4} \right) + \frac{\partial^2}{\partial y^2} \left(P^{-1} |P A_y| \frac{\partial^4 W}{\partial y^4} \right) \right. \right. \\
\left. \left. + \frac{\partial^2}{\partial z^2} \left(P^{-1} |P A_z| \frac{\partial^4 W}{\partial z^4} \right) \right\} \right]^{(k)} = 0 \quad (2.55)
\end{aligned}$$

Since the characteristics of the equation has been altered, the time step is calculated by

$$\Delta\tau = \left[\frac{1}{\sigma} \left(\rho(PZ) + \frac{\rho(PA_x)}{\Delta x} + \frac{\rho(PA_y)}{\Delta y} + \frac{\rho(PA_z)}{\Delta z} \right) \right]^{-1} \quad (2.56)$$

where $Z = \frac{c_t}{\Delta t}$, and σ is the pseudo-time CFL number.

2.7.2 Determination of preconditioning parameter (ϵ)

The preconditioning parameter is ideally $\epsilon \sim M^2$ for clustering the eigenvalues together. However, it should be limited for consistency and robustness in most cases. It is turned off in supersonic flow regions by limiting with $\epsilon = 1$ above. It must be limited from below as well, to prevent from going to zero. Thus, initially it is defined as

$$\epsilon = \min [1, \max(M_{lim}^2, M^2)] \quad (2.57)$$

where $M_{lim} = 10^{-5}$ is set to curb singularities. Numerically it was shown that these limiters are not sufficient to ensure robustness [118]. Further measures have been proposed to reduce preconditioning where necessary. First of all, the local cutoff value for robustness around stagnation points is defined as $\sigma_{pgr} \frac{|\Delta p|}{\rho c^2}$, where $|\Delta p|$ is the maximum pressure variation in the vicinity, σ_{pgr} is a case dependent parameter taken equal to 2 unless stated, and c is the sound speed. Moreover, preconditioning must be limited in low Reynolds number regions where diffusive fluxes dominate, since preconditioners are designed for convective fluxes. Isentropic Mach number M_{is} is a good measure for such regions. Thus, the preconditioner definition for viscous steady flows is

$$\begin{aligned}
\epsilon_s = \min \left[1, \max \left(M_{lim}^2, M^2, \sigma_{pgr} \frac{|\Delta p|}{\rho c^2}, M_{is}^2 \right) \right] \\
\text{with } M_{is}^2 = \frac{2}{\gamma - 1} \left[\left(\frac{p_{t\infty}}{p} \right)^{\frac{\gamma-1}{\gamma}} - 1 \right] \quad (2.58)
\end{aligned}$$

where $p_{t\infty}$ is the free stream total pressure. Lastly, in time accurate computations, preconditioning should also be limited by unsteadiness of the flow. The unsteady Mach number scale [82]

$$M_u = \frac{L_u}{\pi \Delta t c} \quad (2.59)$$

is a good measure for resolution of the largest time scale, where L_u is the largest possible wavelength allowed by the domain or geometry. The final form of the parameter is thus given by [82, 119],

$$\epsilon_u = \min \left[1, \max \left(M_{lim}^2, M^2, \sigma_{pgr} \frac{|\Delta p|}{\rho c^2}, M_{is}^2, M_u^2 \right) \right] \quad (2.60)$$

Observe that a small time step or large wave length may turn off low speed preconditioning totally, leaving the user only with other means of convergence acceleration.

2.7.3 Jacobi Preconditioning

Proposed by Allmaras [120] and Pierce and Giles [121] for steady state flows, it is straightforward to implement in dual time stepping approaches. Jacobi preconditioning is commonly perceived as replacing the scalar time step with a matrix time step and adding a matrix-based artificial viscosity [92] instead of scalar viscosity. Hence, the usual “scalar” time step,

$$\Delta \tau = \left[\frac{1}{\sigma} \left(Z + \frac{\rho(A_x)}{\Delta x} + \frac{\rho(A_y)}{\Delta y} + \frac{\rho(A_z)}{\Delta z} \right) \right]^{-1} \quad (2.61)$$

is replaced with the “matrix time step”,

$$\Delta \tau = \left[\frac{1}{\sigma} \left(ZI + \frac{|A_x|}{\Delta x} + \frac{|A_y|}{\Delta y} + \frac{|A_z|}{\Delta z} \right) \right]^{-1} \quad (2.62)$$

Ideally, it should cover the diffusive Jacobian matrices as well.

It is designed to accelerate convergence to a steady state by facilitating individual time step for each transport equation and most importantly, by effectively damping high frequency error components. Therefore, it shows its greatest value in a multigrid scheme serving as a good smoother [122].

2.7.4 Preconditioning Squared

Jacobi preconditioner merely serves as a good smoother during convergence to a steady state. It does not optimize the condition number of the system, nor it corrects the scaling of the artificial viscosity, which are crucial in low Mach regions. Jacobi and low-Mach preconditioners were combined by Turkel [81] for better accuracy and higher convergence rates in low Mach steady state flows. The combination of is straightforward in the above interpretation: replace the scalar time step definition with a matrix time step definition (Eq.2.62), and the scalar artificial dissipation with a matrix dissipation for a low-Mach preconditioned case. For a dual time scheme, it is formulated as

$$W^{(k+1)} - W^{(k)} + \left[\frac{1}{\sigma} \left(PZI + \frac{|PA_x|}{\Delta x} + \frac{|PA_y|}{\Delta y} + \frac{|PA_z|}{\Delta z} \right) \right]^{-1} P \left[\frac{c_t W - E}{\Delta t} + A_x \frac{\partial W}{\partial x} + A_y \frac{\partial W}{\partial y} + A_z \frac{\partial W}{\partial z} - \mu_a \left\{ \frac{\partial^2}{\partial x^2} \left(P^{-1} |PA_x| \frac{\partial^4 W}{\partial x^4} \right) + \frac{\partial^2}{\partial y^2} \left(P^{-1} |PA_y| \frac{\partial^4 W}{\partial y^4} \right) + \frac{\partial^2}{\partial z^2} \left(P^{-1} |PA_z| \frac{\partial^4 W}{\partial z^4} \right) \right\} \right]^{(k)} = 0 \quad (2.63)$$

The P factor of the residual vector can be embedded into the matrix time step [117]:

$$W^{(k+1)} - W^{(k)} + \left[\frac{1}{\sigma} \left(ZI + \frac{P^{-1}|PA_x|}{\Delta x} + \frac{P^{-1}|PA_y|}{\Delta y} + \frac{P^{-1}|PA_z|}{\Delta z} \right) \right]^{-1} \left[\frac{c_t W - E}{\Delta t} + A_x \frac{\partial W}{\partial x} + A_y \frac{\partial W}{\partial y} + A_z \frac{\partial W}{\partial z} - \mu_a \left\{ \frac{\partial^2}{\partial x^2} \left(P^{-1} |PA_x| \frac{\partial^4 W}{\partial x^4} \right) + \frac{\partial^2}{\partial y^2} \left(P^{-1} |PA_y| \frac{\partial^4 W}{\partial y^4} \right) + \frac{\partial^2}{\partial z^2} \left(P^{-1} |PA_z| \frac{\partial^4 W}{\partial z^4} \right) \right\} \right]^{(k)} = 0 \quad (2.64)$$

This form is more preferable because the matrices $P^{-1}|PA_x|$, .. are found to be symmetric, appearing both in the time step and artificial viscosity terms.

This method can be applied to Navier-Stokes equations including the Jacobian matrices of the viscous terms in the matrix time step. A 2-D analysis is performed and tested by Hosseini [117]. However, it is doubted that the advantages are worth bothering because of additional complexity and computational burden stemming from the 3-D versions of the viscous Jacobians. Instead, spectral radius for the viscous terms can be added crudely to the diagonal of the inverse matrix time step as a stability safeguard in boundary layers.

2.7.5 Implementation of Preconditioning Squared

In entropy variables $dW_e = \left[\frac{dp}{\rho c}, du, dv, dw, dS \right]$, it is convenient to construct the squared preconditioner matrices thanks to relatively simple eigenvalues and eigenvectors. Following notation of Hosseini [117],

$$P_e^{-1} |P_e A_e|^* = \begin{pmatrix} \frac{c(s+|\lambda_2|^*)-q_n r(1-\epsilon)}{c\epsilon} & rn_x & rn_y & rn_z & 0 \\ rn_x & sn_x^2 + |\lambda_2|^* & sn_x n_y & sn_x n_z & 0 \\ rn_y & sn_x n_y & sn_y^2 + |\lambda_2|^* & sn_y n_z & 0 \\ rn_z & sn_x n_z & sn_y n_z & sn_z^2 + |\lambda_2|^* & 0 \\ 0 & 0 & 0 & 0 & |\lambda_2|^* \end{pmatrix} \quad (2.65)$$

which is a formulation in any grid-aligned unit direction $\vec{n} = n_x \hat{i} + n_y \hat{j} + n_z \hat{k}$. The superscript asterisk denotes that the eigenvalues are cut off for robustness, since they can get close to zero otherwise. Other definitions are as follows

$$q_n = un_x + vn_y + wn_z \quad (2.66)$$

$$\delta = \sqrt{(1-\epsilon)^2 q_n^2 + 4\epsilon c^2} \quad (2.67)$$

$$\lambda_1 = \frac{1}{2} [(1+\epsilon)q_n - \delta] \quad (2.68)$$

$$\lambda_{2,3,4} = q_n \quad (2.69)$$

$$\lambda_5 = \frac{1}{2} [(1+\epsilon)q_n + \delta] \quad (2.70)$$

$$r = \frac{c(|\lambda_5|^* - |\lambda_1|^*)}{\delta} \quad (2.71)$$

$$s = \frac{|\lambda_1|^* - 2|\lambda_2|^* + |\lambda_5|^*}{2} + \frac{q_n(1-\epsilon)r}{2c} \quad (2.72)$$

The eigenvalues are cut off as a fraction of the maximum possible. Following Turkel and Vatsa [114],

$$\lambda_{max} = \frac{1}{2} [(1+\epsilon)|q_n| + \delta] \quad (2.73)$$

$$|\lambda_{1,5}|^* = \max(|\lambda_{1,5}|, \epsilon_n \lambda_{max}), \quad |\lambda_2|^* = \max(|\lambda_2|, \epsilon_l \lambda_{max}) \quad (2.74)$$

where ϵ_n and ϵ_l are coefficients typically taken as $\epsilon_n = 0.3$, $\epsilon_l = 0.1$ within the matrix artificial dissipation; $\epsilon_n = \epsilon_l = 0.3$ within the matrix time step.

Remember that above formulations are in entropy variables. Hence transformation matrices are used with ease (see Appendix A) to obtain the final form for implemen-

tation

$$\begin{aligned}
& W^{(k+1)} - W^{(k)} + \\
& \frac{\partial W}{\partial W_e} \left[\frac{1}{\sigma} \left(ZI + \frac{P_e^{-1}|P_e A_{x,e}|}{\Delta x} + \frac{P_e^{-1}|P_e A_{y,e}|}{\Delta y} + \frac{P_e^{-1}|P_e A_{z,e}|}{\Delta z} \right) \right]^{-1} \frac{\partial W_e}{\partial W} \\
& \left[\frac{c_t W - E}{\Delta t} + A_x \frac{\partial W}{\partial x} + A_y \frac{\partial W}{\partial y} + A_z \frac{\partial W}{\partial z} \right. \\
& - \mu_a \left\{ \Delta x^5 \frac{\partial^2}{\partial x^2} \left(\frac{\partial W}{\partial W_e} P_e^{-1} |P_e A_{x,e}| \frac{\partial W_e}{\partial W_p} \frac{\partial^4 W_p}{\partial x^4} \right) \right. \\
& + \Delta y^5 \frac{\partial^2}{\partial y^2} \left(\frac{\partial W}{\partial W_e} P_e^{-1} |P_e A_{y,e}| \frac{\partial W_e}{\partial W_p} \frac{\partial^4 W_p}{\partial y^4} \right) \\
& \left. \left. + \Delta z^5 \frac{\partial^2}{\partial z^2} \left(\frac{\partial W}{\partial W_e} P_e^{-1} |P_e A_{z,e}| \frac{\partial W_e}{\partial W_p} \frac{\partial^4 W_p}{\partial z^4} \right) \right\} \right]^{(k)} = 0 \quad (2.75)
\end{aligned}$$

Notice that the difference formulas within artificial dissipation terms are constructed in primitive variables, $W_p = [p, u, v, w, T]$, which was reported to perform better in low Mach limit [114]. Additionally, residual norms may be computed in primitive variables as well, due to the fact that density variable does not stand as a good measure of convergence in low Mach numbers, because in that limit, change in density is trivial.

The implementation is formulated for the finite volume (with flux balance $A_\xi S_\xi \frac{\partial W}{\partial \xi} + \dots$, etc.) in a low-storage Runge-Kutta stage as

$$\begin{aligned}
& W^{(k+1)} = W^{(k)} - \\
& \alpha_{(s)} \sigma \frac{\partial W}{\partial W_e} \left[ZI + \frac{P_e^{-1}|P_e A_{\xi,e}| S_\xi}{\Delta \xi} + \frac{P_e^{-1}|P_e A_{\eta,e}| S_\eta}{\Delta \eta} + \frac{P_e^{-1}|P_e A_{\zeta,e}| S_\zeta}{\Delta \zeta} \right]^{-1} \frac{\partial W_e}{\partial W} \\
& \left[\frac{c_t W - E}{\Delta t} + A_\xi S_\xi \frac{\partial W}{\partial \xi} + A_\eta S_\eta \frac{\partial W}{\partial \eta} + A_\zeta S_\zeta \frac{\partial W}{\partial \zeta} \right. \\
& - \mu_a \left\{ \Delta \xi^5 \frac{\partial^2}{\partial \xi^2} \left(\frac{\partial W}{\partial W_e} P_e^{-1} |P_e A_{\xi,e}| S_\xi \frac{\partial W_e}{\partial W_p} \frac{\partial^4 W_p}{\partial \xi^4} \right) \right. \\
& + \Delta \eta^5 \frac{\partial^2}{\partial \eta^2} \left(\frac{\partial W}{\partial W_e} P_e^{-1} |P_e A_{\eta,e}| S_\eta \frac{\partial W_e}{\partial W_p} \frac{\partial^4 W_p}{\partial \eta^4} \right) \\
& \left. \left. + \Delta \zeta^5 \frac{\partial^2}{\partial \zeta^2} \left(\frac{\partial W}{\partial W_e} P_e^{-1} |P_e A_{\zeta,e}| S_\zeta \frac{\partial W_e}{\partial W_p} \frac{\partial^4 W_p}{\partial \zeta^4} \right) \right\} \right]^{(k)} \quad (2.76)
\end{aligned}$$

where $\alpha_{(s)}$ is the Runge-Kutta constant for the stage s , and $S_{\xi,\eta,\zeta}$ are the area values in grid-aligned directions.

2.7.6 Blended Matrix Dissipation Form

Matrix artificial dissipation may be computed either with the use of preconditioner parameter for steady flows or that for unsteady flows defined in equations 2.58 and 2.60. Naturally, the preconditioner for unsteady flows is used in dissipation scaling when the problem is time accurate, as used in the convective terms of the equations. Nevertheless, the velocity and temperature variables are highly damped in the natural approach. Use of steady preconditioner instead properly scales dissipation in steady limit ($M_u \ll 1$), although pressure variable is not treated well in unsteady flows, causing convergence issues. Potsdam *et al.* [82] implemented blending of both scalings, which is adapted for ξ -direction to the current formulation as follows

$$D_\xi = \mu_a \Delta \xi^5 \frac{\partial^2}{\partial \xi^2} \left(\frac{\partial W}{\partial W_e} (P_e^{-1} |P_e A_{\xi,e}|)_u \frac{\partial W_e}{\partial W_p} L_p \frac{\partial^4 W_p}{\partial \xi^4} + \frac{\partial W}{\partial W_e} (P_e^{-1} |P_e A_{\xi,e}|)_s \frac{\partial W_e}{\partial W_p} L_{vT} \frac{\partial^4 W_p}{\partial \xi^4} \right) \quad (2.77)$$

where subscripts u & s refers use of unsteady and steady preconditioners, respectively, and the matrices

$$L_p = \begin{pmatrix} 1 & 0 & 0 & 0 & 0 \\ 0 & 0 & 0 & 0 & 0 \\ 0 & 0 & 0 & 0 & 0 \\ 0 & 0 & 0 & 0 & 0 \\ 0 & 0 & 0 & 0 & 0 \end{pmatrix} \quad L_{vT} = \begin{pmatrix} 0 & 0 & 0 & 0 & 0 \\ 0 & 1 & 0 & 0 & 0 \\ 0 & 0 & 1 & 0 & 0 \\ 0 & 0 & 0 & 1 & 0 \\ 0 & 0 & 0 & 0 & 1 \end{pmatrix} \quad (2.78)$$

help treat the variables separately. This definition of scaling is referred as blended matrix dissipation. Formulations in the other grid-aligned directions are similar.

2.7.7 Performance of Preconditioning Squared

An infinitely long wing case with $M = 0.1$ with a largest possible wavelength of 0.1 chords (i.e. span length) is chosen for performance assessment of the implemented preconditioning squared algorithm. Since the main motivation for the preconditioned dual time algorithm has been to subdue infeasible computation time required in viscous cases because of time step restrictions, the first comparison should be made with

the explicit method. The case was run 1000 steps using the explicit method with maximum allowed time step, taking $0.24L/c_\infty$ in total. Then it is compared with dual time stepping simulations that are run for one physical time step which is 1000 times as large as the one used in the former. A fixed diffusion constant $\kappa_6 = 1/256$ is chosen for all simulations. Table 2.1 compares the CPU time required for each simulation. It is seen that dual time stepping combined with Jacobi and low-Mach preconditioning folds the explicit method by 20 to 30 in speed for this benchmark problem where both high aspect ratio and small cells exist. A better speedup would be expected in lower Mach values, since the difference between convective and acoustic speeds becomes larger, i.e. the system becomes more stiff. Moreover, it was shown that both types of preconditioners considered perform even better when used with multigrid, because they boost damping of high frequency error components [122].

Table 2.1: CPU time comparison for $0.24L/c$ time advancement

	CPU time (s)	
	−2 residual drop	−3 residual drop
precond. (dual time)	196	379
no precond. (dual time)	654	2615
explicit (LDDRK5 [106])	7330	

Convergence acceleration by the preconditioning methods with dual time stepping can be observed in Figure 2.7. The same infinite wing benchmark case is run for several time steps with and without the preconditioners. Low speed preconditioner alone cannot be shown here because modifications required on code for the implementation is not straightforward, whereas simply $\epsilon = 1$ is taken to obtain Jacobi preconditioner alone. Nevertheless, it is obvious that both preconditioners perform splendidly and they perform best when they cooperate. Remember that low speed preconditioner scales artificial viscosity as well, which is crucial for accurate results particularly in low Mach flows.

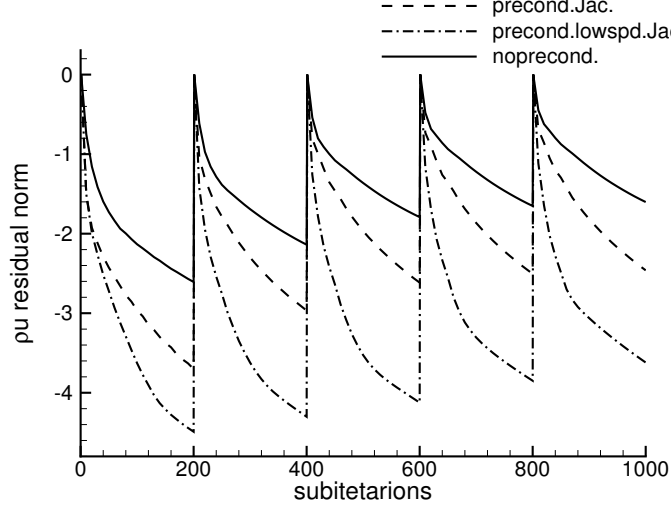


Figure 2.7: Performance comparison for a 0.1c span transient viscous calculation of NACA0012 case under a free stream of $M = 0.1$, $CFL = 3000$

2.8 Implicit Residual Smoothing

Physically, residual smoothing can be interpreted as smoothing out the residual with a form of diffusion operator as the name infers, so that the maximum allowable CFL number of the time integration scheme can be extended. It was introduced by Lerat [123] and adapted to multistage Runge-Kutta scheme by Jameson [124]. In 1-D it is simply formulated as

$$\bar{R}_i - R_i = \epsilon_i \partial_\xi^2 \bar{R}_i \quad (2.79)$$

where residual R_i is smoothed to obtain \bar{R}_i . The smoothing coefficient ϵ_i behaves like a Von Neumann number ($\mu \Delta t / \Delta x^2$) in a diffusion process. Accordingly, the high frequency components of R_i are damped after one time step. The Laplace operator ∂_ξ^2 is usually discretized by second-order central differencing. In 3-D, the Laplace operator is simply factored in each direction to reduce computational effort. Consequently in 3-D, implicit residual smoothing is formulated as follows,

$$\begin{aligned} -\epsilon_i \bar{\bar{R}}_{i-1,j,k} + (1 + 2\epsilon_i) \bar{\bar{R}}_{i,j,k} - \epsilon_i \bar{\bar{R}}_{i+1,j,k} &= R_{i,j,k} \\ -\epsilon_j \bar{\bar{R}}_{i,j-1,k} + (1 + 2\epsilon_j) \bar{\bar{R}}_{i,j,k} - \epsilon_j \bar{\bar{R}}_{i,j+1,k} &= \bar{R}_{i,j,k} \\ -\epsilon_k \bar{\bar{R}}_{i,j,k-1} + (1 + 2\epsilon_k) \bar{\bar{R}}_{i,j,k} - \epsilon_k \bar{\bar{R}}_{i,j,k+1} &= \bar{\bar{R}}_{i,j,k} \end{aligned} \quad (2.80)$$

It is practical to solve the equations in each direction consecutively to reduce the computational burden. Hence, the resulting tridiagonal systems are to be solved in each direction, which should not be troublesome computationally. The smoothing coefficients are given as [125]

$$\begin{aligned}\epsilon_i &= \max \left\{ \frac{1}{4} \left[\left(\frac{\bar{\sigma}}{\sigma} \frac{1}{1 + \Psi(\frac{\Lambda_{c,j}}{\Lambda_{c,i}} + \frac{\Lambda_{c,k}}{\Lambda_{c,i}})} \right)^2 - 1 \right], 0 \right\} \\ \epsilon_j &= \max \left\{ \frac{1}{4} \left[\left(\frac{\bar{\sigma}}{\sigma} \frac{1}{1 + \Psi(\frac{\Lambda_{c,i}}{\Lambda_{c,j}} + \frac{\Lambda_{c,k}}{\Lambda_{c,j}})} \right)^2 - 1 \right], 0 \right\} \\ \epsilon_k &= \max \left\{ \frac{1}{4} \left[\left(\frac{\bar{\sigma}}{\sigma} \frac{1}{1 + \Psi(\frac{\Lambda_{c,i}}{\Lambda_{c,k}} + \frac{\Lambda_{c,j}}{\Lambda_{c,k}})} \right)^2 - 1 \right], 0 \right\}\end{aligned}\tag{2.81}$$

where Λ_c are spectral radius specific to convection terms in each direction, and $\Psi = 0.0625$ typically. Theoretically, one can take the smoothed CFL to unsmoothed CFL number ratio $\bar{\sigma}/\sigma$ infinitely large. However, it is not practical because high wave number smoothing of the Runge-Kutta scheme is disrupted. It is common practice to take $\bar{\sigma}/\sigma \approx 2$.

In viscosity dominated regions, smoothing coefficients based on viscous spectral radii should be used,

$$\begin{aligned}\epsilon_i &= C \frac{\bar{\sigma}}{\sigma} \frac{\Lambda_{v,i}}{\Lambda_{c,i} + \Lambda_{v,j} + \Lambda_{v,k}} \\ \epsilon_j &= C \frac{\bar{\sigma}}{\sigma} \frac{\Lambda_{v,j}}{\Lambda_{c,i} + \Lambda_{v,j} + \Lambda_{v,k}} \\ \epsilon_k &= C \frac{\bar{\sigma}}{\sigma} \frac{\Lambda_{v,k}}{\Lambda_{c,i} + \Lambda_{v,j} + \Lambda_{v,k}}\end{aligned}\tag{2.82}$$

where $C = 5/4$ typically. As a result, the maximum of the local coefficients in Eqs. 2.81 and 2.82 is chosen. Remember that formulation of the convective spectral radii differs when the system is preconditioned (Eq. 2.73).

2.9 Parallelization

It is essential to parallelize a solver if large problems are intended to be solved, not only due to the fact that parallelization harnesses more computing power, but also

supplies more memory thanks to distributed memory systems such as MPI (Message Passing Interface).

In the first step, the mesh decomposer simply reads the mesh by the master process and assigns partitions to the processes equally. Each process reads the corresponding mesh independently and solves their part with necessary communications done in the interfaces. The passing of information between the processes is performed through three levels of ghost cells as sketched in Figure 2.8. Likewise, the grid points in the interfaces are communicated for once, to ensure continuity of the domain. The communication is essentially performed at the end of each stage of the Runge-Kutta iteration. It is sure that this much of ghosts cells would result in considerable communication and consequently, loss of efficiency. However, three levels of cells are essential to ensure fourth order of accuracy of the numerical method seamlessly. In order to maximize the efficiency of the parallel solution, the partitions must be equally large to keep the collaboration among the processes well-balanced. An unbalanced workload among processes would cause waiting periods for some, reducing efficiency. Another tip to increase efficiency is to keep surface to volume ratio of the partitions as low as possible (ideally, equal number of cells in each direction of the partition).

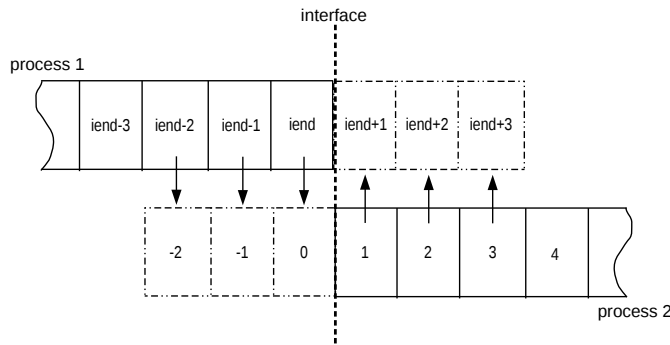


Figure 2.8: Communication between two partitions through ghost cells.

Some benchmark tests are performed on the manufactured flow case mentioned in Section 3.2. The problem is defined with $41 \times 41 \times 41$ nodes, which is decomposed into two partitions in each dimension as shown in Figure 2.9. Decomposition is performed in all directions equally, to enhance parallel efficiency. The results exactly match the serial ones as expected.

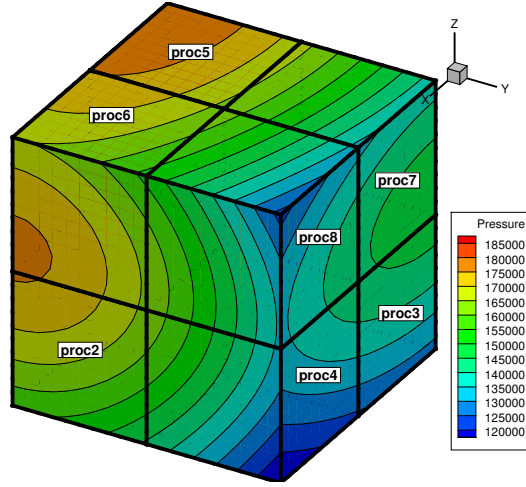


Figure 2.9: Sample block decomposition.

An important test towards benchmarking parallel efficiency is the parallel speed-up curve (see Figure 2.10). The same manufactured solution problem is reproduced on a block with $88 \times 88 \times 88$ cells employing a single computing node with 64 cores and a shared memory of 256 GBs. The block is decomposed into 2 and 4 in each direction, resulting in 8 and 64 partitions, respectively. Likewise, equal decomposition in 2-D and 1-D is examined. As stated above, a 3-D decomposition of a problem enhances parallel performance, through minimizing total interface area. Note here that 1-D decomposition fails after some point due to the excess of ratio of communication work for each partition and unequal extent of the partitions.

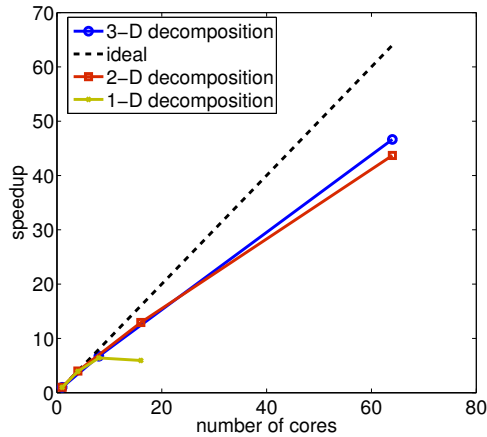


Figure 2.10: Parallel speed-up curves for 1-D, 2-D and 3-D decomposition of a block with 88^3 cells.

CHAPTER 3

VERIFICATION AND VALIDATION OF THE FLOW SOLVER THROUGH BENCHMARK CASES

In this chapter, some test cases are presented to validate the solver's accuracy order and demonstrate competency for inviscid, viscous flows, and turbulence. First, validations are achieved in 2-D cases to justify the extension of the solver to 3-D. In the last section, verification of the 3-D solver is performed on a manufactured case. All tests are conducted using explicit low-storage four-stage Runge-Kutta time integration.

3.1 Preliminary 2-D Cases

3.1.1 Isentropic Vortex Convection

The inherent spatial discretizations are intended to be validated via an isentropic vortex convection test problem, whose analytical solution is simply transport of the initial vortex as it is. Cartesian mesh sizes of 100×100 , 200×200 and 400×400 are generated with some non-uniformity (Figure 3.1). The mesh is generated via smooth transformation of uniform mesh. A strong vortex ($u_A/V_\infty = 0.8$) is convected under $M_\infty = 0.5$ for a time period of $V_\infty t/L = 30$, and periodic conditions on the boundaries. The initial form of the solution is given by,

$$\mathbf{V} = \begin{Bmatrix} V_\infty \\ 0 \\ 0 \end{Bmatrix} + u_A e^{(1-(r/b)^2)/2} \begin{Bmatrix} (y - y_0)/b \\ -(x - x_0)/b \\ 0 \end{Bmatrix} \quad (3.1)$$

for a 2-D vortex defined on $[-25L, 25L]^2$. r is the distance from the vortex center

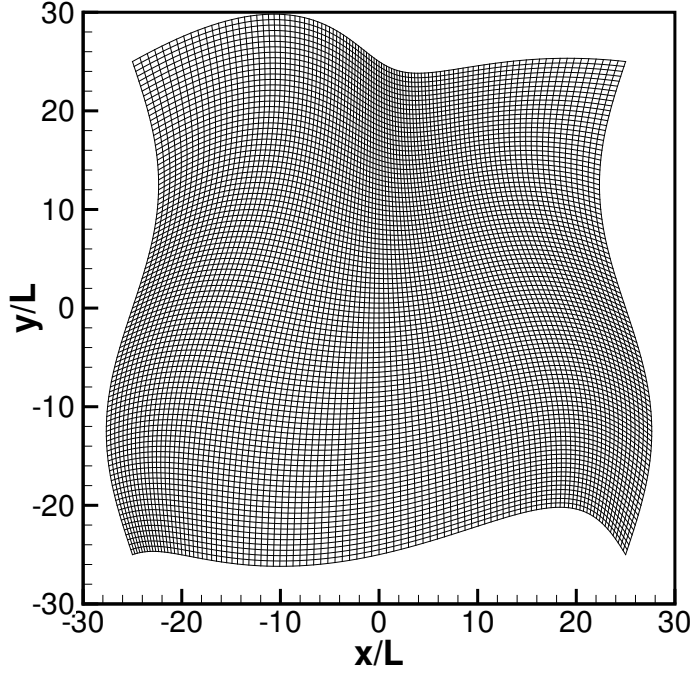


Figure 3.1: Non-uniform Cartesian mesh

(x_0, y_0) . A representative length scale for the vortex can be defined from $e^{-(r/b)^2} = \frac{1}{2}$ at $r = L$. The primitive variables can be found using isentropic relations,

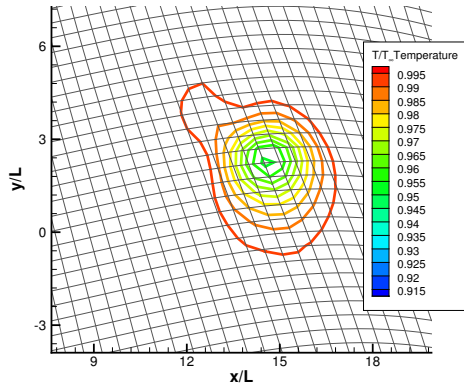
$$\frac{T}{T_\infty} = \left(\frac{p}{p_\infty} \right)^{(\gamma-1)/\gamma} = \left(\frac{\rho}{\rho_\infty} \right)^{\gamma-1} = 1 - \frac{\gamma-1}{2} \frac{u_A^2}{c_\infty^2} e^{1-(r/b)^2} \quad (3.2)$$

A fourth-order efficient four-stage Runge-Kutta time integration is used. Since the compact RK4 is second-order accurate for nonlinear equations, a non-dimensional time step size of order spatial step-size squared in transformed coordinates ($u_\infty \Delta t / L \sim \Delta x^2$) or one order higher than that when instability shows up ($u_\infty \Delta t / L \sim \Delta x^3$), is chosen to prevent the time integration error from overshadowing the spatial discretization error. The vortex is convected a distance from $-15L$ to $15L$ in the x -direction. The temperature contours are shown in Figure 3.2, of the vortex on the 100×100 mesh. Observe the loss of vortex shape and position with some of the schemes. Using central schemes with symmetry preservation is known to lower numerical dissipation, hence reduces peak amplitude loss. It can be observed that the non-symmetric form of divergence does not preserve the peak of the vortex as compared to symmetric form with same accuracy order. Moreover, since dispersion causes waves to travel

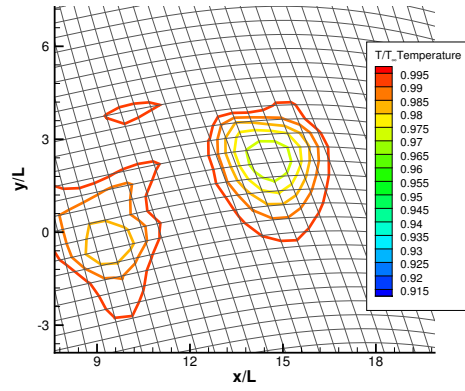
at different speeds, loss of position and shape of the vortex is minimized with low-dispersion DRP scheme (Figure 3.2e). As expected, position and shape of the vortex are most immensely preserved with fourth-order DRP scheme on 400×400 mesh (Figure 3.2f).

The symmetry-preserving scheme proved to be stable without any means of artificial dissipation for this problem. The skew-symmetric form owes this to local and global conservation of total energy by convection, avoiding spurious generation of kinetic and internal energies. However, for compressible flows, where density can drop to some extent, unbounded increase of velocity is not avoided in global conservation of total energy. Still, stability is dramatically enhanced, even though, to eliminate small-amplitude oscillations, a minimal artificial diffusion may be required in other problems such as problems with submerged bodies. In contrast, a standard scheme ($\mathbf{F} = \overline{\rho \mathbf{V} \phi}$) without artificial diffusion would be unstable giving no results at all. Hence, results of the standard scheme are obtained by help of an artificial diffusion, whereas the Jameson-type averaging [90] ($\mathbf{F} = \overline{\rho \mathbf{V}} \overline{\rho \phi} / \overline{\rho}$), which slightly differs from the skew-symmetric form [54], did not require one for this test problem.

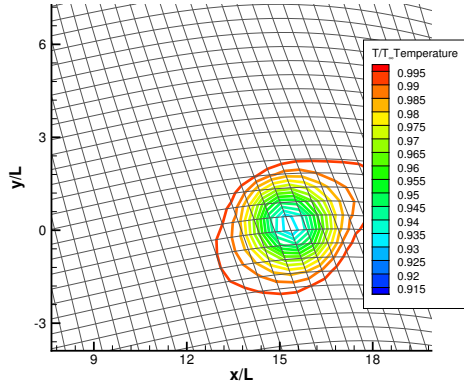
An error analysis is also performed in order to validate the accuracy orders of the schemes. Figure 3.3 shows logarithmic plots of the root-mean-squared error values with respect to doubling mesh sizes. The skew-symmetric fourth-order DRP scheme exhibits the lowest error for all variables. The promised order of accuracies of the schemes seem to be maintained. As to u, v and T , the non-symmetric schemes proved to be almost equally accurate with their symmetric counter-parts, except the standard scheme has little more error due to the influence of artificial diffusion. However, entropy generation levels (Figure 3.3d) plot another story: All schemes demonstrate their success with different levels of error. Entropy generation has to be solely related to numerical dissipation for this inviscid problem (no heat generation/conduction, no shocks). Hence, it can be taken as a measure of numerical dissipation. The skew-symmetric scheme proved to cause less dissipation error, in fact, one order and two order less than corresponding Jameson-type and standard schemes, respectively. The standard scheme has the largest error, due to the fact that an extra dissipation (artificial diffusion) is essentially added. Observe the entropy error results of fourth-order DRP schemes, where minimization of dispersion error for each case provides one order



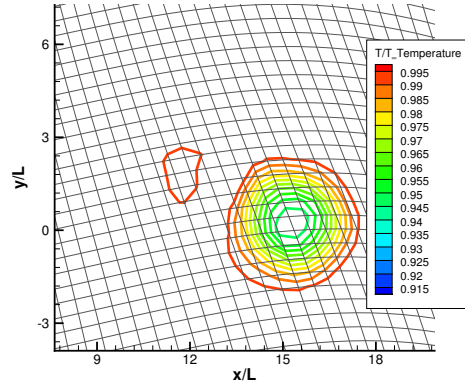
(a) Second-order scheme conserving skew-symmetry on 100×100 grid



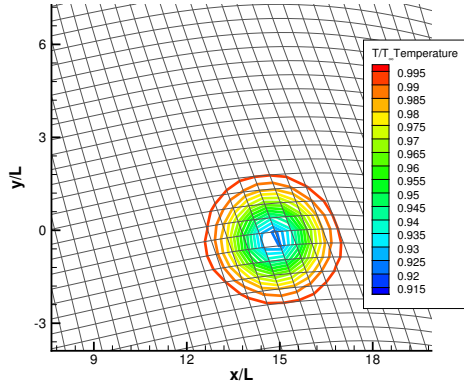
(b) Second-order scheme (Jameson-type scheme) on 100×100 grid



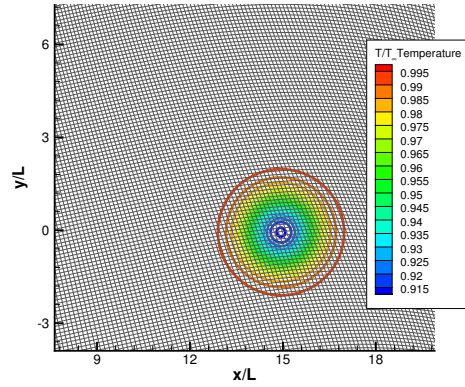
(c) Fourth-order scheme conserving skew-symmetry on 100×100 grid



(d) Fourth-order scheme (Jameson-type scheme) on 100×100 grid



(e) Fourth-order DRP scheme conserving skew-symmetry on 100×100 grid



(f) Fourth-order DRP skew-symmetric scheme on 400×400 grid

Figure 3.2: Temperature contour of the isentropic vortex using symmetry-preserving and Jameson-type schemes

less error. Eventually, Figure 3.3d can be deemed a splendid illustration of merits of skew-symmetry as well as DRP feature of discretizations.

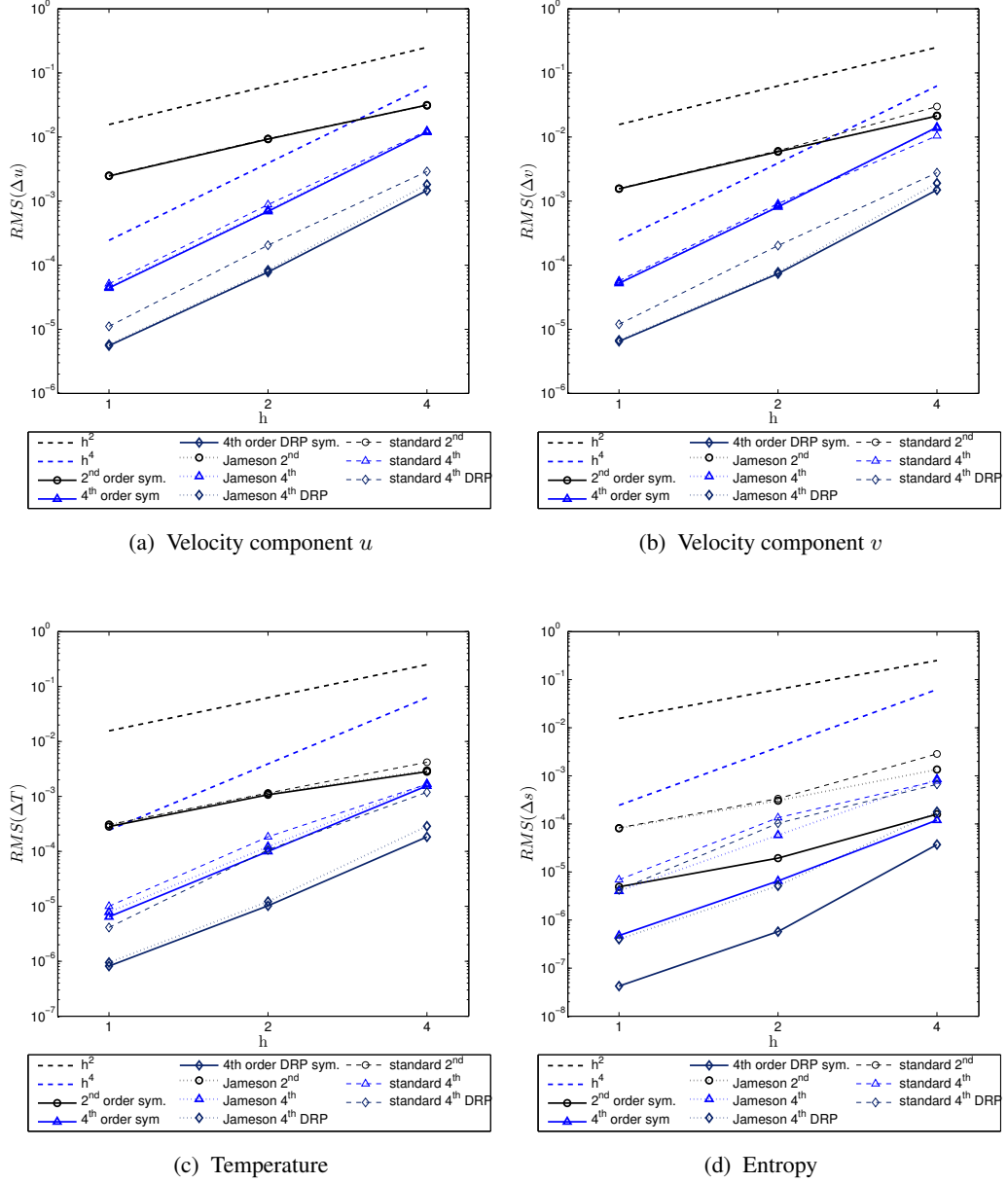


Figure 3.3: Step-size vs. root-mean-square of differences of isentropic vortex convection solutions from analytical values of dimensionless velocities u and v , temperature, entropy.

Essentially, the skew-symmetric discretization of convection term requires additional computations (see Section 2) to obtain averaged flux on cell faces. This results in

more CPU time for a simulation of same accuracy order on the same mesh. For instance, the standard scheme costs 1.3 multiple of the Jameson-type scheme, whereas the skew-symmetric scheme costs 1.8 times what the Jameson-type scheme costs. It is not a big trouble as the profit made from mesh size is considered. In fact, it is observed from the results of the aforementioned vortex problem that the low-dispersion fourth-order skew-symmetric scheme on 200×200 mesh attains the accuracy obtained with the low-dispersion Jameson-type basic scheme on 400×400 mesh. Accordingly, the skew-symmetric form performs around 2.7 times faster than the basic form to achieve the same accuracy, thanks to the mesh-size related cost reduction. The performance gap further extends as second-order basic scheme is compared, and even further on 3-D domains.

3.1.2 Inviscid transonic flow over RAE2822 airfoil

Inviscid flow simulation of an airfoil case can be seen in Figure 3.4. The domain is around 6-chords-length wide having 193×94 grid points and the Mach number is 0.725. The low-dissipation, low-dispersion (DRP) fourth-order scheme is used for the solution. In order to increase the sharpness of the shock as well as reduce oscillations, the artificial dissipation method explained in Section 2.3 is utilized, where a pressure-gradient sensor is employed to switch the dissipation between shock and smooth regions. As the results are compared with the experiment data [126], it can be concluded that there is some difference indeed, particularly, the location of shock differs considerably. A reason for this occasion might be the wall interference of the wind tunnel. More importantly, the experiment definitely reflects a viscous flow, which could result in difference with inviscid transonic flow solutions. After all, the results obtained in another simulation by Özyörük [127], using standard fourth-order accurate finite-difference scheme, compare with the current results quite closely.

3.1.3 Couette flow

A Couette flow case is chosen as the first viscous test case, where an upper plate moves with $U = 75.4 \text{ m/s}$ velocity and a temperature difference of 1 K between the

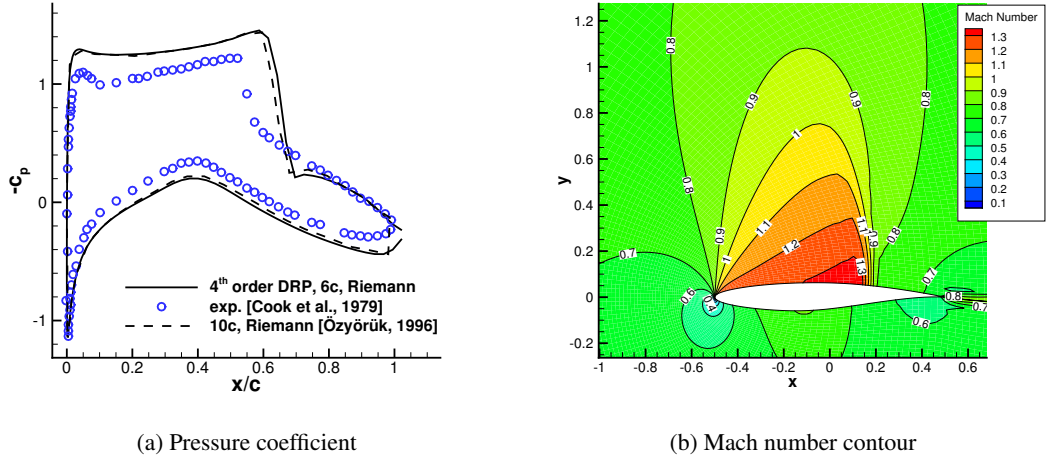
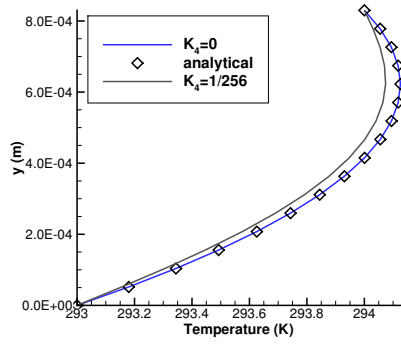
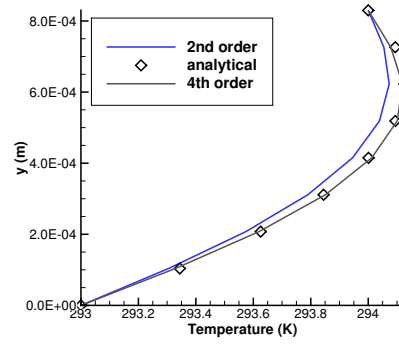


Figure 3.4: Transonic flow simulation on RAE2822 airfoil ($M = 0.725$, $\alpha = 2.92^\circ$)

plates is set. The temperature distribution is shown in Figure 3.5 ($Re = 4000, Pr = 0.708$). Firstly, 17 grid points between the plates is chosen (see Figure 3.5a). Apparently for the current test problem, the low-dissipation scheme does not necessitate artificial dissipation to produce a converged solution, whence the analytical solution can be reproduced perfectly. Note here that the analytical solution is a quadratic equation which can be obtained perfectly with a fourth-order discretization. Nevertheless, addition of the artificial dissipation induces some error, dependent on its intensity factors (K_4, K_6). This observation should be expected because in low Reynolds number flows, diffusion process, which is altered by the artificial diffusion, is dominant on resulting flow behavior. Figure 3.5b demonstrates the case where 9 grid points are used between the plates. Thanks to the fact that without artificial dissipation a perfect match is achieved using both second and fourth-order discretizations, the impact of artificial dissipation reveals. As can be observed, the error order of the artificial dissipation for the fourth-order discretization is higher than that of the second-order discretization, consequently more accurate results are obtained. Note here that post-processing involves linear interpolation between cell centers and boundary conditions are applied using linear extrapolation towards the ghost cells, which conflicts with fourth-order discretization's quadratic predictions. Horizontal velocity distribution is not shown here, which is merely a linear function on y and perfectly obtained using both discretizations.



(a) Second-order accurate solutions on 17×6 grid



(b) Solutions on 9×6 grid with artificial dissipation coefficients of $K_6 = K_4 = 1/2048$

Figure 3.5: Couette flow simulations

3.1.4 Laminar flow over a flat plate

Another notable viscous flow test case is laminar flow over a flat plate. Mach number is selected to be low enough ($M = 0.2$) to use the compressible solver as though incompressible results are obtained. The test setup consists of a flat plate is shown in Figure 3.6 (69×49 grid points totally), where boundary layer at $x = 1.0549 m$ location under $Re_L = 100000$ with $L = 2 m$ is investigated. The results are compared with Blasius solution in Figure 3.7. Both the horizontal velocity profile and the friction coefficient agree well using fourth-order discretization. Since, the vertical velocity naturally has lower order compared to the horizontal velocity, error level becomes more visible. The fourth-order discretization has slightly more accuracy compared to the second-order discretization. Lowering the intensity of artificial dissipation and using matrix dissipation method instead could reduce the error even more.

3.1.5 Symmetric airfoil in laminar flow

A NACA0012 airfoil with blunt trailing edge is tested under a flow of $M = 0.5$ and $Re = 5000$ with no angle of incidence. The mesh is in O-grid topology with an extent of 170 chords consisting of 157×112 grid points. Success of convergence to a solution seems to be equally good for both fourth and second order discretizations

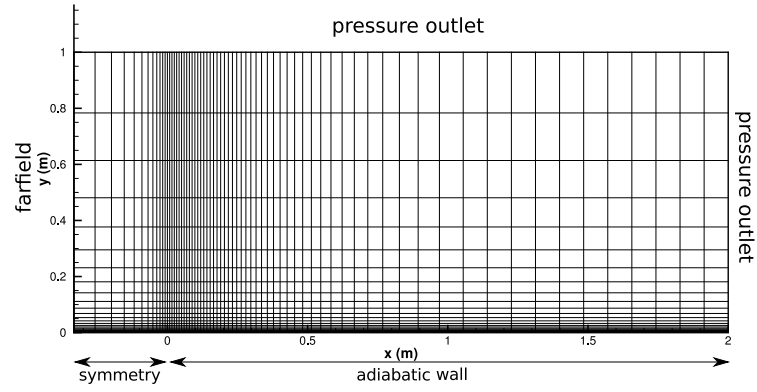


Figure 3.6: Flat plate simulation setup

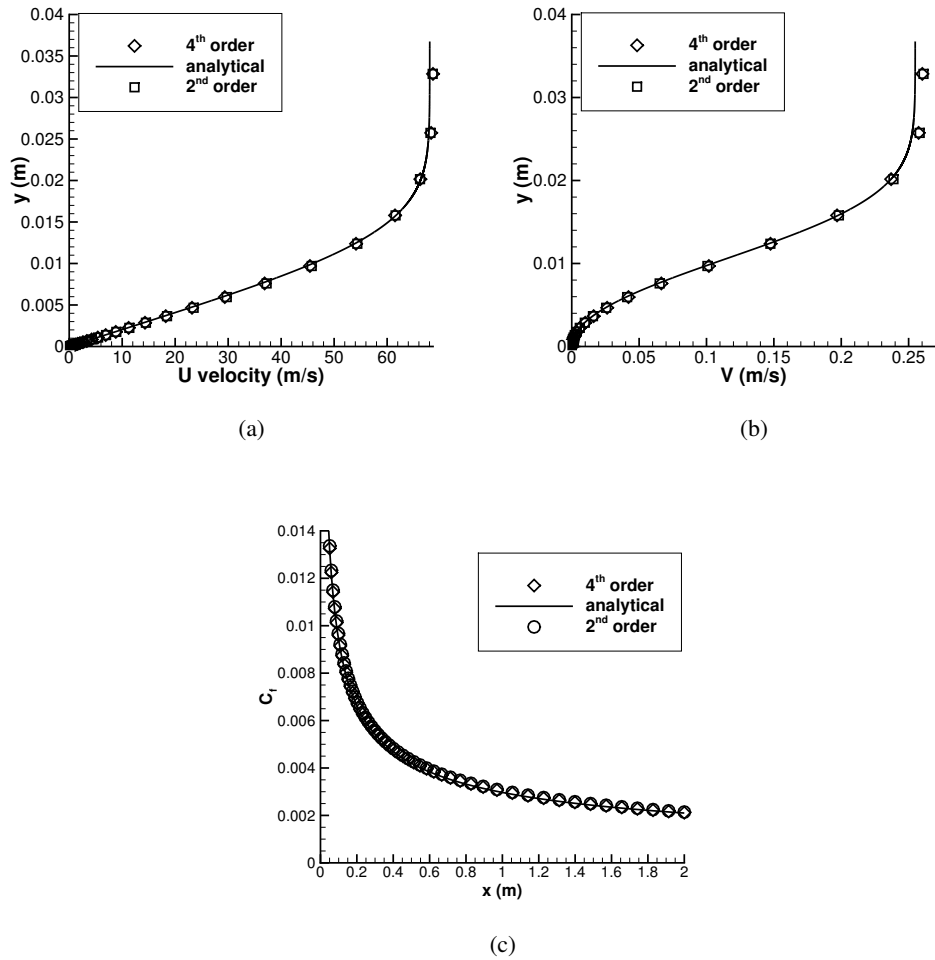


Figure 3.7: Blasius velocity profiles (a,b) and shear coefficient distribution (c)

(see Figure 3.8c). In Figure 3.8b, pressure coefficient is compared with another result from literature [128] where a high-order upwind residual distributive scheme (over P^2 elements) used with 8564 grid points (200 of which being on the airfoil). The fourth-order DRP scheme proves to be closer to the reference solution, despite the deviation in the trailing edge due to its bluntness. A C-grid topology would be the approach to overcome this issue.

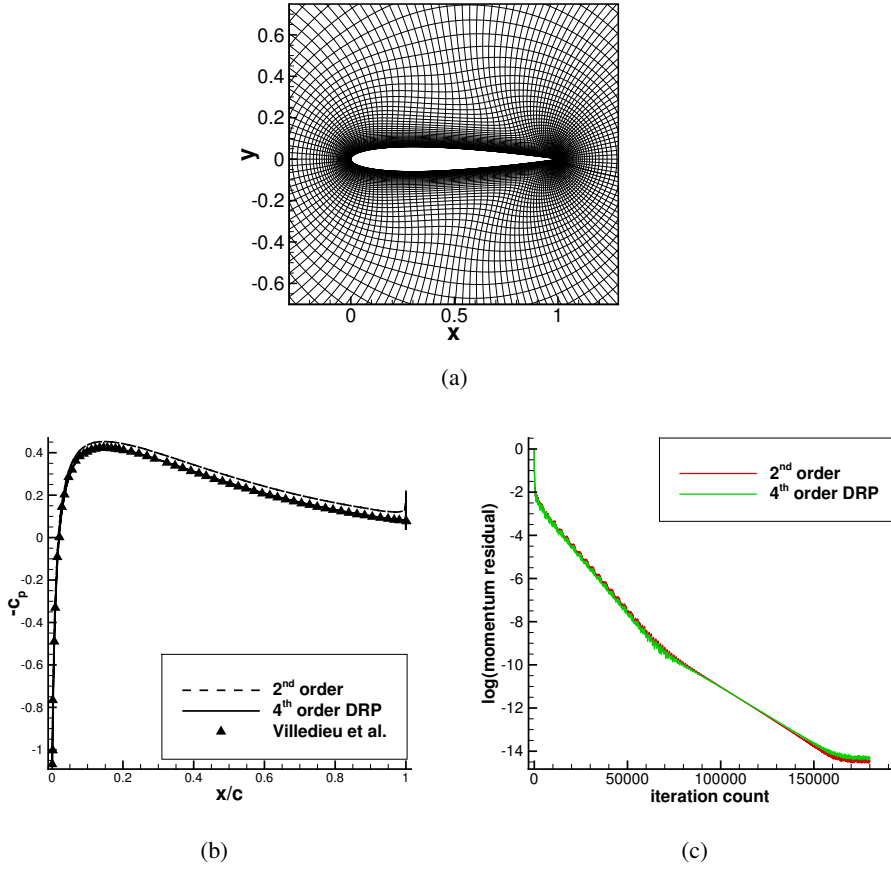


Figure 3.8: Grid (a), pressure coefficient (b) and residual drop (c) on NACA0012 airfoil ($M = 0.5$, $Re = 5000$)

3.1.6 Lid-driven cavity flow

A classical cavity problem is simulated as well, at $Re = 100$ and $Re = 1000$. The top plate moves with a velocity of 1 m/s while the other walls are stationary imposing no-slip boundary condition. The 25×25 and 49×49 grids are clustered near the walls to

be able to resolve higher gradients. The centerline u -velocity and v -velocity plots are compared in Figure 3.9 with the well-known fine-grid solutions (129×129) of Ghia [129]. The accuracy of fourth-order method is obvious, particularly near the high-gradient regions close to the walls. Even a higher Reynolds number case would reveal the difference more profoundly, owing to the fact that secondary vortices come into existence or become stronger. The artificial dissipation intensity factors are chosen to be $K_4 = K_6 = 1/2048$ to minimize the impact on the solutions.

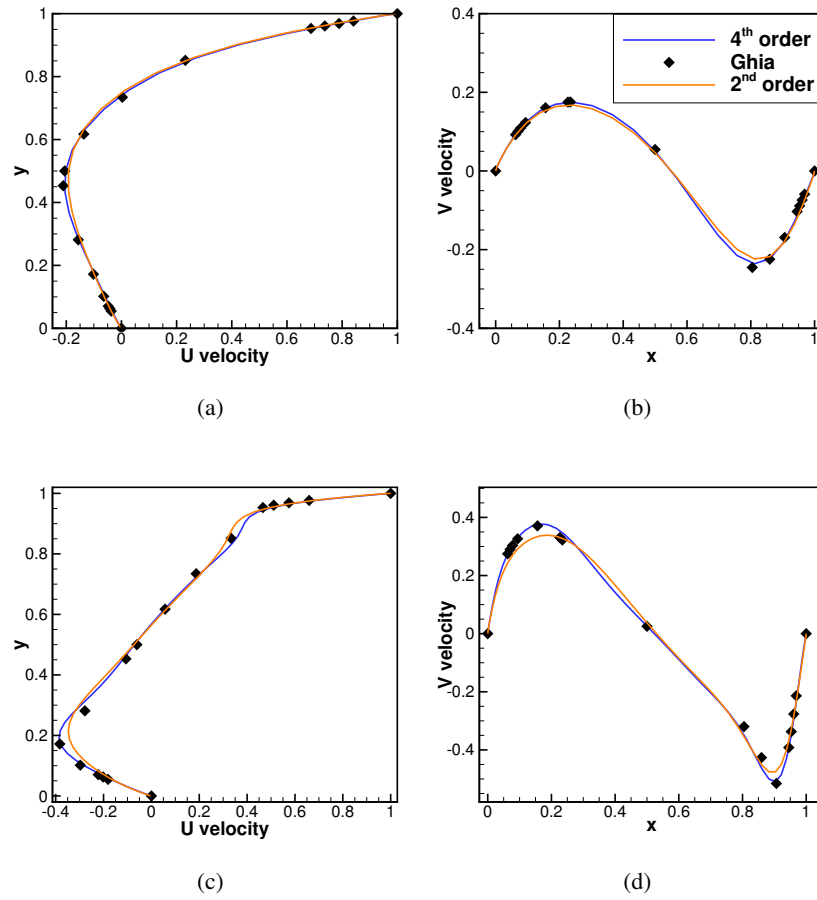


Figure 3.9: Geometric centerline (a), u-velocity (b) v-velocity comparison at $Re = 100$ (25×25 grid points) and (c,d) at $Re = 1000$ (49×49 grid points) with Ghia's data ([129])

3.1.7 Turbulent flow on flat plate

Testing of Spalart-Allmaras one-equation model explained in section 2.4.2 is performed on flat plate with $L = 1$ m and $Re_L = 5 \times 10^6$. The mesh used is exactly the same with the one used in the laminar case (see Figure 3.6). The Figure 3.10a compares the friction coefficient with the results of the NASA CFL3D code [130] and a fine mesh solution with the current code, whereas Figure 3.10b depicts the comparison of the boundary layer velocities in dimensionless units with the law of wall ($\kappa = 0.41$, $B = 5.0$. See [131]) at two locations ($x = 0.2$ and $x = 0.97$ m). Both graphs prove that satisfying agreement is achieved even with a comparably coarse mesh thanks to use of fourth-order accuracy. Furthermore, grid convergence seems to be achieved even on the coarse (69×49) mesh. At the leading edge of the plate, the abrupt oscillations on the friction coefficient is due to the underresolved boundary layer at those locations, obviously. The extremely fine mesh solution of CFL3D together with the fine mesh of the current solver however, captures the curve decently. The velocity profiles also reveal that close to the leading edge the accuracy decreases.

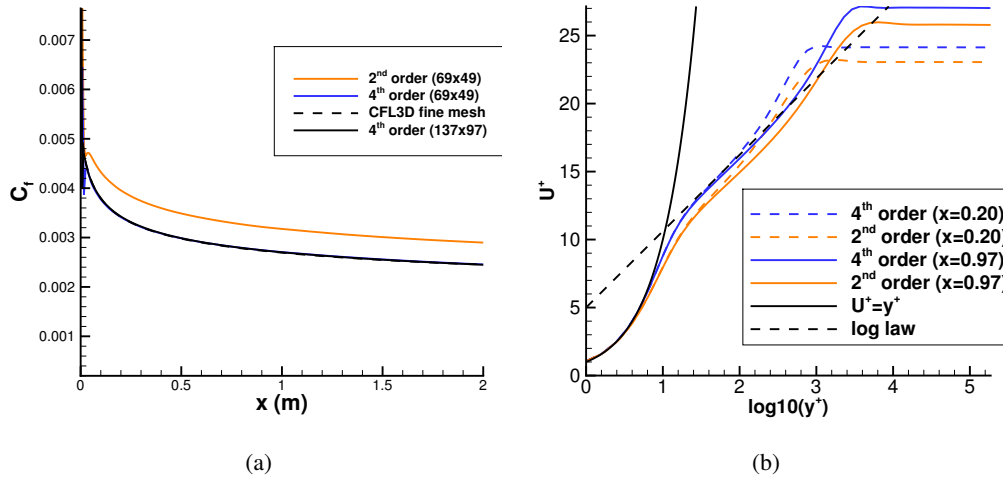


Figure 3.10: (a) Friction coefficient results of fine-mesh CFL3D (545×385) and the current code (69×49), (b) dimensionless boundary layer velocity and the law of the wall at $x = 0.97008$ m location

3.2 Code Verification in 3-D using Method of Manufactured Solutions

It is not an easy task to validate compressible Navier-Stokes equations in 3-D since there is hardly an exact solution to the governing equations, if at all. The only way known is to make simplifications such as incompressibility at low Mach numbers, and study simple flows as done in the previous sections (which are in the literature referred as “validation” rather than verification[132]). Nevertheless, the simple flows usually have zero first and second derivatives of velocity in some directions, overlooking the validation of some aspects of the whole discretization. At this point, one can “manufacture” an exact solution, which necessitates some modifications to the equations, instead of trying desperately to find an exact solution to a physical problem governed by the original system of partial differential equations. Method of Manufactured Solutions (MMS) is a versatile tool to verify the solution of a given code, such that any aspect of a solver can be evaluated separately to identify possible mistakes in the code. More importantly, it is quite convenient to perform an order of accuracy analysis, since the exact solution is already known (or determined) from the beginning. Verification of the observed order of accuracy on a smoothly-mapped non-uniform mesh would verify the discretization methods and the code comprehensively. In fact, it is the recommended acceptance test for code verification, since it is the most sensitive test to coding mistakes [133]. In this section, MMS is intended to be utilized to verify the order of accuracy of the code being developed. The procedure of MMS is summarized as follows [132]:

- Choose a -preferably smooth- solution a priori
- Operate the solution on the governing equations to obtain some source terms
- Modify the code to include the source terms, initial solution and boundary conditions
- Solve the modified equations on several levels of refinement
- Perform discretization error analysis by taking second norm of the error globally

- Calculate observed order of accuracy and compare with the formal order of accuracy and check if they match.

A solution similar to that proposed by Veluri et.al.[134] is chosen and implemented as stationary boundary condition:

$$\phi(x, y, z) = \phi_0 + \phi_x f_s\left(\frac{a_{\phi x} \pi x}{L}\right) + \phi_y f_s\left(\frac{a_{\phi y} \pi y}{L}\right) + \phi_z f_s\left(\frac{a_{\phi z} \pi z}{L}\right) \quad (3.3)$$

with the coefficients and the sinusoidal functions (f_s) chosen as tabulated in the article by Veluri et.al.[134]. In this report, the ultimate aim is to obtain the formal order of accuracy on non-uniform grid using the full-feature 3-D equations, i.e. compressible Navier-Stokes equations. It will verify all aspects of the targeted solver simultaneously: convective flux, viscous flux, artificial dissipation, compressibility, third dimension effects, and even boundary conditions. Verification of the time-accurate solutions is left as a future work.

Figure 3.11 depicts the verification results of the 3-D code using a manufactured solution. The code proved to work perfectly with all features active (DRP, artificial dissipation, viscosity), achieving fourth-order accuracy on the nonuniform set of grids (see Figure 3.11a). Solely verifying the solver in full-feature mode automatically verifies all aspects of the code, thus nullifies separate tests. In fact, there had been an error in the 3-D code, detected and corrected in the results shown (see Figure 3.11b).

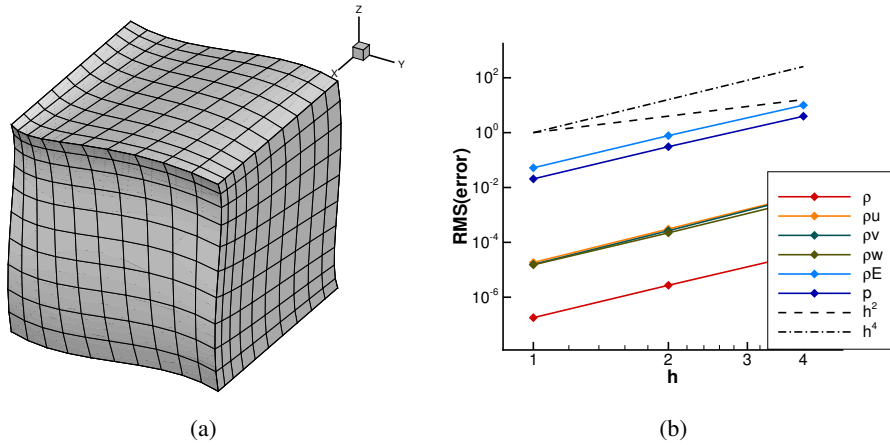


Figure 3.11: Full Navier-Stokes fourth-order DRP solution of the manufactured case (b) on non-uniform grid (a)

CHAPTER 4

UNSTEADY TURBULENT FLOW BENCHMARK PROBLEMS

This chapter covers validation and evaluation of the unsteady flow solver through several turbulent benchmark problems, as to influence of the turbulence models and the numerical scheme. Firstly, a highly detached flow around an airfoil is considered, where detached-eddy simulation is inherently competent. Then, decaying isotropic homogeneous turbulence case is considered to assess the low dispersion and low dissipation merits of the solver combined with the subgrid model. Lastly, a turbulent channel flow benchmark case is solved to test resulting shear and velocity profile obtained by turbulence model in wall-bounded flows.

4.1 NACA0012 airfoil at $\alpha = 45^\circ$

A highly separated airfoil case, which is a great challenge for a turbulence model, has been tested to inspect the DES model at its best. For this case, only ZDES model is tested because ZDES and SLADDES models are expected to behave similar for such a highly separated flow. An O-type mesh of $193 \times 101 \times 31$ grid points, respectively in wall-tangent, wall-normal, and spanwise directions are used with a span of one chord length (See Fig.4.1). Periodic conditions are set in the span limits. A time step of $\Delta t = 0.005c/U_\infty$ is chosen for the dual-time algorithm and the residuals are allowed to drop around three orders, using a fixed number of 40 subiterations. Figure 4.2 shows streamlines and isosurface plots of Q -criterion= 0. In the isosurface plot, highly 3-D nature of the flow is evident. In Figure 4.3, change of lift and drag coefficients are shown with respect to dimensionless time. The averaged values of C_L and C_D are compared with measurements as well as with another DES result from

literature in Table 4.1. Note that the prescribed Reynolds number of the experimental results [135, 136] and the current results slightly differ from that of the DDES and URANS results by Im&Zha [136]: $Re = 2 \times 10^6$ and $Re = 1.3 \times 10^6$, respectively. Nevertheless, Reynolds number effect is known to be trivial at strongly separated high Reynolds number flows ($Re > 10^5$).

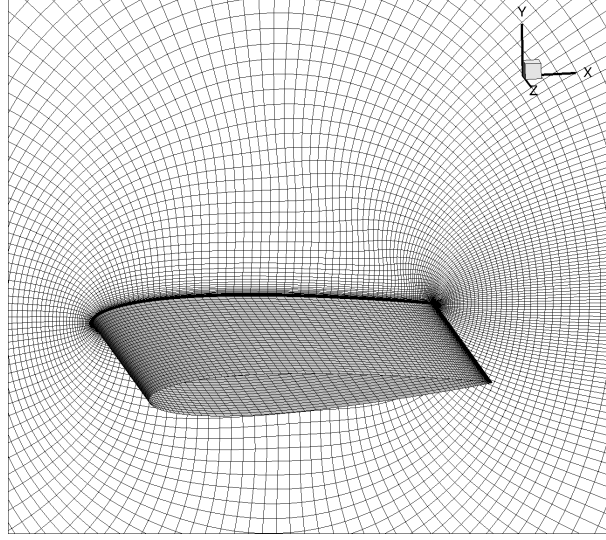


Figure 4.1: Mesh around NACA0012 airfoil ($193 \times 101 \times 31$ points, first cell height $y^+ \approx 1$)

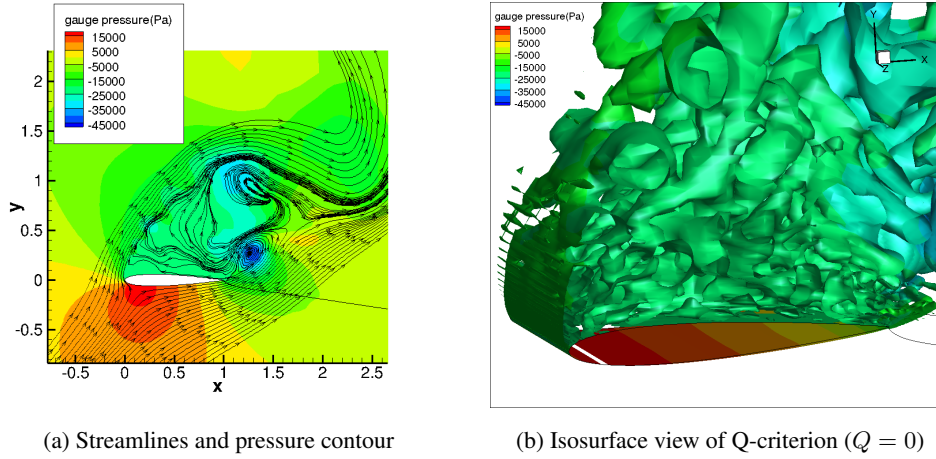


Figure 4.2: Instantaneous views from the NACA0012 airfoil simulation (at $\alpha = 45^\circ$, $Re = 2 \times 10^6$, $M = 0.5$)

Table 4.1: Lift and drag coefficients of NACA0012, $M = 0.5$, $Re = 2 \times 10^6$, $\alpha = 45^\circ$

	C_L	C_D
experiment [135, 136]	1.168	1.109
current (ZDES)	1.151	1.169
DDES [136]	1.087	1.076
DES [136]	1.086	1.075
URANS [136]	1.432	1.421

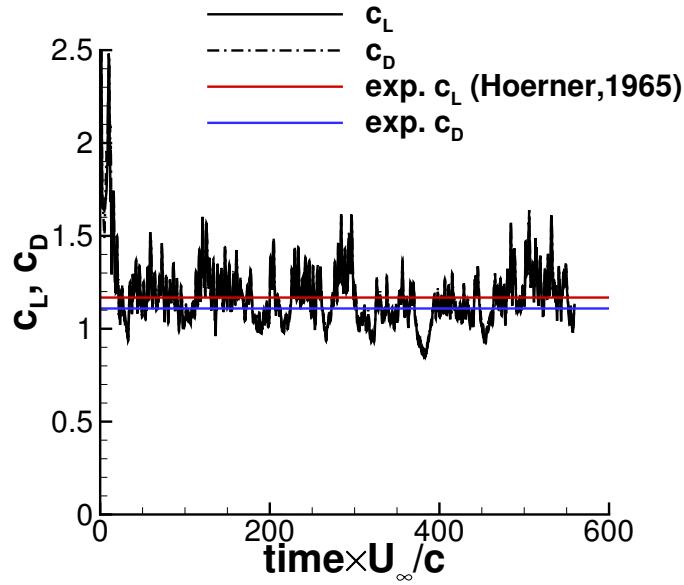


Figure 4.3: Lift and drag coefficients of NACA0012 vs. time ($M = 0.5$, $Re = 2 \times 10^6$, $\alpha = 45^\circ$)

4.2 Decaying homogeneous-isotropic turbulence

Decaying isotropic turbulence benchmark case is widely accepted for turbulence model calibration purposes and examining dissipation impact of numerical schemes. It provides a fundamental test ground for turbulence validation at a minimal computational cost. An unpublished set of data is available freely which is commonly known as Wray1997 DNS data [137, 138]. It provides well-resolved DNS simulation results on a 512^3 grid of cubic box of 2π length on a side, having been verified by former

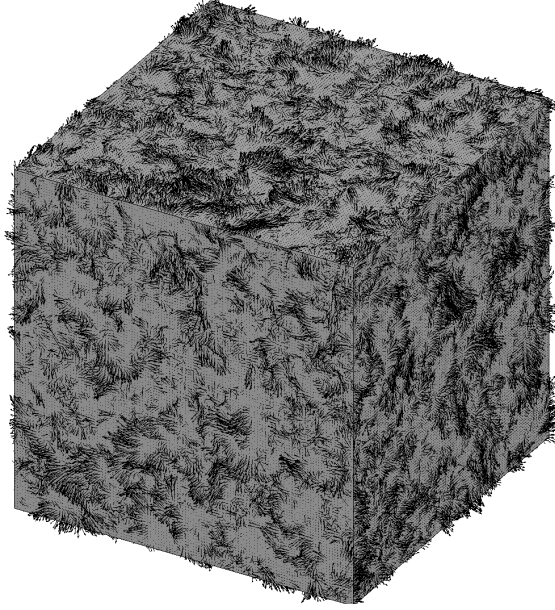


Figure 4.4: Velocity vector field by the DNS of Wray [137]

empirical findings [139].

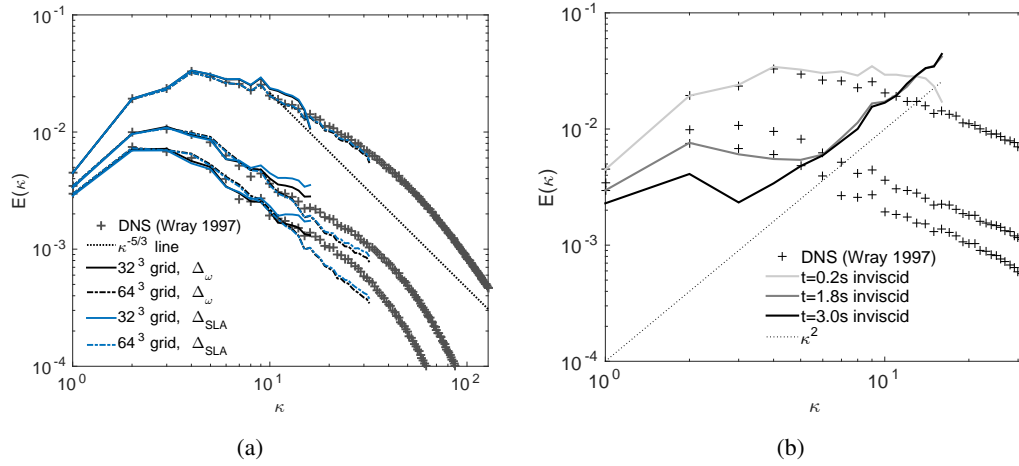


Figure 4.5: Energy spectra of an initially isotropic turbulence at three time levels: a) ++; DNS results on 512^3 grid (known as Wray1997 unpublished data set), --; current solution on 32^3 grid, ---; current solution on 64^3 grid, b) inviscid solution

Figure 4.5a demonstrates the success of the current solver in both DES approaches as compared with the Wray1997 DNS data. The two grids employed in the present test consist of 32^3 and 64^3 cells, respectively. The initial flow field is mined from the available data with 128^3 cells [137] (see Figure 4.4), through sharp truncation into

32^3 cells. At three different times, energy spectra are compared with the DNS results. A fixed time step is used for both grids which corresponds to a Courant number of 0.1 for the coarse grid. The turbulence models appear to benefit even on a coarse mesh greatly from low numerical dissipation and dispersion characteristics of solver. Note that for all the cases, the standard value of the DES model constant is adopted ($C_{DES} = 0.65$). In fact, further calibration might be necessary for the new length scale definition Δ_{SLA} .

Figure 4.5b demonstrates an evaluation of dissipation error of the scheme for the 32^3 grid. A low dissipative scheme obeys the κ^2 rule on higher wavenumbers [26]. Indeed, both low dissipation and dispersion nature and proper modeling of the subgrid turbulence are crucial in calculation of broadband noise levels where turbulent scales and accurately capturing of the energy cascade play an important role.

4.3 Turbulent flow in a channel ($Re_\tau = 395$)

In this section, the ZDES(*imode* = 2) and the SLADDES turbulence model is tested through a channel flow case which is considered as a challenging unsteady test case. For such a case in fact, instead of finite volume methods, very high accurate spectral methods are widely employed [140] in DNS framework because numerical dissipation usually overcomes the initiation and growth of turbulence in the channel. For such a case, DES is mostly considered incompetent because it enables use of coarser grids, which comes with higher numerical dissipation preventing initiation of instabilities. Nevertheless, the low dissipation nature together with fourth-order accuracy of the current method should handle these problems. Apart from numerical dissipation concerns, modeling of the boundary layer might delay growth of fluctuations in a pure DES (DES97) or DDES because of the dissipation by the eddy viscosity.

The case is setup with a friction velocity Reynolds number of $Re_\tau = 395$, in a domain $2\pi H \times 2H \times \pi H$ composed of $32 \times 64 \times 32$ cells by taking the channel half-height $H = 1$ m. The flow is initialized with a laminar Poiseuille flow corresponding to a bulk Mach number of $M_b = 0.2$, and bulk Reynolds number of $Re_b = 6875$. Driving the flow to give a constant mass flux (i.e. constant Re_b) necessitates application of

a constant body force in x -direction as a function of Re_τ and Re_b . Some synthetic turbulence, composed of Fourier composition of many wave numbers in a coherent fashion [86, 87], is induced on the initial flow field to stimulate transition. A time step of $\Delta t = 0.0145H/a_\infty$, where a_∞ is the freestream acoustic speed, is used for all the simulations. LDDRK5 [106], which is an optimized explicit Runge-Kutta time stepping, is employed. The computations are advanced from the initial state until wall shear values are settled around a mean. Afterwards, data is collected for about 900 dimensionless time to compute statistics of turbulence. Note here that no artificial dissipation is used in the no-model simulation, whereas a tiny amount is included in the ZDES and SLADDES ($k_6 = 1/1024$).

Table 4.2 shows computed friction Reynolds number values of several approaches. SLADDES and ZDES approaches implemented in the high-order solver prove success with quite close Re_τ to the nominal value, even on such a coarse mesh. Interestingly, Re_τ is predicted more accurately without use of any model, even more accurate than what a LES approach with a regularization model could achieve. What's more, simulation without a model happened to give a better prediction of friction Reynolds number than a DNS solution [140]. This, however, does not make sense simply because, the no-model simulation solely represents effects of the resolved scale fluctuations, whereas the DNS aims to resolve them all. This situation can be explained through an error trade-off mechanism, which is also observed in some other under-resolved simulations using symmetry-preserving schemes [141, 59]. Note also that the numerical dissipation may work as a sub-grid eddy viscosity in a crude manner, literally deeming the simulation an implicit large-eddy simulation. Alas, the numerical dissipation is not an easily controllable term most of the time, despite recent efforts towards controlling it for LES by making use of various numerical methods (see the review “monotonically implicit LES” (MILES) [52]).

In the framework of ZDES, the switching between LES and RANS modes at an instant in the channel is visualized in Figure 4.6. As expected, employment of RANS is ensured in the attached boundary layer and LES zone is activated in the outer flow. The dark region in the contour plot solely represents the LES zone with LES-type sub-grid length-scale (Δ_{vol} or Δ_ω), whereas the light region corresponds to both RANS mode (using d_{wall}) and DDES mode (using Δ_{max}). The same visualization could be

Table 4.2: Computed friction Reynolds number Re_τ with several approaches. Channel dimensions are $L_x = 2\pi H$; $L_y = 2H$; $L_z = \pi H$. The nominal value dictated by body force is $Re_\tau = 395$

	Δx^+	Δy_{min}^+	Δy_{max}^+	Δz^+	$N_x \times N_y \times N_z$	Re_τ
DNS [140]	10.0	–	6.5	6.5	$256 \times 193 \times 192$	392.2
LES [59]	38.5	2.6	40.7	19.3	$64 \times 64 \times 64$	386.0
SLADDES (current,fine)	38.5	2.6	40.7	19.3	$64 \times 64 \times 64$	395.5
SLADDES (current)	77.0	2.6	40.7	38.6	$32 \times 64 \times 32$	396.1
ZDES (current)	77.0	2.6	40.7	38.6	$32 \times 64 \times 32$	399.9
ZDES (current, no Ψ)	77.0	2.6	40.7	38.6	$32 \times 64 \times 32$	400.6
no model (current)	77.0	2.6	40.7	38.6	$32 \times 64 \times 32$	395.1

performed in a backward facing step case as well, since it is a more challenging case for a hybrid method [31].

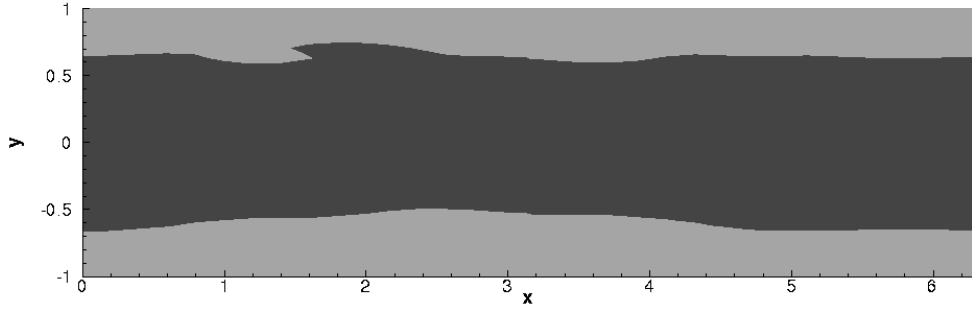


Figure 4.6: Visualization of LES (dark region, $f_d \geq 0.8$) and RANS (light region, $f_d \leq 0.8$) zones of ZDES ($imode = 2$) at an instant at $z = 0$

Sample visualization of turbulent structures obtained via SLADDES at an instant in the channel is shown in Figure 4.7. It is interesting to observe that turbulent fluctuations are sustained even on such a coarse mesh. Figure 4.8 shows the contour of the function F_{KH} (see Eq. 2.38,2.40). In the dark regions, due to existence of purely 2-D shear, the function reduces by one order of magnitude so that eddy viscosity is reduced dramatically to enable Kelvin-Helmholtz instabilities.

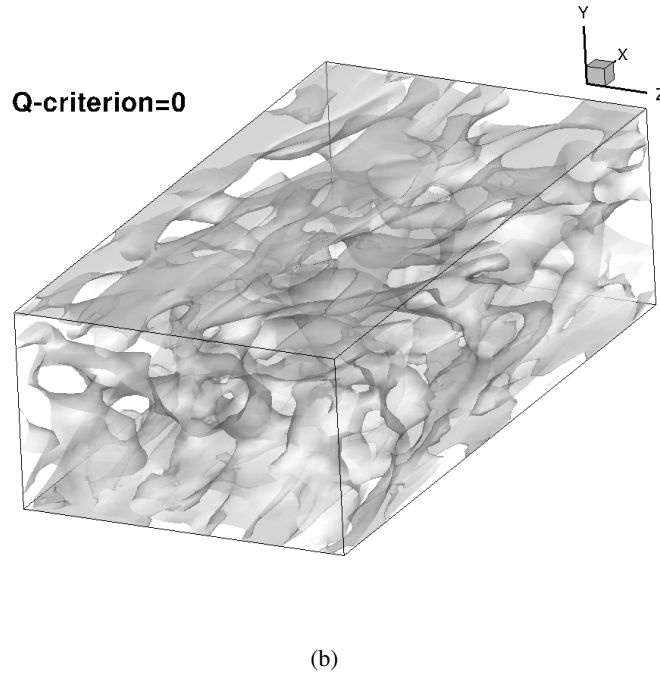
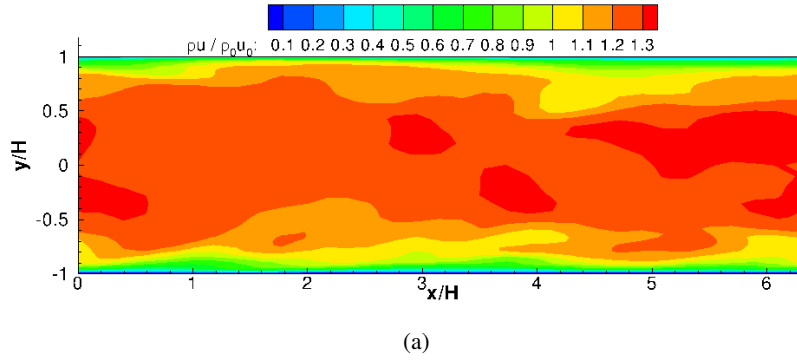


Figure 4.7: Using SLADDES on grid $32 \times 64 \times 32$ (a) Instantaneous x -momentum field, (b) an iso-surface of Q-criterion

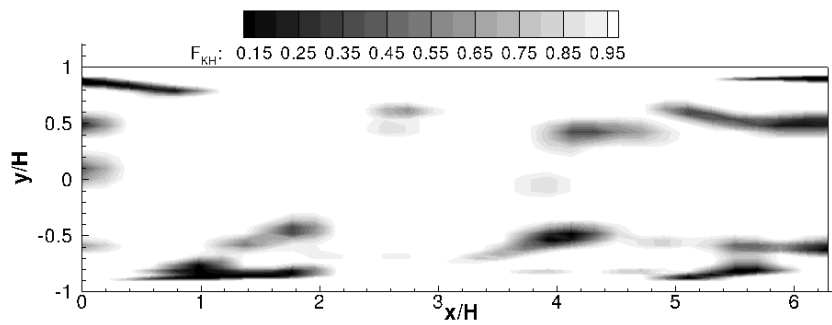


Figure 4.8: Visualization of subgrid length scale reduction in SLADDES approach on grid $32 \times 64 \times 32$

Figure 4.9a compares the dimensionless velocity profile and Reynolds stress diagonal components with the reference DNS solution. As seen, the velocity profiles both by ZDES and SLADDES suffer a slight log-layer mismatch. SLADDES with a finer mesh (see Table 4.2) is also assessed, where mismatch occurs to a lesser extent. This misalignment of the log-layer and viscous layer, which stems from insufficient turbulent kinetic energy feed from the modeled layer to the resolved layer, has also been observed in wall modeled LES approaches [142], and hybrid LES/RANS approaches [143, 32]. In WMLES approaches with wall-stress models, the solution to the mismatch problem is simply grid convergence of the LES region [37]. However, in hybrid LES/RANS approaches where grid convergence is not easy to speak of, other cares must be taken. For example in zonal approaches, a proper small-scale forcing is applied at the interface [33] through either synthetic turbulence or imported DNS data. As to the seamless (i.e. nonzonal) hybrid LES/RANS approaches, improved DDES (IDDES) solves this issue [103, 11] proposing some empirical functions to tailor the eddy viscosity in the buffer layer between the RANS and LES regions. Another notable fix for the mismatch is alteration of the LES model constant, specifically in the wall vicinity, so that eddy viscosity is modified and the mismatch is subdued [144]. Note that in this study, a fix for the log-layer mismatch is out of the scope.

In Figure 4.9b-d, it can be seen that the Reynolds stress terms are under-predicted considerably as compared with the DNS profiles, except for the no-model simulation and the ZDES (without Ψ). Clearly, smaller Reynolds stress terms are expected due to the fact that part of the Reynolds stresses are represented by the calculated eddy viscosity rather than fluctuations directly. In fact, there is a balance between modeled and resolved Reynolds stresses depending on grid refinement and Reynolds number [145]. The no-model simulation naturally lacks the eddy viscosity, whereas the exception by ZDES (without Ψ) probably is related with the severe log-layer mismatch.

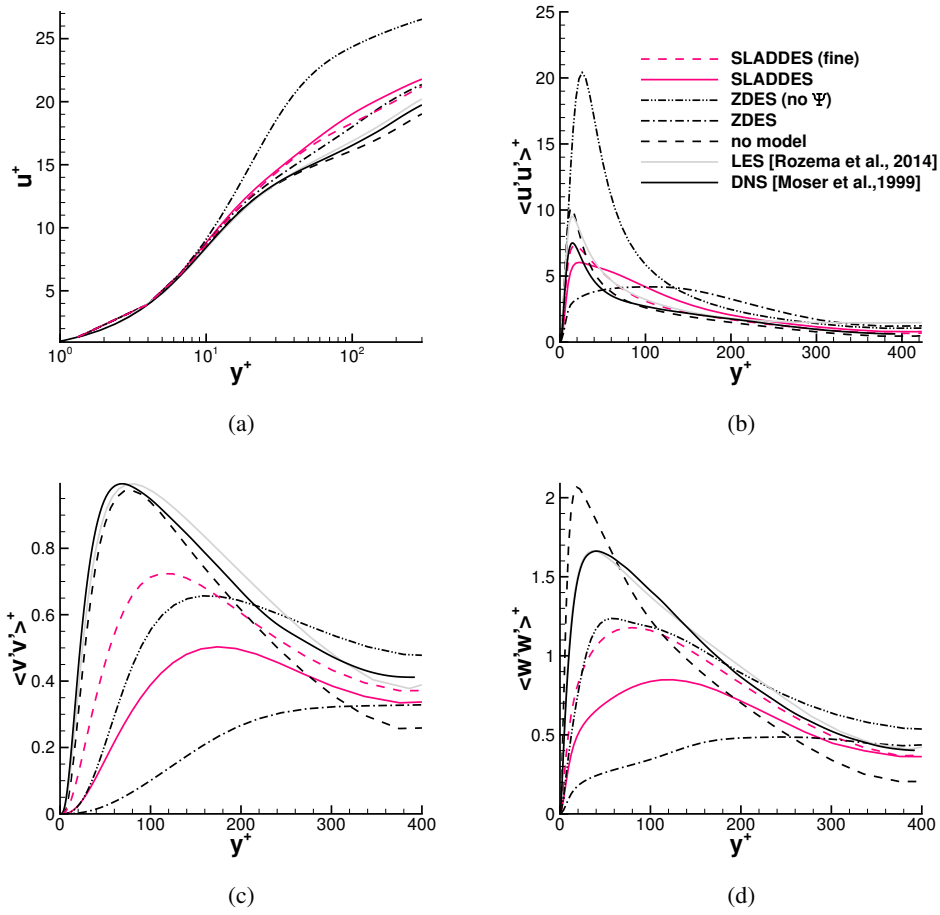


Figure 4.9: Dimensionless mean velocity profile (a) and Reynolds stress terms (b,c,d)

CHAPTER 5

AEROACOUSTIC COMPUTATIONS AROUND AIRFOILS

This chapter covers the acoustic noise prediction around airfoils. Firstly, development and validation of the acoustic analogy tool is presented. Then, airfoil self-noise of NACA0012 in a flow with $Re = 416000$, $M = 0.116$ and attack angle of 5.4° is investigated. Although this case neither corresponds to a typical wind turbine foil nor to wind turbine typical range of Reynolds numbers, it is considered as an affordable and accessible benchmark for such simulations, involving both laminar and turbulent boundary layers at the same time. A more realistic wind turbine blade section in a high-Re flow case is left as the next step for such simulations.

Generation and propagation of noise is based on the flow solver described in Chapter 2 and the acoustic solver presented in this chapter, respectively. In fact, this is a DES-FWH hybrid noise prediction approach which is practical for prediction at distant microphone locations.

5.1 Development of the Frequency-domain Ffowcs Williams-Hawkings Solver

In differential form, the FW-H equation is given as follows [68]

$$\left(\frac{\partial^2}{\partial t^2} - c_0^2 \frac{\partial^2}{\partial x_i \partial x_i} \right) (H(f) \rho') = \frac{\partial^2}{\partial x_i \partial x_j} (T_{ij} H(f)) - \frac{\partial}{\partial x_i} (F_i \delta(f)) + \frac{\partial}{\partial t} (Q \delta(f)) \quad (5.1)$$

where $f = 0$ defines the surface, outside of which a solution is sought for. The primed variables are perturbed values around the free-stream conditions, and the subscript 0 represents free stream values. H is Heaviside; and δ is Dirac delta function. $T_{i,j}$, F_i and Q represent quadrupole, dipole and monopole source terms, respectively. The

source terms are given as,

$$T_{ij} = \rho u_i u_j + p \delta_{ij} - \tau_{ij} - c_0^2 \rho' \delta_{ij} \quad (5.2a)$$

$$F_i = (p \delta_{ij} - \tau_{ij} + \rho u_i (u_j - v_j)) \frac{\partial f}{\partial x_j} \quad (5.2b)$$

$$Q = (\rho_0 v_i + \rho (u_i - v_i)) \frac{\partial f}{\partial x_i} \quad (5.2c)$$

In the above equations, while u_i is the local flow velocity, v_i represents FW-H surface velocity, δ_{ij} is Kronecker delta, and τ_{ij} is the viscous stress tensor which is generally neglected. The derivative $\partial f / \partial x_i$ is nothing but the surface normal vector.

The solution to the Equation 5.1 can be obtained through Green function of the wave equation. 3-D time-domain solution was formulated efficiently by Farassat [146], whereas 2-D and 3-D frequency-domain solutions were demonstrated in Lockard's studies [88, 72]. Comparison of both approaches showed that the frequency-domain solution proves to be more efficient [147]. Another charming aspect of the frequency-domain approach is that the derivatives in the formulation can be obtained analytically rather than numerically. Alas, the frequency-domain formulation might require large amount of memory since all the time period needs to be stored before performing a FFT. In the absence of the volumetric term however, the memory requirements should not make a trouble. Therefore, in this study, the frequency-domain approach is adopted.

Assuming rectilinear motion of the surface in constant speed ($f = f(\mathbf{x} + \mathbf{U}t) = 0$), performing Galilean transformation from (\mathbf{x}, t) to (\mathbf{y}, \bar{t}) where $y_i = x_i + U_i t$; $\bar{t} = t$ and transforming to frequency domain, and lastly, performing Prandtl-Glauert transformation, the ultimate form of the equation for a permeable moving surface yields density perturbation at an observer location for a given frequency [72]:

$$\begin{aligned} H(f) c_0^2 \rho'(\mathbf{y}, \omega) = & - \int_{f>0} T_{ij}(\boldsymbol{\xi}, \omega) H(f) \frac{\partial^2 G(\mathbf{y}; \boldsymbol{\xi})}{\partial \xi_i \partial \xi_j} d\boldsymbol{\xi} \\ & - \oint_{f=0} F_i(\boldsymbol{\xi}, \omega) \frac{\partial G(\mathbf{y}; \boldsymbol{\xi})}{\partial \xi_i} ds \\ & - \oint_{f=0} i\omega Q(\boldsymbol{\xi}, \omega) G(\mathbf{y}; \boldsymbol{\xi}) ds \end{aligned} \quad (5.3)$$

where \mathbf{y} and $\boldsymbol{\xi}$ denote the observer and source coordinates, respectively. As the density perturbation ρ' is computed, the acoustic pressure p' at the observer location \mathbf{y} can

be found by $p'(\mathbf{y}, \omega) = c_0^2 \rho'(\mathbf{y}, \omega)$. Note that flow velocity on the surface $U_i = -v_i$ is used instead of the surface velocity v_i . The transformed source terms in perturbation velocity form are found as

$$F_i = (p\delta_{ij} + \rho(u_i - U_i)(u_j + U_j) + \rho_0 U_i U_j) \frac{\partial f}{\partial y_j} \quad (5.4a)$$

$$Q = (\rho(u_i + U_i) - \rho_0 U_i) \frac{\partial f}{\partial y_i} \quad (5.4b)$$

The quadrupole term T_{ij} does not change in the transformations.

In Prandtl-Glauert transformed coordinates $(\bar{x}, \bar{y}, \bar{z})$, Green function for wave equation for $M < 1$ is conveniently given by,

$$G(\mathbf{y}; \xi) = \frac{-1}{4\pi d} e^{-ik(d-M\bar{x})/\beta^2} \quad (5.5)$$

where the transformations can be derived as,

$$\begin{aligned} \bar{x} &= (x - \xi) \cos \alpha \cos \phi + (y - \eta) \sin \alpha + (z - \zeta) \cos \alpha \sin \phi \\ \bar{y} &= -(x - \xi) \sin \alpha \cos \phi + (y - \eta) \cos \alpha + (z - \zeta) \sin \alpha \sin \phi \\ \bar{z} &= -(x - \xi) \sin \phi + (z - \zeta) \cos \phi \\ d &= \sqrt{\bar{x}^2 + \beta^2(\bar{y}^2 + \bar{z}^2)} \end{aligned}$$

where $i = \sqrt{-1}$, M is Mach number, k is wavenumber (ω/c_0), and β is Prandtl-Glauert factor ($\sqrt{1 - M^2}$). The angles are defined such that $\sin \alpha = U_2 / \sqrt{U_1^2 + U_2^2 + U_3^2}$, $\tan \phi = U_3 / U_1$.

Equation 5.3 requires integration of the sources over the surface and the entire volume outside the surface, which is prohibitively expensive. Fortunately, the quadrupole source (or, the Lighthill stress tensor, T_{ij}) can be neglected because it is not significant in most low-Mach cases [79]. In flows like jets, however, where shear layers and wakes could cause refraction of waves, the quadrupole source term becomes dominant. Still, the need to bother the costly volume integration can be evaded, provided the integration surface encompasses all the important quadrupole sources. Note that propagation of the relevant waves up to the surface must be allowed by the mesh resolution. Another caution should be given to the fact that the eddies passing through the integration surface cause spurious noise, some remedies to which are proposed in the literature [79, 72].

Integrations in Equation 5.3 are performed simply by midpoint approximation, that is, the surface is approximated with panels, and the integrands are computed numerically through multiplication of midpoint value of the integrands with the area of the panels. Computation of the sources on the panels and integration of Equation 5.3 are parallelized via shared memory model of OpenMP [89], with respect to panel indices and frequency indices, respectively.

5.2 Validation of the Ffowcs Williams-Hawkings Solver

In this section, a basic setup used by Lockard [147] for testing of the monopole and another similar setup for dipole computations are chosen to validate the current implementation. The implementation is efficiently parallelized using shared-memory principles.

5.2.1 A Moving Monopole Source

A monopole moving in $-x$ direction, or equivalently placed in a uniform flow in $+x$ direction, is described by complex velocity potential as

$$\phi = A \frac{1}{4\pi d} \exp [i(\omega t - k(d - Mx)/\beta^2)] . \quad (5.6)$$

The field variables can be calculated from the complex potential through formulations, $p' = -\rho_0(\partial\phi/\partial t + U_0\partial\phi/\partial x)$, $u'_i = \partial\phi/\partial x_i$, and $\rho' = p'/c_0^2$, taking only the real parts. The analytic definition of the sound field will be used for both the required field on the FW-H surface and the sound at the observer position. Suppose a monopole fluctuating in a single tone with $\omega l/c_0 = 4\pi/46$ placed in a flow with $M = 0.5$. The source amplitude is taken as $A/(l^2 c_0) = 0.01$. The FW-H integration surface is chosen to be a sphere of radius $5l$ created with 97×49 points in equally spaced azimuthal and polar angles (see Figure 5.1). 64 time samples are generated for two periods of the wave. Since the quadrupole term is neglected, mean values must be subtracted from the monopole and dipole sources (Q , F_i), even though windowing is not relevant in this problem. Unless the mean values are subtracted, the computed pressure signal will falsely fluctuate around a nonzero mean, i.e. in frequency domain, $\omega = 0$ solution of the sound pressure ($p'(0)$) will turn out to be nonzero.

Figure 5.2 compares the analytic solution of sound pressure signal and root-mean-square with the computed solution by the FW-H implementation at an observer located at radial location $R = 50l$ and a polar angle of $\theta = 0$. The agreement validates the implementation at least for monopole problems in uniform flow.

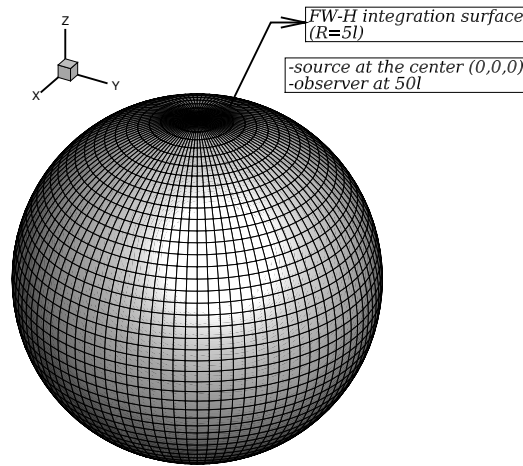


Figure 5.1: Ffowcs Williams-Hawkins solver integration surface for the moving dipole and monopole source tests

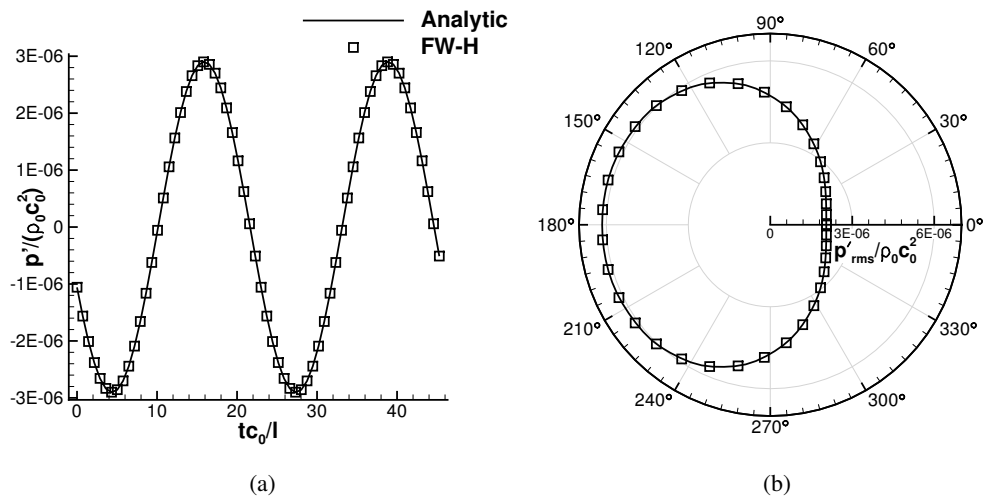


Figure 5.2: (a) Pressure signal at $R = 50l$, $\theta = 0^\circ$ and (b) directivity comparison of a monopole solution in a mean flow with $M = 0.5$.

5.2.2 A Moving Dipole Source

Similar to the monopole source, a moving dipole source located on the origin can be defined by the velocity potential function,

$$\phi = \frac{\partial}{\partial y} \left\{ A \frac{1}{4\pi d} \exp [i(\omega t - k(d - Mx)/\beta^2)] \right\} \quad (5.7)$$

The uniform flow is in the $+x$ direction whereas the dipole axis lies in y direction. Magnitude, frequency, integration surface and observer location are all taken equal to those of the monopole source in Section 5.2.1. The integration surface is chosen to be exactly the same sphere as in the monopole case (Figure 5.1), but with an observer at a polar angle $\theta = 90^\circ$ instead. The signal and directivity computations (Figure 5.3) prove almost identical results with the analytical solution, which validates the implementation for the dipoles as well. Remember that the quadrupole term in the formulation is ignored throughout this study.

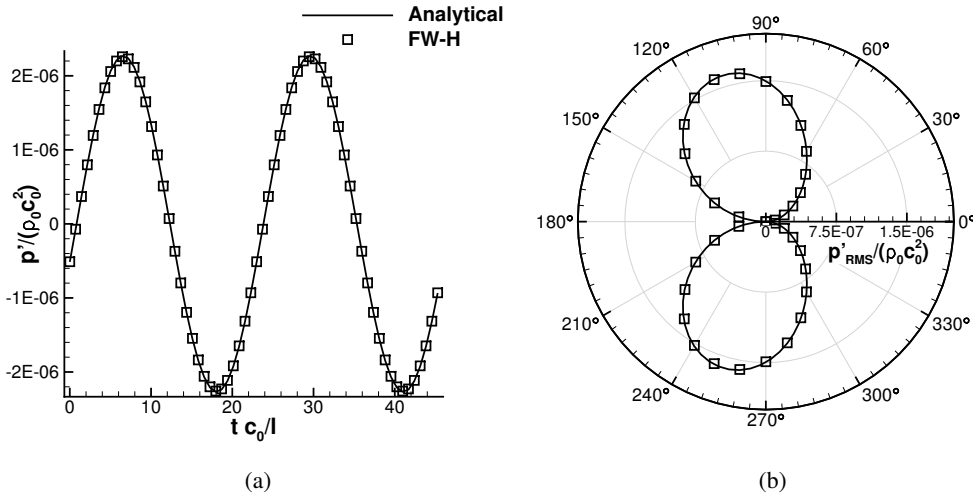


Figure 5.3: (a) Pressure signal at $R = 50l$, $\theta = 100^\circ$ and (b) directivity comparison of a dipole solution in a mean flow with $M = 0.5$.

5.3 Signal Processing Framework

In real applications, source fluctuations are not necessarily fully periodic, because data from CFD computations is usually of limited time due to computational restric-

tions. Besides, sources, especially those due to turbulence, are necessarily quite complex consisting of many frequencies of different origins such that a continuity between the beginning and end points of any record segment can not be possible. Hence, the source signals must be filtered before the FFT for reliable Fourier transformations. A regular Hanning filter (a.k.a. Hanning window), or a modified one that is adjusted to keep the signal on the mid-period intact [88], should be appropriate for the purpose of making the signals periodic. The weighting of the regular Hanning filter on a given sample n on the discrete signal is given as

$$w_n = 0.5 \left[1 - \cos \left(2\pi \frac{n-1}{N} \right) \right] ; n = 1, N \quad (5.8)$$

where N is the total number of samples in the window. Hanning windows have less impact on frequency resolution and accuracy of amplitudes on the spectrum than other window types.

An energy correction should also be made, through simply dividing the FFT output by $\sqrt{(1/N) \sum w_n^2}$, i.e. scaling the weightings by the root-mean-square. The window must be applied after subtracting the mean values from each segment. Afterwards, the mean values could be restored if necessary. Nonetheless, subtracting the mean values solely modifies the zero frequency component, which is not relevant if the spectrum is the desired output. In this study, only the regular Hanning filter is considered for use on segments with 1/2 overlap (see Figure 5.4 for a demonstration). Resulting power spectra from all the segments are then averaged to get an estimate of the power spectrum. This procedure is called the Welch's method [148], also known as the periodogram method.

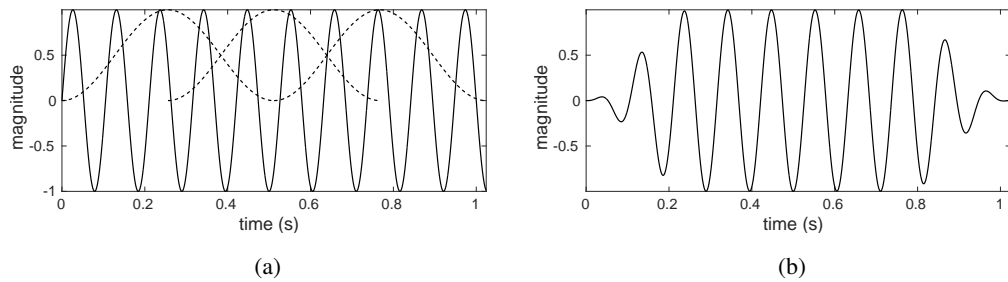


Figure 5.4: a) a sinusoidal signal (solid curve) and 1/2 overlapping Hanning windows (dashed curves); b) corresponding filtered signal

The signal processing procedure is summarized below:

1. Arrange the time record in $1/2$ overlapping segments and compute the sources via Equations 5.4,
2. If needed, remove the trend in each segment by subtracting the linear least squares fit,
3. Subtract the mean values of each segment from themselves to obtain pure perturbations,
4. Filter the segments via Hanning filter,
5. FFT of the signals in the segments,
6. Integrate the FWH equation in frequency domain (Equation 5.3) for each segment separately to obtain pressure spectra on the observer location,
7. Take average of the power spectra to get an estimate of pressure spectrum on the observer,
8. If desired, perform an octave band transformation of the spectrum.

Note that detrending the signal is only necessary when there is an undesirable trend on the signal, in order to prevent possible bias on the low frequency end of the spectrum. Ideally, a statistical convergence of the variables should be achieved, which would obviate the need for detrending. Note again that an octave band transformation is necessary when comparisons are to be made with some other results or measurements that have different frequency resolution. That is, the results or measurements must be of the same band representation (e.g. one-third octave band) for the comparison to be meaningful.

5.4 Seo and Moon's Long Span Correction to Sound Pressure Levels

In most of the RANS/LES applications, simulation of full span of an airfoil or body is not usually affordable. It is common to take only a section of the body's span as the simulation domain. Then, far-field sound pressure level of the full span is estimated

from the radiation contribution of the simulated section. The most common approach is the Kato correction [149], which is based on pressure coherence based on space-time cross-correlation of a selected point on the body surface, on the premise that the sources radiate sound independently if the coherence length is smaller than the simulated span. On the contrary, they radiate sound together if the coherence is immense, i.e. they radiate nearly-cylindrical waves. However, this method partly lacks justification, because frequencies with intermediate coherence lengths are treated somewhat ad-hoc. Moreover, there is not a well-defined way to estimate the coherence length from the coherence function.

Seo and Moon [150] proposed an improvement over the Kato *et al.*'s [149] box-car function. The improvement is mainly on frequencies with the intermediate coherence lengths, while the asymptotic values are equal to those of the Kato correction. In a simplified form, the correction to sound pressure level (SPL) is given as,

$$SPL_{corr.} = \begin{cases} 10\log_{10}(N), & L_c/L_s \leq 1/\sqrt{\pi} \\ 10\log_{10}(L_c/L_s) + 10\log_{10}(\sqrt{\pi}N), & 1/\sqrt{\pi} < L_c/L_s < N/\sqrt{\pi} \\ 20\log_{10}(N), & L_c/L_s \geq N/\sqrt{\pi} \end{cases} \quad (5.9)$$

where L_c is the coherence length, L_s is the simulated span, and $L = NL_s$ is the full span of the body. The derivation of the above formulation (see [150]) is based on a special definition of coherence. That is,

$$\gamma_{ij}(\omega) = \frac{\overline{\Re(\hat{p}'_i \hat{p}'_j^*)}}{|\hat{p}'_i| |\hat{p}'_j|} \quad (5.10)$$

where \hat{p}'_i is the Fourier transform of the radiated acoustic pressure by subsection i on an observer, $(\cdot)^*$ stands for conjugate, and $\Re(\cdot)$ denotes real part of a complex input. This definition directly reflects phase differences between the two subsections for a given angular frequency (ω) so that it can be termed as “acoustic spanwise coherence function”. The overline denotes ensemble average over all computed phase differences with equal span distance (Δz_{ij}). The radiated acoustic pressures by the subsections (\hat{p}'_i, \hat{p}'_j) can be obtained by Curle's analogy using the surface pressure signal on the body [151]. The coherence length L_c is estimated from a Gaussian fit to

the coherence function, that is,

$$\gamma(\Delta z_{ij}) \approx \exp\left(-\frac{\Delta z_{ij}^2}{L_c^2}\right) \quad (5.11)$$

In fact, the derivation of the correction in Eq. 5.9 is based on this approximation. Details of the methodology are given in the Seo & Moon's work [150]. It is also successfully applied on a trailing edge noise simulation case in their following work [152].

5.5 Noise Prediction from NACA0012 ($\alpha = 5.4^\circ$, $Re = 416000$, $M = 0.116$)

A low-Mach airfoil case is investigated for direct noise computation using SLADDES. The parameters of the flow setup is imported from one of the untripped experiments by Brooks *et al.* [15], with a chord length of 15.24 cm., and a span of 45.72 cm. (run no. 159, see figure 55(c) in [15]). In the simulations, the span is taken as one tenth of the chord length. Three mesh configurations with O-topology, listed in Table 5.1, are considered. The grid G1 only served the purpose of a preliminary trial mesh to qualitatively observe difference between ZDES (*imode* = 2) and SLADDES. G2 is an intermediate trial mesh for turbulence stimulation. The grid G3 (see Figure 5.5) on the other hand, being the finest grid, is designed for noise computation. The trailing edge is rounded with radius $r/c = 2.6 \times 10^{-3}$, while in the Brooks' experiments, the trailing edges are reported to be sharpened not less than $r/c \approx 0.2 \times 10^{-3}$, and in Wolf and Lele's wall-resolved LES study [24], it is rounded with $r/c \approx 1.5 \times 10^{-3}$. The LES results [24] will be used as a benchmark as well as the Brooks' measurements. In the LES [24] study, maximum grid spacings on the airfoil in wall units are given as $\Delta x^+ \approx 60$, $\Delta y^+ \approx 0.5$ and $\Delta z^+ \approx 20$ with a total number of around 45 million grid points.

Firstly, simulations are started with a large time step to eliminate initial large transients quickly. Afterwards, the time step is reduced to $\Delta t = 4 \times 10^{-3} c/a_\infty$, corresponding to 1.8×10^{-6} s. Crudely, this corresponds to the stability limit –for an explicit time stepping scheme– of a cell located towards the edge of the boundary layer over the trailing edge suction side (approximately at $\delta/2.5$), such that any unsteadiness around that cell level can be resolved with a Courant number of around

Table 5.1: Grid configurations considered

Grid	Span extent	Far field	$N_x \times N_y \times N_z$	S.S. Δx_{max}^+	Δy_{min}^+	Δz^+
G1	$0.1c$	$26c$	$257 \times 97 \times 49$	450	1	42
G2	$0.1c$	$42c$	$281 \times 169 \times 49$	250	1	42
G3	$0.1c$	$120c$	$641 \times 201 \times 41$	106	0.7	50

1.6. Specifically, the trailing edge boundary layer thickness on suction side was measured in the experiment [15] as $\delta/c \approx 0.045$, while the mentioned cell layer is at $y/c \approx 0.018$. Thus, WMLES mode is expected to take over towards the trailing edge with proper time resolution about that cell layer. It is useful to note again in this simulation that a dual time stepping strategy with preconditioning and matrix artificial dissipation is employed for time integration so that the numerical difficulties of scale disparity between acoustics and flow is subdued on this low-Mach-number flow, and dissipation is properly scaled.

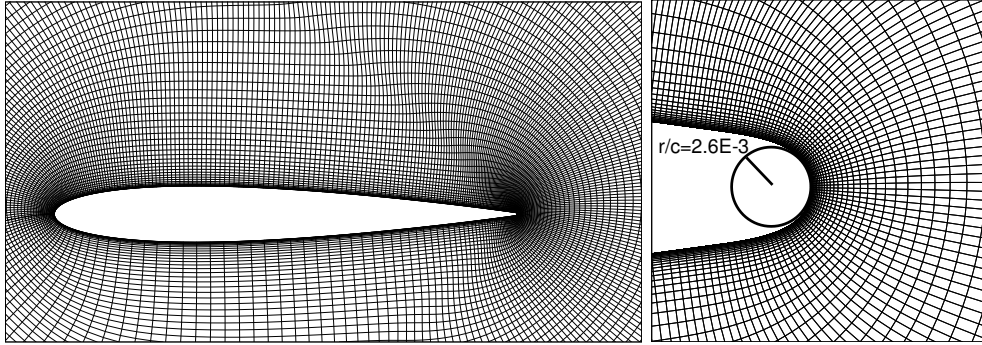


Figure 5.5: *left*: asymmetric mesh setup G3 (every 2nd point shown); *right*: Rounded trailing edge of NACA0012 (all points shown)

Figure 5.6 demonstrates how ZDES (*imode* = 2) approach on the preliminary mesh (G1) fails to support the synthetically generated turbulent structures, while SLADDES approach sustains the fluctuations to some extent, in particular, those emanating from the vicinity of the trailing edge. Hence, only SLADDES results will be presented hereafter.

Figure 5.7 visualizes the coherent structures around the airfoil obtained on the fine

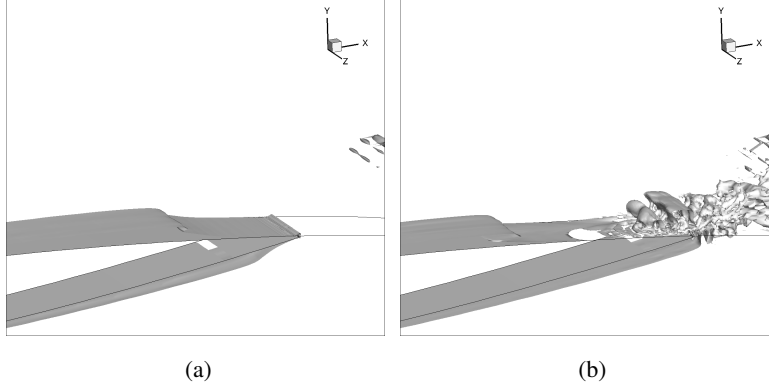


Figure 5.6: A preliminary study on coarse mesh (G1): Q-criterion ($Q = 0$) isosurface around the trailing edge using: a) ZDES, b) SLADDES

mesh (G3). For such structures to occur, synthetically generated initial turbulence (as mentioned in Section 4.3) might be necessary for triggering the fluctuations. Otherwise, they might only emanate from a restricted region. In fact, it was the case on the intermediate mesh (G2), while there was no such necessity on the fine mesh (G3). Another idea developed for triggering the fluctuations was temporarily disabling the boundary layer shield (described in Eq. 2.40). This also has proven success in the intermediate mesh (G2), and may be used where stimulation by synthetic turbulence turns out to be inaccessible or inadequate. Note that all the results presented hereafter are only obtained on the G3 grid, which is designed for noise computation.

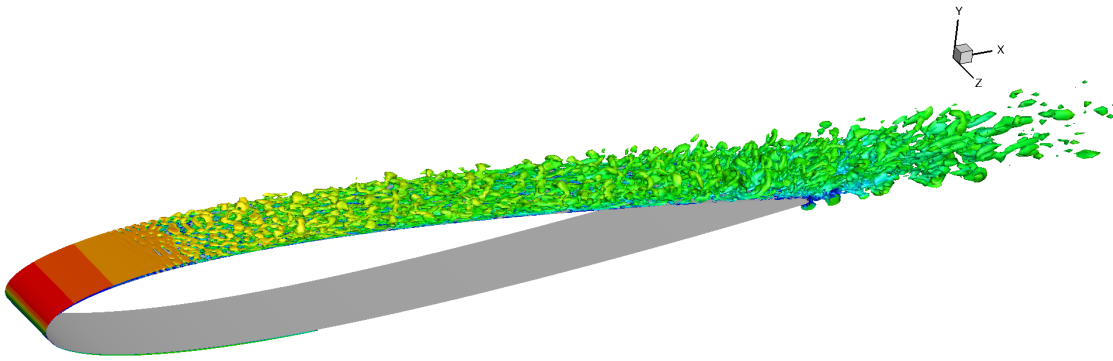


Figure 5.7: Isosurface of λ_2 colored by velocity magnitude (grid G3)

Figure 5.8a compares the pressure coefficient distributions obtained over the airfoil

surface by the SLADDES approach, an LES study [24] and the XFOIL code. SLADDES approach agrees particularly well with XFOIL where natural transition is allowed as well. In the LES results however, the boundary layer is tripped on the suction side through suction/blowing (see the kinks). Transition phenomenon can be more clearly observed in the skin friction plot (see the steepness in Figure 5.8b). Once again, the results compare fairly well, except for the transition region on the suction side. Still, natural transition may be deemed successful despite the lack of a transition model. Notice in Figure 5.8b that data on the pressure side is not available from the LES results.

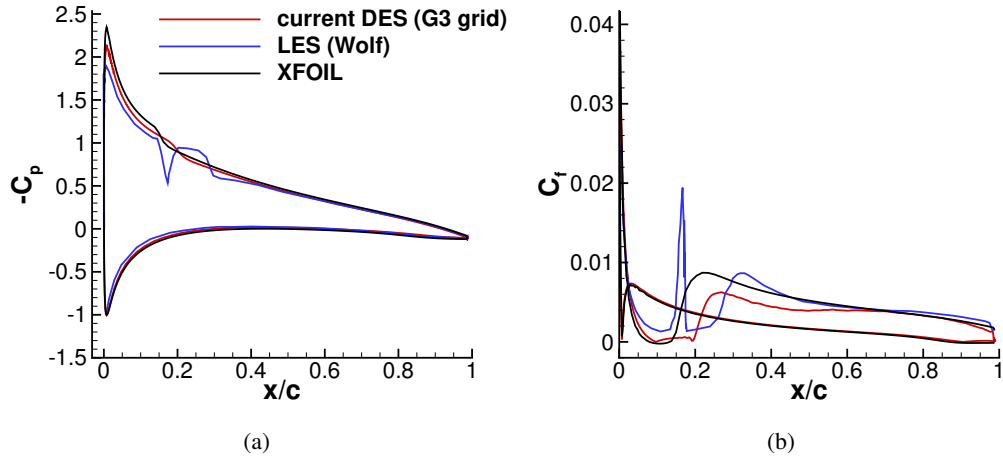


Figure 5.8: $-C_p$ (a) and C_f (b) around the airfoil

In Figure 5.9, the dimensionless velocity profiles on the suction side are shown at various locations. Comparisons indicate a logarithmic layer mismatch over the turbulent boundary layer on the suction side. Actually, an agreement with the law of the wall with a Von Kármán constant of $\kappa = 0.41$ is not expected due to the adverse pressure gradient. Nevertheless, any other law is not observed as well. In fact, $\kappa = 0.35$ law is reported by Wolf [71] in his comprehensive wall-resolved LES study, which apparently does not match with the current DES results. Note that the viscous sublayer is resolved by approximately 6 points, while up to $y^+ = 200$, by around 25 points in total. As pointed out earlier, log-layer mismatch is a problem that remains to be solved for most of the DES methods. A direct solution to this problem should be to ensure an LES level of resolution in the boundary layer, since the problem mainly stems from

lack of energy transfer between the resolved turbulence in the outer layers and the modeled turbulence in the sublayers. Instead, IDDES method [11] in recent years, powered by blending functions between resolved and modeled regions, has proven a sound and affordable solution to the mismatch problem.

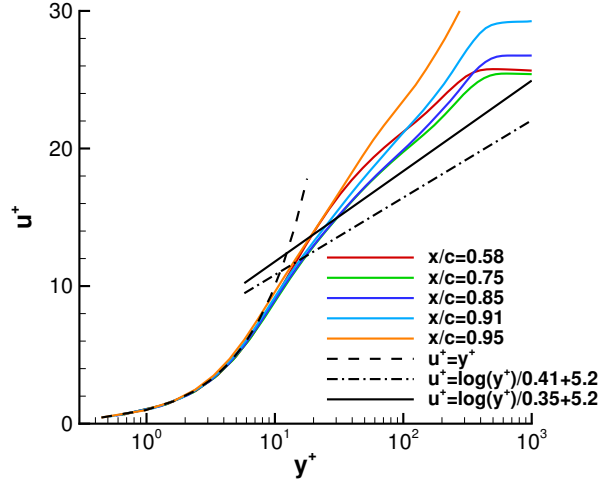


Figure 5.9: Dimensionless velocity profile on the suction side (grid G3)

Figure 5.10 is a demonstration of the acoustic field computed directly from the flow field around the airfoil. A dominant tone is observed to get emitted from the trailing edge, which is due to the vortex shedding from the pressure side laminar boundary layer (see Figure 5.11a). In fact, obtaining that laminar vortex was not straightforward with a DES approach. In an initial attempt, S-A turbulence model in the DES approach produced spurious eddy viscosity on the pressure-side, which disrupted the laminar boundary layer. Hence, the laminar recirculation bubble was not seen in that attempt. In a second attempt, a special approach was devised, where an initial eddy viscosity variable of $\tilde{\nu}/\nu_\infty = 0$ was assigned throughout the domain such that the S-A model can not produce spurious eddy viscosity (any eddy viscosity, indeed). When it came to switch to a small time step as explained above, a very small amount of eddy viscosity distribution ($\tilde{\nu}/\nu_\infty = 10^{-14}$, for example) in a small region close to the leading edge on the suction side, is released artificially for once. Consequently, the S-A model was enabled to produce eddy viscosity in the instabilities of the shear layer on the suction side, resulting in transition to turbulence. Figure 5.11a illustrates the resulting eddy viscosity around the laminar shear layer (or absence thereof) towards

the trailing edge. In addition, Figure 5.11a,b compares the corresponding vortices shedding on the trailing edge with those of the LES study. The resemblance is close. Notice that the trailing edge shapes of the current simulation and the LES study does not perfectly conform to each other.

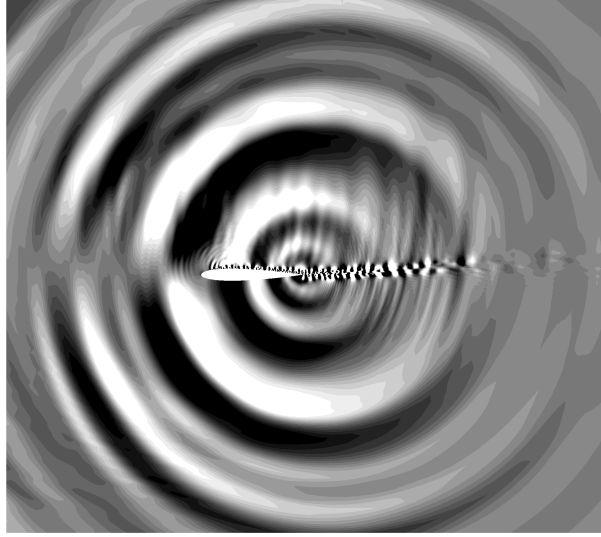


Figure 5.10: Contour of $\partial p/\partial t$ around the airfoil (G3 grid)

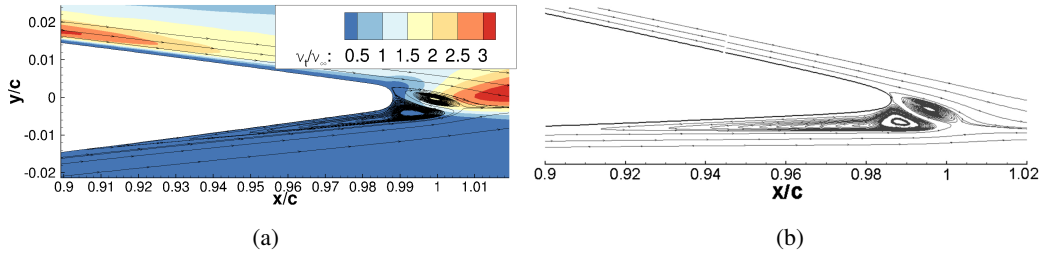


Figure 5.11: a) Mean eddy viscosity contour and streamlines in the vicinity of the trailing edge, b) streamlines of the recirculation bubble obtained via LES [24] appearing on the trailing edge

For far-field noise predictions, the time accurate data from the SLADDES on three selected surfaces (see Figure 5.12a) are collected as 20 frames of 64 samples with 1/2 overlap and processed using Hanning window. The far field sound level is computed by a frequency domain 3-D Ffowcs Williams-Hawkings solver following Lockard [88], as explained in Section 5.1. Recall that the FW-H implementation explained in Section 5.1 neglects volumetric terms pertaining to quadrupole sources, calculation

of which is usually impractical in realistic 3-D applications. Instead of computing all the volumetric sources, the common approach is to select a surface encompassing significant quadrupole sources effectively. However, the passage of vortices and other non-acoustic entities through the permeable surface induces some error. In fact, error of this kind is canceled by the volumetric sources in the original formulation [72]. For low-Mach flow problems with dominant dipole sources such as the present case however, quadrupole sources are often negligible, as also proven by Wolf for the same case [71]. Therefore, use of the airfoil surface should be the natural choice (surface with $j = 1$ in Figure 5.12a). Still for completeness, results by three different integration surfaces are examined prior to comparing the far-field noise with the measurements. Figure 5.12b compares the noise predictions on an observer location by the sound radiated from the simulated span, based on flow data on the surfaces around the airfoil with various distances. The results considerably differ, particularly at high frequencies. Besides, the hydrodynamic disturbances related with the error at high frequencies are not seemingly resolved up to $j = 90$ surface, where the grid stretching is intense. Avoidance of both the error due to neglecting volumetric sources and under-resolution of the acoustic waves at the same time is not straightforward [72], requiring ad-hoc remedies. As pointed out earlier, a good compromise for such flows with low Mach number and dominant non-quadrupole sources is to choose the body's surface as the FW-H integration surface. Hence, only the airfoil surface will be considered as the FW-H integration surface hereafter.

The SPL from the simulated span ($L_s = 0.1c$) was scaled to the experimental span ($L = 3c$) according to the Seo&Moon correction [150], which is based on spanwise coherence lengths of frequency components (see Section 5.4). In the current simulation however, obtaining a reliable coherence length information was quite troublesome, probably due to shortness of the simulated span. As Figure 5.13a implies, fitting some of the coherence functions, particularly those around the vortex tone, to a Gaussian distribution for coherence length estimation was not seemingly possible. At those frequencies, it may be well said that the coherence lengths are larger than the simulated span L_s , which greatly affects the SPL correction value. Therefore, another approach was adopted for estimating coherence lengths around the vortex tone. According to Roger *et al.* [153], coherence length distribution over the frequencies for a

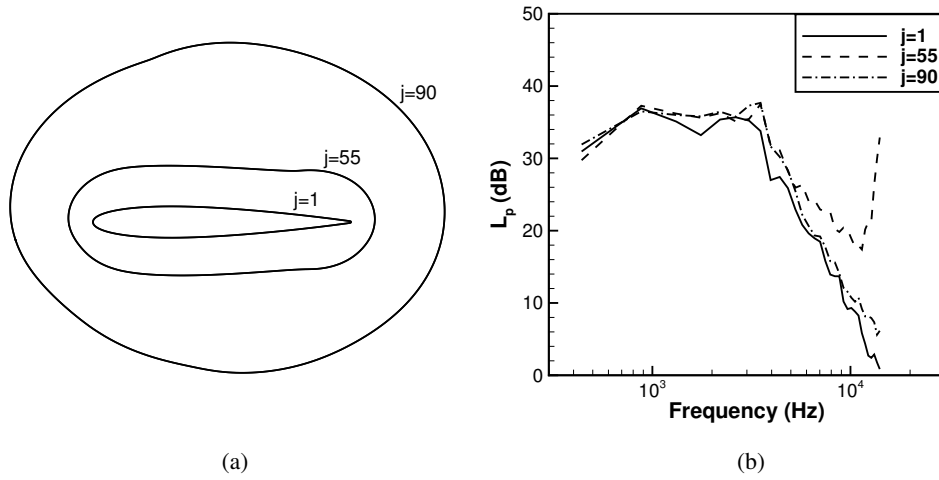


Figure 5.12: a) Surfaces used in FW-H acoustic analogy, b) SPL predictions on the surfaces with $\Delta f = 439.3$ Hz by an observer at $(c, 8c)$ at midspan

vortex-shedding noise can be fit to a function $L_c = L_0 \exp(-A|f - f_0|)$. L_0 and f_0 are the coherence length and frequency of the vortex shedding, A is an adjustable coefficient usually around $A = 0.012$. L_0 is measured as $7h$ for a flat plate with thickness h and zero angle of attack [153]. In the current study, considering the nonzero angle of attack and thickness of the airfoil, $L_0 = 5h$ and $A = 0.003$ are taken roughly, where h is the airfoil thickness. The vortex sound frequency is naturally taken as the frequency of the noise peak emitted by one simulated span L_s , that is $f_0 = 2636$ Hz. The resulting coherence length estimates and corresponding SPL correction values are shown in Figure 5.13b. Figure 5.14 compares SPLs (L_p) obtained by LES [24], SLADDES (using fourth-order DRP on the grid G3, and additionally second-order scheme on the same grid), and the NASA experiment by Brooks *et al.* [15]. The observer is located at the simulated midspan at $(c, 8c)$, the origin being the leading edge. The agreement is good with the selected values except for discrepancies in the low-frequency end. Most probably, it is related with difficulties in the coherence length estimation. Another reason might be the shortness of the simulated span, which could also be a reason for the former reason. On the other hand, the high frequency noise emission predictions agree with the measurements, which shows that the resolution and the numerical approach can sustain generation and propagation of such short waves. The second-order scheme, however, overpredicts the SPL. Both the amplitude of the main

tone and the broadband noise show discrepancies between the experimental measurements. At the current mesh resolution with the second-order scheme, the acoustics sources might be under-resolved. In fact, under-resolution of sources are reported to cause over-prediction of the wall pressure fluctuation intensities, resulting in higher noise levels [154].

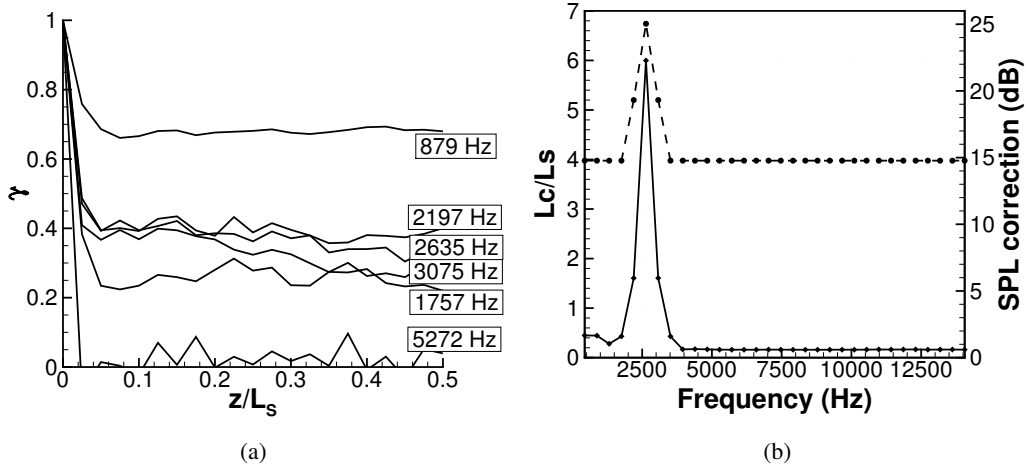


Figure 5.13: a) Spanwise coherence for several frequencies; b) —: coherence length by $L_c = L_0 \exp(-A(|f - f_0|))$ formula, - -: corresponding SPL correction

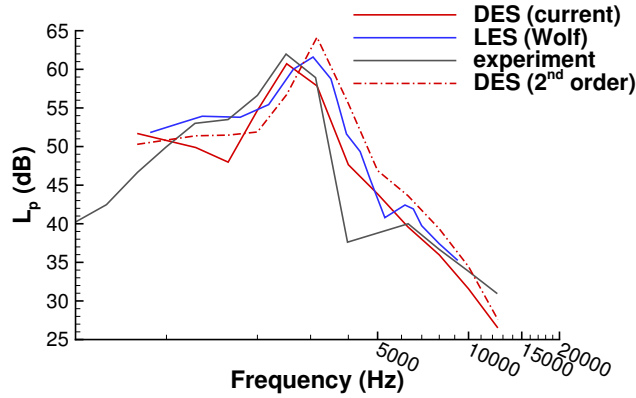


Figure 5.14: Comparison of sound pressure levels at $(c, 8c)$ in third octave bands with NASA experiments [15] and Wolf's LES+FWH results [24]

Figure 5.15 illustrates the directivity pattern of several noise frequencies, at a distance of $r = 8c$. Notice that the directivity computations are done only for the simulated span, that is, no long-span corrections are considered for this plot. The first impres-

sion is that all the patterns are that of dipole sources. The lowest frequency, with a Helmholtz number of $kc = 2.45$, shows a typical dipole directivity of free-space Green's function since $kc < 2\pi$, i.e. a compact source. In contrast, higher frequencies with $kc > 2\pi$ behave like non-compact sources as expected, showing the typical cardioid pattern of a semi-infinite flat plate, i.e. the pattern of half-space Green's function [18]. Basically, non-compact source patterns imply that the phase variation along the acoustic scattering body is significant, whereas it is not, for compact sources. Note that the pattern with Helmholtz number $kc = 7.36$ corresponds to the noise peak for the full span wing in the experiment.

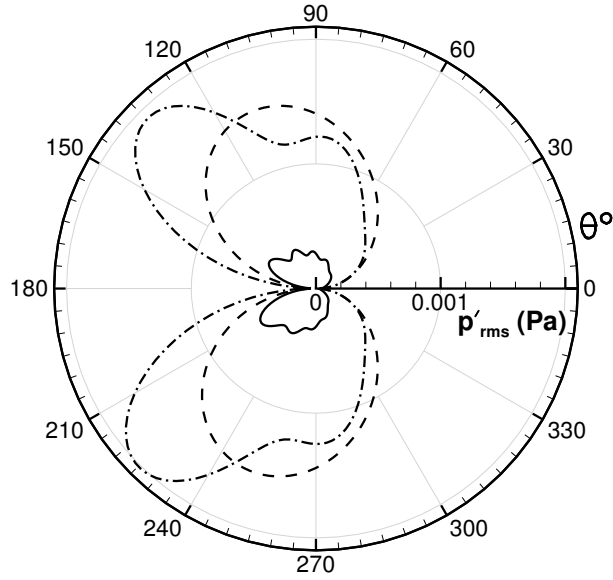


Figure 5.15: Directivity at $r = 1.22$ m ($8c$) distance to the trailing edge. $---$: 879 Hz ($kc = 2.45$), $- \cdot -$: 2636 Hz ($kc = 7.36$), $—$: 5272 Hz ($kc = 14.73$)

CHAPTER 6

CONCLUSIONS

In this thesis, a compressible flow solver, named METUDES, is developed for use in aeroacoustic simulations. The solver is validated through several unsteady turbulent flow cases before being used in investigation of an airfoil trailing-edge noise. This chapter concludes the thesis and proposes some possible directions for further research.

6.1 The Development and Validation of the Flow Solver: METUDES

A 3-D compressible unsteady flow solver has been developed from scratch, for use in noise simulations in METU Department of Aerospace Engineering. Determining noise sources using first principles, i.e. compressible Navier-Stokes equations, requires resolution of turbulence spatially and temporally. Rather than resolving most (or all) of the turbulence, as is the case in LES or DNS approaches, the inner boundary layer is modeled using a RANS method in the framework of DES (i.e. wall-modeled LES mode of DES). This approach is supported by many numerical properties of the solver and turbulence modeling features that allow flow instabilities to occur more easily. In summary, the combined application of

- low-dissipation and low-dispersion fourth-order spatial scheme,
- a low-Mach preconditioned dual-time strategy
- accompanied by matrix dissipation in a blended form,
- a modified Spalart-Allmaras turbulence model rendering the DES model applicable in laminar regions,

- and an enhanced version of DES that improves the subgrid length scale definition such that grid dependency is reduced and Kelvin-Helmholtz instabilities are fostered,
- Erroneous activation of near-wall functions of the SA model in the LES region is prevented using a correction (Ψ) to the subgrid length scale

has been considered promising for turbulence resolving and aeroacoustic purposes even in low-Mach regime. In fact, the major contribution of this thesis is the coalescence of all these features on a flow solver being primarily designed for aeroacoustic purposes.

Two DES improvements, called ZDES and SLADDES, were implemented, and tested in decaying turbulence and channel flow benchmark cases. The solver showed merit in the two cases even on coarse mesh thanks to the low-dissipation and low-dispersion features of the spatial discretization. Specifically in the channel flow case, low dissipation discretization allowed use of very little (or no at all) artificial dissipation so that the no-model simulation without any artificial dissipation behaved like an implicit large-eddy simulation with outstandingly close results to the reference DNS data. In the decaying turbulence case, the energy spectrum matched the DNS results even on the coarse mesh. Nevertheless, the DES model constant appears to be in need of recalibration for the new length scale definition.

The present DES models have two drawbacks: log-layer mismatch, and spurious eddy viscosity production in the laminar region of the boundary layers. Although not tackled in this study, the former was effectively solved by Shur *et al.* [11] in the framework of improved detached-eddy simulation (IDDES). The latter is currently cleared thanks to the modified version of the Spalart-Allmaras model, through assigning an initial eddy viscosity of zero in the laminar side of the airfoil and instantly injecting a small amount on the side where transition is expected, as demonstrated in Section 5.5. Ideally, this should be handled automatically by coupling the turbulence model with a transition model. Even without a transition model, it is shown in the airfoil problem in Section 5.5 that the location of transition to turbulence agree with the XFOIL prediction, which might be considered as another contribution of this thesis.

6.2 Noise Simulation around NACA0012 Airfoil Section

A frequency-domain Ffowcs Williams-Hawkings solver, that permits permeable integration surfaces, is developed for noise prediction on an observer position. Then, a low-Mach airfoil trailing-edge noise prediction with a Reynolds number of 416,000 is attempted. As a matter of fact, this is a challenging task involving resolution of turbulent boundary layer. Nonetheless, both the aerodynamic and noise predictions are in agreement with measurements and benchmark simulations. Yet, scaling of the resulting noise levels on the observer to the full-span wing is somewhat ambiguous. Despite the fact that the benchmark LES study [24] claims the sufficiency of a span of 0.1 chords, the current study does not. The same simulation with a doubled span-length is in progress to illuminate this issue.

6.3 Recommendations For Future Research

The present solver needs further development for better use in aerodynamic and aeroacoustic problems. The immediate developments are recommended as

- A correction to log-layer mismatch is needed. Among others, implementation of IDDES [11] would be the most popular choice.
- Overset grid blocks will enhance the use of the solver, paving the way to simulation of more complex problems with less grid points.
- Incorporation of advanced convergence acceleration techniques could lower computational effort in the dual-time evolution.
- For minimal reflections from far boundaries, implementation of Navier-Stokes characteristic boundary conditions, or definition of an effective sponge zone will enhance acoustic results.
- For this specific couple of numerical setup and subgrid length scale definition, a recalibration of the subgrid-scale constant (C_{DES}) on the decaying turbulence benchmark might be valuable.

As a future investigation that makes a good use of the present methodology, simulation of a rotating wind turbine blade will be tempting. Accurate prediction of both flow and noise around the blade will be a supportive contribution to wind energy science.

Countless future research starting from this methodology can be contemplated. Since the recent progress in hybrid RANS/LES models looks promising towards prospects of affordable and accurate prediction of complex flows in industrial range of Reynolds numbers, mitigating certain deficiencies of the DES models demands further understanding and research. The remedies proposed to mitigate the deficiencies usually complicate the model even further, bringing forth more ad-hoc coefficients and tunable variables. For example, IDDES [11] is a major complexity over DDES, despite the effectiveness on log-layers. The author believes that some alternative remedies to the log-layer mismatch issue should be proposed. For instance, development of a variable DES coefficient (C_{DES}) could address the issue with less complexity. Another future research might be on coupling the current DES model with a transition model. The current configuration is a convenient testbed for such purposes because the turbulence model equation permits zero eddy viscosity.

REFERENCES

- [1] G. Raman, “Wind turbines: clean, renewable and quiet?,” *Noise Notes*, vol. 9, no. 1, pp. 35–44, 2010.
- [2] C. Arakawa, O. Fleig, M. Iida, and M. Shimooka, “Numerical approach for noise reduction of wind turbine blade tip with earth simulator,” *Journal of the Earth Simulator*, vol. 2, no. 3, pp. 11–33, 2005.
- [3] S. Oerlemans, P. Sijtsma, and B. Mendezlopez, “Location and quantification of noise sources on a wind turbine,” *Journal of Sound and Vibration*, vol. 299, no. 4-5, pp. 869–883, 2007.
- [4] C. Doolan, D. J. Moreau, and L. A. Brooks, “Wind turbine noise mechanisms and some concepts for its control,” *Acoustics Australia*, vol. 40, no. 1, pp. 7–13, 2012.
- [5] A. Tadamas and M. Zangeneh, “Numerical prediction of wind turbine noise,” *Renewable Energy*, vol. 36, no. 7, pp. 1902–1912, 2011.
- [6] S. Hosseini, R. Vinuesa, P. Schlatter, A. Hanifi, and D. Henningson, “Direct numerical simulation of the flow around a wing section at moderate reynolds number,” *International Journal of Heat and Fluid Flow*, vol. 61, Part A, pp. 117 – 128, 2016. SI TSFP9 special issue.
- [7] N. Sezer-Uzol and L. N. Long, “3-d time-accurate CFD simulations of wind turbine rotor flow fields,” *AIAA paper*, vol. 394, p. 2006, 2006.
- [8] O. Marsden, C. Bogey, and C. Bailly, “Direct noise computation of the turbulent flow around a zero-incidence airfoil,” *AIAA journal*, vol. 46, no. 4, pp. 874–883, 2008.
- [9] P. Spalart, W. Jou, and M. Strelets, “Comments on the feasibility of les for wings, and on a hybrid rans/les approach,” in *Advances in DNS/LES, First AFOSR International Conference on DNS/LES, Greyden*, 1997.

- [10] U. Piomelli and E. Balaras, “Wall-layer models for large-eddy simulations,” *Annual review of fluid mechanics*, vol. 34, no. 1, pp. 349–374, 2002.
- [11] M. L. Shur, P. R. Spalart, M. K. Strelets, and A. K. Travin, “A hybrid rans-les approach with delayed-DES and wall-modelled LES capabilities,” *International Journal of Heat and Fluid Flow*, vol. 29, no. 6, pp. 1638–1649, 2008.
- [12] C. Mockett, M. Fuchs, and F. Thiele, “Progress in des for wall-modelled les of complex internal flows,” *Computers & Fluids*, vol. 65, pp. 44–55, 2012.
- [13] J. Larsson and Q. Wang, “The prospect of using large eddy and detached eddy simulations in engineering design, and the research required to get there,” *Philosophical Transactions of the Royal Society of London A: Mathematical, Physical and Engineering Sciences*, vol. 372, no. 2022, 2014.
- [14] ANSYS, “Fluent flow solver software.” <http://www.ansys.com>. Accessed: November-2016.
- [15] T. F. Brooks, D. S. Pope, and M. A. Marcolini, *Airfoil self-noise and prediction*, vol. NASA-RP-1218. National Aeronautics and Space Administration, Office of Management, Scientific and Technical Information Division, 1989.
- [16] S. Oerlemans, “Wind tunnel aeroacoustic tests of six airfoils for use on small wind turbines,” NREL Subcontract Report 35339, Nationaal Lucht-en Ruimtevaartlaboratorium (NLR), 2004.
- [17] W. Devenport, R. A. Burdisso, H. Camargo, E. Crede, M. Remillieux, M. Rasmick, and P. V. Seeters, “Aeroacoustic testing of wind turbine airfoils,” NREL Subcontract Report 43471, Virginia Polytechnic Institute and State University, 2010.
- [18] J. E. F. Williams and L. H. Hall, “Aerodynamic sound generation by turbulent flow in the vicinity of a scattering half plane,” *Journal of Fluid Mechanics*, vol. 40, no. 4, p. 657–670, 1970.
- [19] M. Howe, “Trailing edge noise at low mach numbers,” *Journal of Sound and Vibration*, vol. 225, no. 2, pp. 211 – 238, 1999.

- [20] M. Wang and P. Moin, “Computation of trailing-edge flow and noise using large-eddy simulation,” *AIAA journal*, vol. 38, no. 12, pp. 2201–2209, 2000.
- [21] E. Manoha, B. Troff, and P. Sagaut, “Trailing-edge noise prediction using large-eddy simulation and acoustic analogy,” *AIAA journal*, vol. 38, no. 4, pp. 575–583, 2000.
- [22] J. Winkler, S. Moreau, and T. Carolus, “Airfoil trailing edge noise prediction from large-eddy simulation: influence of grid resolution and noise model formulation,” in *16th AIAA/CEAS aeroacoustics conference*, p. 3704, 2010.
- [23] J. G. Kocheemoolayil and S. K. Lele, “Large eddy simulation of airfoil self-noise at high reynolds number,” in *22nd AIAA/CEAS Aeroacoustics Conference, Lyon, France, Aeroacoustics Conferences, American Institute of Aeronautics and Astronautics*, May 2016.
- [24] W. R. Wolf and S. K. Lele, “Trailing-edge noise predictions using compressible large-eddy simulation and acoustic analogy,” *AIAA journal*, vol. 50, no. 11, pp. 2423–2434, 2012.
- [25] J. Smagorinsky, “General circulation experiments with the primitive equations,” *Monthly Weather Review*, vol. 91, no. 3, pp. 99–164, 1963.
- [26] C. Mockett, *A Comprehensive Study of Detached Eddy Simulation*. PhD thesis, Technischen Universität Berlin, 2009.
- [27] P. R. Spalart, “Detached-eddy simulation,” *Annual Review of Fluid Mechanics*, vol. 41, pp. 181–202, 2009.
- [28] U. Michel, D. Eschricht, B. Greschner, T. Knacke, C. Mockett, and F. Thiele, “Advanced DES methods and their application to aeroacoustics,” in *Progress in Hybrid RANS-LES Modelling*, pp. 59–76, Springer, 2010.
- [29] M. Strelets, M. Shur, A. Travin, and P. R. Spalart, *The Delay of RANS-to-LES Transition in Hybrid RANS-LES Approaches and Some Recently Proposed Remedies*, pp. 3–21. Springer International Publishing, 2016.
- [30] P. R. Spalart, S. Deck, M. Shur, K. Squires, M. K. Strelets, and A. Travin, “A new version of detached-eddy simulation, resistant to ambiguous grid densi-

- ties,” *Theoretical and computational fluid dynamics*, vol. 20, no. 3, pp. 181–195, 2006.
- [31] S. Deck, “Recent improvements in the zonal detached eddy simulation (ZDES) formulation,” *Theoretical and Computational Fluid Dynamics*, vol. 26, pp. 523–550, 2012.
- [32] L. Davidson and S. Dahlström, “Hybrid LES-RANS: An approach to make LES applicable at high reynolds number,” *International Journal of Computational Fluid Dynamics*, vol. 19, no. 6, pp. 415–427, 2005.
- [33] L. Davidson and M. Billson, “Hybrid LES-RANS using synthesized turbulent fluctuations for forcing in the interface region,” *International Journal of Heat and Fluid Flow*, vol. 27, no. 6, pp. 1028–1042, 2006.
- [34] M. L. Shur, P. R. Spalart, M. K. Strelets, and A. K. Travin, “An enhanced version of des with rapid transition from rans to les in separated flows,” *Flow, Turbulence and Combustion*, vol. 95, no. 4, pp. 709–737, 2015.
- [35] N. Chauvet, S. Deck, and L. Jacquin, “Zonal detached eddy simulation of a controlled propulsive jet,” *AIAA journal*, vol. 45, no. 10, pp. 2458–2473, 2007.
- [36] H. Choi and P. Moin, “Grid-point requirements for large eddy simulation: Chapman’s estimates revisited,” *Physics of Fluids*, vol. 24, no. 1, p. 011702, 2012.
- [37] J. Larsson, S. Kawai, J. Bodart, and I. Bermejo-Moreno, “Large eddy simulation with modeled wall-stress: recent progress and future directions,” *Mechanical Engineering Reviews*, vol. 3, no. 1, 2016.
- [38] P. Moin, J. Bodart, S. Bose, and G. I. Park, “Wall-modeling in complex turbulent flows,” in *Advances in Fluid-Structure Interaction* (M. Braza, A. Bottaro, and M. Thompson, eds.), (Cham), pp. 207–219, Springer International Publishing, 2016.
- [39] S. T. Bose and G. I. Park, “Wall-modeled large-eddy simulation for complex turbulent flows,” *Annual Review of Fluid Mechanics*, vol. 50, no. 1, pp. 535–561, 2018.

- [40] B. Greschner, J. Grilliat, M. Jacob, and F. Thiele, “Measurements and wall modeled les simulation of trailing edge noise caused by a turbulent boundary layer,” *International Journal of Aeroacoustics*, vol. 9, no. 3, pp. 329–355, 2010.
- [41] L. Wang, C. Mockett, T. Knacke, and F. Thiele, “Detached-eddy simulation of landing-gear noise,” in *19th AIAA/CEAS Aeroacoustics Conference*, p. 2069, 2013.
- [42] M. Ghasemian and A. Nejat, “Aerodynamic noise prediction of a horizontal axis wind turbine using improved delayed detached eddy simulation and acoustic analogy,” *Energy Conversion and Management*, vol. 99, pp. 210 – 220, 2015.
- [43] M. L. Shur, P. R. Spalart, and M. K. Strelets, “Jet noise computation based on enhanced DES formulations accelerating the RANS-to-LES transition in free shear layers,” *International Journal of Aeroacoustics*, vol. 15, no. 6-7, pp. 595–613, 2016.
- [44] E. K. Guseva, A. V. Garbaruk, and M. K. Strelets, “Application of DDES and IDDES with shear layer adapted subgrid length-scale to separated flows,” *Journal of Physics: Conference Series*, vol. 769, no. 1, p. 012081, 2016.
- [45] F. de la Puente Cerezo, L. Sanders, F. Vuillot, P. Druault, and E. Manoha, “Zonal detached eddy simulation of a simplified nose landing-gear for flow and noise predictions using an unstructured navier-stokes solver,” *Journal of Sound and Vibration*, vol. 405, pp. 86 – 111, 2017.
- [46] Z. Wang, K. Fidkowski, R. Abgrall, F. Bassi, D. Caraeni, A. Cary, H. Deconinck, R. Hartmann, K. Hillewaert, H. Huynh, N. Kroll, G. May, P.-O. Persson, B. van Leer, and M. Visbal, “High-order cfd methods: current status and perspective,” *International Journal for Numerical Methods in Fluids*, vol. 72, no. 8, pp. 811–845, 2013.
- [47] N. Kroll, H. Bieler, H. Deconinck, V. Couaillier, H. van der Ven, and K. Sorensen, *ADIGMA—A European Initiative on the Development of Adaptive Higher-Order Variational Methods for Aerospace Applications: Results of*

a Collaborative Research Project Funded by the European Union, 2006-2009, vol. 113. Springer, 2010.

- [48] N. Kroll, C. Hirsch, F. Bassi, C. Johnston, and K. Hillewaert, *IDIHOM: Industrialization of High-Order Methods-A Top-Down Approach: Results of a Collaborative Research Project Funded by the European Union, 2010-2014*, vol. 128 of *Notes on Numerical Fluid Mechanics and Multidisciplinary Design*. Springer, 2015.
- [49] A. Kravchenko and P. Moin, “On the effect of numerical errors in large eddy simulations of turbulent flows,” *Journal of Computational Physics*, vol. 131, no. 2, pp. 310–322, 1997.
- [50] A. Vreman, B. Geurts, and J. Kuerten, “Comparison of numerical schemes in large-eddy simulation of the temporal mixing layer,” *International journal for numerical methods in fluids*, vol. 22, no. 4, pp. 297–312, 1996.
- [51] C. Fureby and F. Grinstein, “Monotonically integrated large eddy simulation of free shear flows,” *AIAA journal*, vol. 37, no. 5, pp. 544–556, 1999.
- [52] J. P. Boris, “More for les: a brief historical perspective of MILES,” in *Implicit Large-Eddy Simulation: computing turbulent flow dynamics* (F. F. Grinstein, L. G. Margolin, and W. J. Rider, eds.), pp. 9–38, Cambridge university press, 2007.
- [53] R. Verstappen and A. Veldman, “Symmetry-preserving discretization of turbulent flow,” *Journal of Computational Physics*, vol. 187, pp. 343–368, May 2003.
- [54] J. Kok, “A high-order low-dispersion symmetry-preserving finite-volume method for compressible flow on curvilinear grids,” *Journal of Computational Physics*, vol. 228, pp. 6811–6832, Oct. 2009.
- [55] A. E. Honein and P. Moin, “Higher entropy conservation and numerical stability of compressible turbulence simulations,” *Journal of Computational Physics*, vol. 201, no. 2, pp. 531 – 545, 2004.

- [56] Y. Morinishi, “Skew-symmetric form of convective terms and fully conservative finite difference schemes for variable density low-mach number flows,” *Journal of Computational Physics*, vol. 229, pp. 276–300, Jan. 2010.
- [57] S. Pirozzoli, “Stabilized non-dissipative approximations of euler equations in generalized curvilinear coordinates,” *Journal of Computational Physics*, vol. 230, pp. 2997–3014, Apr. 2011.
- [58] D. Modesti and S. Pirozzoli, “A low-dissipative solver for turbulent compressible flows on unstructured meshes, with openfoam implementation,” *Computers & Fluids*, vol. 152, pp. 14 – 23, 2017.
- [59] W. Rozema, J. Kok, R. Verstappen, and A. Veldman, “A symmetry-preserving discretisation and regularisation model for compressible flow with application to turbulent channel flow,” *Journal of Turbulence*, vol. 15, no. 6, pp. 386–410, 2014.
- [60] C. K. Tam and J. C. Webb, “Dispersion-relation-preserving finite difference schemes for computational acoustics,” *Journal of computational physics*, vol. 107, no. 2, pp. 262–281, 1993.
- [61] G. Pont, P. Cinnella, J.-C. Robinet, and P. Brenner, “Assessment of automatic hybrid RANS/LES models for industrial CFD,” in *32nd AIAA Applied Aerodynamics Conference*, p. 2691, 2014.
- [62] R. D. Sandberg, “Compressible-flow dns with application to airfoil noise,” *Flow, Turbulence and Combustion*, vol. 95, pp. 211–229, Oct 2015.
- [63] M. J. Lighthill, “On sound generated aerodynamically i. general theory,” *Proceedings of the Royal Society of London A: Mathematical, Physical and Engineering Sciences*, vol. 211, no. 1107, pp. 564–587, 1952.
- [64] K. S. Brentner and F. Farassat, “Modeling aerodynamically generated sound of helicopter rotors,” *Progress in Aerospace Sciences*, vol. 39, no. 2, pp. 83 – 120, 2003.
- [65] A. S. Lyrintzis, “Surface integral methods in computational aeroacoustics—from the (CFD) near-field to the (acoustic) far-field,” *International Journal of Aeroacoustics*, vol. 2, no. 2, pp. 95–128, 2003.

- [66] M. Wang, J. B. Freund, and S. K. Lele, “Computational prediction of flow-generated sound,” *Annual Review of Fluid Mechanics*, vol. 38, no. 1, pp. 483–512, 2006.
- [67] *Large-Eddy Simulation for Acoustics*. Cambridge Aerospace Series, Cambridge University Press, 2007.
- [68] J. F. Williams and D. L. Hawkings, “Sound generation by turbulence and surfaces in arbitrary motion,” *Philosophical Transactions of the Royal Society of London. Series A, Mathematical and Physical Sciences*, vol. 264, no. 1151, pp. 321–342, 1969.
- [69] P. di Francescantonio, “A new boundary integral formulation for the prediction of sound radiation,” *Journal of Sound and Vibration*, vol. 202, no. 4, pp. 491 – 509, 1997.
- [70] K. S. Brentner and F. Farassat, “Analytical comparison of the acoustic analogy and kirchhoff formulation for moving surfaces,” *AIAA journal*, vol. 36, no. 8, pp. 1379–1386, 1998.
- [71] W. Wolf, *Airfoil Aeroacoustics, LES and Acoustic Analogy Predictions*. PhD thesis, Stanford University, 2011.
- [72] D. P. Lockard and J. H. Casper, “Permeable surface corrections for fflowcs williams and hawkings integrals,” in *Proceedings of the 11th AIAA/CEAS Aeroacoustics Conference*, no. AIAA-2005-2995, 2005.
- [73] B. A. Singer, D. P. Lockard, and K. S. Brentner, “Computational aeroacoustic analysis of slat trailing-edge flow,” *AIAA journal*, vol. 38, no. 9, pp. 1558–1564, 2000.
- [74] B. Singer, D. Lockard, and G. Lilley, “Hybrid acoustic predictions,” *Computers & Mathematics with Applications*, vol. 46, no. 4, pp. 647 – 669, 2003. Turbulence Modelling and Simulation.
- [75] J. Casper, D. Lockard, M. Khorrami, and C. Streett, “Investigation of volumetric sources in airframe noise simulations,” in *10th AIAA/CEAS Aeroacoustics Conference*, p. 2805, 2004.

- [76] F. Souliez, L. Long, P. Morris, and A. Sharma, “Landing gear aerodynamic noise prediction using unstructured grids,” *International Journal of Aeroacoustics*, vol. 1, no. 2, pp. 115–135, 2002.
- [77] F. de la Puente, L. Sanders, and F. Vuillot, “On LAGOON nose landing gear CFD/CAA computation over unstructured mesh using a ZDES approach,” in *20th AIAA/CEAS Aeroacoustics Conference*, p. 2763, 2014.
- [78] H. Lai and K. H. Luo, “A three-dimensional hybrid LES-acoustic analogy method for predicting open-cavity noise,” *Flow, Turbulence and Combustion*, vol. 79, pp. 55–82, Jul 2007.
- [79] M. Wang, S. K. Lele, and P. Moin, “Computation of quadrupole noise using acoustic analogy,” *AIAA journal*, vol. 34, no. 11, pp. 2247–2254, 1996.
- [80] T. Ikeda, S. Enomoto, K. Yamamoto, and K. Amemiya, “Quadrupole corrections for the permeable-surface flows williams–hawkins equation,” *AIAA Journal*, pp. 2307–2320, 2017.
- [81] E. Turkel, “Preconditioning-squared methods for multidimensional aerodynamics,” in *13th Computational Fluid Dynamics Conference*, (Snowmass Village, CO, U.S.A.), American Institute of Aeronautics and Astronautics, June 1997.
- [82] M. A. Potsdam, V. Sankaran, and S. A. Pandya, “Unsteady low mach preconditioning with application to rotorcraft flows,” in *Proceedings of the 18th AIAA CFD Conference, Miami, FL*, 2007.
- [83] A. Crivellini, V. D’Alessandro, and F. Bassi, “A spalart–allmaras turbulence model implementation in a discontinuous galerkin solver for incompressible flows,” *Journal of Computational Physics*, vol. 241, pp. 388–415, May 2013.
- [84] A. Crivellini and V. D’Alessandro, “Spalart–allmaras model apparent transition and RANS simulations of laminar separation bubbles on airfoils,” *International Journal of Heat and Fluid Flow*, vol. 47, pp. 70–83, June 2014.
- [85] P. R. Spalart, S. Deck, M. L. Shur, K. D. Squires, M. K. Strelets, and A. Travin, “A new version of detached-eddy simulation, resistant to ambiguous grid den-

- sities,” *Theoretical and Computational Fluid Dynamics*, vol. 20, pp. 181–195, 2006.
- [86] L. Davidson, “Using isotropic synthetic fluctuations as inlet boundary conditions for unsteady simulations,” *Advances and Applications in Fluid Mechanics*, vol. 1, no. 1, pp. 1–35, 2007.
 - [87] L. Davidson, “Fluid mechanics, turbulent flow and turbulence modeling,” *Chalmers University of Technology, Goteborg, Sweden (Nov 2011)*, 2011.
 - [88] D. P. Lockard, “An efficient, two-dimensional implementation of the flowcs williams and hawkins equation,” *Journal of Sound and Vibration*, vol. 229, no. 4, pp. 897–911, 2000.
 - [89] OpenMP, “The OpenMP API specification for parallel programming.” <http://www.openmp.org>. Accessed: September-2017.
 - [90] A. Jameson, “Numerical solutions of the euler equations for compressible inviscid flows,” *Princeton University, MAE Report*, vol. 1643, 1983.
 - [91] A. Jameson, W. Schmidt, and E. Turkel, “Numerical solutions of the euler equations by finite volume methods using runge-kutta time-stepping schemes,” *AIAA paper*, vol. M, pp. 1–19, 1981.
 - [92] S. R. C. and T. Eli, “Multistage schemes with multigrid for euler and navier-stokes equations,” Tech. Rep. 3631, NASA Langley Research Center, Hampton, Virginia 23681-2199, August 1997.
 - [93] L. Martinelli, *Calculations of viscous flows with a multigrid method*. PhD thesis, Princeton Univ., NJ., 1987.
 - [94] J. Kok, “Extra-large eddy simulations using a high-order finite-volume scheme,” Tech. Rep. December, NL-TP-2007-800, 2007.
 - [95] P. Spalart and S. Allmaras, “A one-equation turbulence model for aerodynamic flows,” in *30th Aerospace Sciences Meeting and Exhibit*, Aerospace Sciences Meetings, American Institute of Aeronautics and Astronautics, Jan. 1992.

- [96] S. R. Allmaras and F. T. Johnson, “Modifications and clarifications for the implementation of the spalart-allmaras turbulence model,” in *ICCFD7-1902, Seventh International Conference on Computational Fluid Dynamics, Big Island, Hawaii*, 2012.
- [97] G.-c. Zha and C. Gables, “Delayed detached eddy simulation of a stall flow over NACA0012 airfoil using high order schemes,” *Proceedings of the 49th AIAA Aerospace Sciences Meeting including the New Horizons Forum and Aerospace Exhibition*, pp. 1–16, 2011.
- [98] S. Deck, “Zonal-detached-eddy simulation of the flow around a high-lift configuration,” *AIAA journal*, vol. 43, no. 11, pp. 2372–2384, 2005.
- [99] J. Riou, E. Garnier, S. Deck, and C. Basdevant, “Improvement of delayed-detached eddy simulation applied to separated flow over missile fin,” *AIAA Journal*, vol. 47, no. 2, pp. 345–360, 2009.
- [100] J. Riou, E. Garnier, and C. Basdevant, “Blowing effects on the separated flow over a moderately swept missile fin,” *AIAA journal*, vol. 49, no. 2, pp. 269–278, 2011.
- [101] S. Jee, O. Lopez, D. Brzozowski, A. Glezer, R. Moser, J. Pereira, A. Sequeira, and J. Pereira, “Delayed detached eddy simulation of aerodynamic controls with synthetic jets,” in *Proceedings of the 5th European Conference on Computational Fluid Dynamics*, 2010.
- [102] S. Jee, O. D. L. Mejia, R. D. Moser, J. A. Muse, A. T. Kutay, and A. J. Calise, “Simulation of rapidly maneuvering airfoils with synthetic jet actuators,” *AIAA journal*, vol. 51, no. 8, pp. 1883–1897, 2013.
- [103] A. K. Travin, M. L. Shur, P. R. Spalart, and M. K. Strelets, “Improvement of delayed detached-eddy simulation for les with wall modelling,” in *ECCOMAS CFD 2006: Proceedings of the European Conference on Computational Fluid Dynamics, Egmond aan Zee, The Netherlands, September 5-8, 2006*, Delft University of Technology; European Community on Computational Methods in Applied Sciences (ECCOMAS), 2006.

- [104] C. K. W. Tam, “Computational aeroacoustics : Issues and methods,” *AIAA Journal*, vol. 33, no. 10, 1995.
- [105] C. K. Tam, J. C. Webb, and Z. Dong, “A study of the short wave components in computational acoustics,” *Journal of Computational Acoustics*, vol. 1, no. 01, pp. 1–30, 1993.
- [106] W. De Roeck, W. Desmet, M. Baelmans, and P. Sas, “An overview of high-order finite difference schemes for computational aeroacoustics,” in *Proceedings of the International Conference on Noise and Vibration Engineering*, pp. 353–368, 2004.
- [107] A. Jameson, “Transonic flow calculations for aircraft,” in *Numerical Methods in Fluid Dynamics: Lectures given at the 3rd Centro Internazionale Matematico Estivo, 1983* (F. Brezzi, ed.), pp. 156–242, Berlin, Heidelberg: Springer Berlin Heidelberg, 1985.
- [108] A. Jameson, “Time dependent calculations using multigrid, with applications to unsteady flows past airfoils and wings,” *AIAA paper*, vol. 1596, p. 1991, 1991.
- [109] M.-S. Liou, A. Arnone, and L. Povinelli, “Multi-grid time-accurate integration of navier-stokes equations,” *AIAA paper*, pp. 93–3361, 1993.
- [110] N. D. Melson, H. L. Atkins, and M. D. Sanetrik, “Time-accurate navier-stokes calculations with multigrid acceleration,” in *The Sixth Copper Mountain Conference on Multigrid Methods*, 1993.
- [111] N. A. Pierce, *Preconditioned Multigrid Methods for Compressible Flow Calculations on Stretched Meshes*. PhD thesis, University of Oxford, 1997.
- [112] D. L. Darmofal and B. Van Leer, “Local preconditioning: Manipulating mother nature to fool father time,” *Computing the Future II: Advances and Prospects in Computational Aerodynamics*, vol. 30, 1998.
- [113] S. Venkateswaran and C. Merkle, “Dual time-stepping and preconditioning for unsteady computations,” in *33rd Aerospace Sciences Meeting and Exhibit*, Aerospace Sciences Meetings, American Institute of Aeronautics and Astronautics, Jan. 1995.

- [114] E. Turkel and V. N. Vatsa, “Local preconditioners for steady and unsteady flow applications,” *ESAIM: Mathematical Modelling and Numerical Analysis*, vol. 39, no. 03, pp. 515–535, 2005.
- [115] E. Turkel, “Preconditioned methods for solving the incompressible and low speed compressible equations,” *Journal of computational physics*, vol. 72, no. 2, pp. 277–298, 1987.
- [116] J. M. Weiss and W. A. Smith, “Preconditioning applied to variable and constant density flows,” *AIAA journal*, vol. 33, no. 11, pp. 2050–2057, 1995.
- [117] K. Hosseini, *Practical Implementation Of Robust Preconditioners For Optimized Multistage Flow Solvers*. PhD thesis, Stanford University, 2005.
- [118] Y. Colin, H. Deniau, and J.-F. Boussuge, “A robust low speed preconditioning formulation for viscous flow computations,” *Computers & Fluids*, vol. 47, no. 1, pp. 1–15, 2011.
- [119] R. Djeddi, J. Howison, and K. Ekici, “A fully coupled turbulent low-speed preconditioner for harmonic balance applications,” *Aerospace Science and Technology*, vol. 53, pp. 22–37, 2016.
- [120] S. Allmaras, “Analysis of a local matrix preconditioner for the 2-d navier-stokes equations,” *AIAA paper*, vol. 3330, p. 1993, 1993.
- [121] N. A. Pierce and M. B. Giles, “Preconditioned multigrid methods for compressible flow calculations on stretched meshes,” *Journal of Computational Physics*, vol. 136, no. 2, pp. 425–445, 1997.
- [122] E. Turkel, “Preconditioning techniques in computational fluid dynamics,” *Annual Review of Fluid Mechanics*, vol. 31, no. 1, pp. 385–416, 1999.
- [123] A. Lerat, “Une classe de schémas aux différences implicites pour les systèmes hyperboliques de lois de conservation,” *Comptes Rendus Acad. Sciences Paris*, vol. 288, 1979.
- [124] A. Jameson, “The evolution of computational methods in aerodynamics,” *Journal of Applied Mechanics*, vol. 50, no. 4b, pp. 1052–1070, 1983.

- [125] J. Blazek, *Computational Fluid Dynamics: Principles and Applications*. Elsevier, 2005.
- [126] P. Cook, M. Firmin, and M. McDonald, “Airfoil RAE 2822: pressure distributions, and boundary layer and wake measurements,” tech. rep., AGARD AR 138, 1979.
- [127] Y. Ozyoruk and L. Long, “Progress in time-domain calculations of ducted fan noise: Multigrid acceleration of a high-resolution caa scheme,” in *2nd AIAA/CEAS, Aeroacoustics Conference*, no. 1771, (State College, PA), American Institute of Aeronautics and Astronautics, May 1996.
- [128] N. Villedieu, T. Quintino, M. Vymazal, and H. Deconinck, “High order residual distribution schemes based on multidimensional upwinding,” in *ADIGMA - A European Initiative on the Development of Adaptive Higher-Order Variational Methods for Aerospace Applications*, vol. 113 of *Notes on Numerical Fluid Mechanics and Multidisciplinary Design*, pp. 129–143, Springer Berlin Heidelberg, 2010.
- [129] U. Ghia, K. Ghia, and C. Shin, “High-Re solutions for incompressible flow using the navier-stokes equations and a multigrid method,” *Journal of Computational Physics*, vol. 48, pp. 387–411, 1982.
- [130] N. L. R. Center, “Turbulence modeling resource.” http://turbmodels.larc.nasa.gov/flatplate_sa.html. Accessed: August-2014.
- [131] F. White, *Viscous fluid flow*. New York, NY: McGraw-Hill Higher Education, 1974.
- [132] C. J. Roy, “Review of code and solution verification procedures for computational simulation,” *Journal of Computational Physics*, vol. 205, pp. 131–156, May 2005.
- [133] P. Knupp, *Verification of computer codes in computational science and engineering*. Boca Raton, Fla: Chapman & Hall/CRC, 2003.
- [134] S. P. Veluri, C. J. Roy, and E. A. Luke, “Comprehensive code verification techniques for finite volume CFD codes,” *Computers & Fluids*, vol. 70, pp. 59–72, Nov. 2012.

- [135] S. F. Hoerner, *Fluid-dynamic drag : practical information on aerodynamic drag and hydrodynamic resistance*. Hoerner Fluid Dynamics, 1965.
- [136] H.-S. Im and G.-C. Zha, “Delayed detached eddy simulation of airfoil stall flows using high-order schemes,” *Journal of Fluids Engineering*, vol. 136, no. 11, p. 111104, 2014.
- [137] A. A. Wray, “Unpublished DNS data. available on agard database.” <http://torroja.dmt.upm.es/turbdata/agard/>, 1997.
- [138] R. Moser, J. Kim, and N. Mansour, “A selection of test cases for the validation of large eddy simulations of turbulent flows,” tech. rep., AGARD-AR-345, 1998.
- [139] G. Comte-Bellot and S. Corrsin, “Simple eulerian time correlation of full-and narrow-band velocity signals in grid-generated, ‘isotropic’ turbulence,” *Journal of Fluid Mechanics*, vol. 48, no. 02, pp. 273–337, 1971.
- [140] R. D. Moser, J. Kim, and N. N. Mansour, “Direct numerical simulation of turbulent channel flow up to $Re = 590$,” *Physics of Fluids*, vol. 11, no. 4, pp. 943–945, 1999.
- [141] J. Meyers and P. Sagaut, “Is plane-channel flow a friendly case for the testing of large-eddy simulation subgrid-scale models?,” *Physics of Fluids (1994-present)*, vol. 19, no. 4, p. 048105, 2007.
- [142] U. Piomelli and E. Balaras, “Wall-layer models for large-eddy simulations,” *Annual Review of Fluid Mechanics*, vol. 34, no. 1, pp. 349–374, 2002.
- [143] F. Hamba, “A hybrid RANS/LES simulation of turbulent channel flow,” *Theoretical and Computational Fluid Dynamics*, vol. 16, pp. 387–403, May 2003.
- [144] P. Wu and J. Meyers, “A constraint for the subgrid-scale stresses in the logarithmic region of high reynolds number turbulent boundary layers: A solution to the log-layer mismatch problem,” *Physics of Fluids*, vol. 25, no. 1, 2013.
- [145] N. V. Nikitin, F. Nicoud, B. Wasistho, K. D. Squires, and P. R. Spalart, “An approach to wall modeling in large-eddy simulations,” *Physics of Fluids*, vol. 12, no. 7, pp. 1629–1632, 2000.

- [146] F. Farassat, “Linear acoustic formulas for calculation of rotating blade noise,” *AIAA journal*, vol. 19, no. 9, pp. 1122–1130, 1981.
- [147] D. Lockard, “A comparison of fflowcs williams-hawkings solvers for airframe noise applications,” in *8th AIAA/CEAS Aeroacoustics Conference*, no. 2580, (Breckenridge, CO), American Institute of Aeronautics and Astronautics, June 2002.
- [148] P. Welch, “The use of fast fourier transform for the estimation of power spectra: A method based on time averaging over short, modified periodograms,” *IEEE Transactions on Audio and Electroacoustics*, vol. 15, pp. 70–73, June 1967.
- [149] C. Kato, A. Iida, Y. Takano, H. Fujita, and M. Ikegawa, “Numerical prediction of aerodynamic noise radiated from low mach number turbulent wake,” in *31st Aerospace Sciences Meetings*, American Institute of Aeronautics and Astronautics, Jan 1993.
- [150] J. H. Seo and Y. J. Moon, “Aerodynamic noise prediction for long-span bodies,” *Journal of Sound and Vibration*, vol. 306, no. 3, pp. 564 – 579, 2007.
- [151] F. Pérot, X. Gloerfelt, C. Bailly, J.-M. Auger, and H. Giardi, “Numerical prediction of the noise radiated by a cylinder,” in *9th AIAA/CEAS Aeroacoustics Conference and Exhibit*, p. 3240, 2003.
- [152] Y. Moon, J. Seo, Y. Bae, M. Roger, and S. Becker, “A hybrid prediction method for low-subsonic turbulent flow noise,” *Computers & Fluids*, vol. 39, no. 7, pp. 1125 – 1135, 2010.
- [153] M. Roger, S. Moreau, and A. Guédel, “Vortex-shedding noise and potential-interaction noise modeling by a reversed sears’ problem,” in *Proceedings of the 12th AIAA/CEAS Aeroacoustics Conference and Exhibit*, pp. 8–10, 2006.
- [154] J. G. Kocheemoolayil, *Large eddy simulation of airfoil self-noise*. PhD thesis, Stanford University, 2016.

APPENDIX A

VARIABLE TRANSFORMATIONS

In most of the compressible flow formulations, conservative variables are used in the governing equations. For example in derivation and implementation of preconditioning, use of some other variable set might be a great convenience. In those cases, transformations of variables back and forth is necessary. The following variable sets are considered currently,

$$dW = \begin{Bmatrix} d\rho \\ d(\rho u) \\ d(\rho v) \\ d(\rho w) \\ d(\rho E) \end{Bmatrix}, \quad dW_p = \begin{Bmatrix} dp \\ du \\ dv \\ dw \\ dT \end{Bmatrix}, \quad dW_e = \begin{Bmatrix} dp/\rho c \\ du \\ dv \\ dw \\ dp - c^2 d\rho \end{Bmatrix} \quad (\text{A.1})$$

, i.e. conservative, primitive and entropy variables in differential form, respectively. Note that the conservative variables $W = [\rho, \rho u, \rho v, \rho w, \rho E]$ in the governing equations are nondimensionalized, with respect to $\rho_\infty, \rho_\infty u, \rho_\infty v, \rho_\infty w$ and $\rho_\infty c_\infty^2$.

Transformation of a vector V from one variable set to another, say a to b is simply,

$$V_b = \frac{\partial W_b}{\partial W_a} V_a \quad (\text{A.2})$$

Likewise, b to a will be

$$V_a = \frac{\partial W_a}{\partial W_b} V_b \quad (\text{A.3})$$

where

$$\frac{\partial W_a}{\partial W_b} = \left(\frac{\partial W_b}{\partial W_a} \right)^{-1} \quad (\text{A.4})$$

It can also be shown that transformation of a matrix M is performed as [117]

$$M_b = \frac{\partial W_b}{\partial W_a} M_a \frac{\partial W_a}{\partial W_b} \quad (\text{A.5})$$

In dimensionless form of variables of the current work, following transformations are used:

$$\frac{\partial W}{\partial W_e} = \left(\frac{\partial W_e}{\partial W} \right)^{-1} = \begin{pmatrix} \frac{\rho}{c} & 0 & 0 & 0 & -\frac{1}{c^2} \\ \frac{\rho u}{c} & \rho & 0 & 0 & -\frac{u}{c^2} \\ \frac{\rho v}{c} & 0 & \rho & 0 & -\frac{v}{c^2} \\ \frac{\rho w}{c} & 0 & 0 & \rho & -\frac{w}{c^2} \\ \frac{\rho}{c} \left(\frac{q^2}{2} + \frac{c^2}{\gamma-1} \right) & \rho u & \rho v & \rho w & -\frac{q^2}{2c^2} \end{pmatrix} \quad (\text{A.6})$$

$$\frac{\partial W_p}{\partial W_e} = \left(\frac{\partial W_e}{\partial W_p} \right)^{-1} = \begin{pmatrix} \rho c & 0 & 0 & 0 & 0 \\ 0 & 1 & 0 & 0 & 0 \\ 0 & 0 & 1 & 0 & 0 \\ 0 & 0 & 0 & 1 & 0 \\ c(\gamma-1) & 0 & 0 & 0 & \frac{1}{\rho} \end{pmatrix} \quad (\text{A.7})$$

where $q^2 = u^2 + v^2 + w^2$. In dimensionless form, square of sound speed becomes

$$c^2 = T = \gamma \frac{p}{\rho} \quad (\text{A.8})$$

CURRICULUM VITAE

PERSONAL INFORMATION

Surname, Name: Cengiz, Kenan

Nationality: Turkish (TC)

Date and Place of Birth: 08.02.1984, Aydın

e-mail: kcengiz@ae.metu.edu.tr

EDUCATION

Degree	Institution	Year of Graduation
M.S.	Aerospace Eng. Dept. of METU	2010
B.S.	Aerospace Eng. Dept. of METU	2007
High School	Aydın Adnan Menderes Anadolu Lisesi	2002

PROFESSIONAL EXPERIENCE

Year	Place	Enrollment
2018 -	InnoVita Engineering Ltd.	CFD Analyst, flight model developer
2017	Aerotim Engineering Ltd.	CFD Analyst
2014-2016	Aerospace Eng. Dept. of METU	Scholarship-funded research assistant
2007-2014	Aerospace Eng. Dept. of METU	Research assistant

PUBLICATIONS

Journal Publications

Kenan Cengiz, Yusuf Özyörük, *Experiences with Two Detached Eddy Simulation Approaches through use of a High-order Finite Volume Solver*, Journal of Turbulence (under review)

Özgür Yalçın, Kenan Cengiz, Yusuf Özyörük, *High-order Detached Eddy Simulation of Unsteady Flow Around NREL S826 Airfoil*, Journal of Wind Engineering & Industrial Aerodynamics (accepted)

Conference Publications

Özgür Yalçın, Kenan Cengiz, and Yusuf Özyörük. *Shear-layer-adapted delayed detached-eddy simulation of a transonic open cavity flow*, In *Ankara International Aerospace Conference*, pages AIAC–2017–114, Ankara, September 2017.

Kenan Cengiz and Yusuf Özyörük, *Numerical Prediction of DU96 Airfoil Trailing-edge Noise using Detached-eddy Simulation*, In *Wind Energy Science Conference*, Technical University of Denmark, Lyngby, June 2017.

Kenan Cengiz and Yusuf Özyörük, *Detached Eddy Simulation Using A High-Order Low-Dissipation Low-Dispersion Computational Method For Aeroacoustic Purposes*, In *Ankara International Aerospace Conference*, pages AIAC–2015–043, Ankara, September 2015.

Kenan Cengiz and Yusuf Özyörük, *Rüzgar Türbini Aeroakustiği Benzetimi Maksadıyla Yüksek Doğruluklu Üç Boyutlu Navier-Stokes Kodu Geliştirilmesi*, In *Ulusal Havacılık ve Uzay Kongresi*, number 101, Kayseri, 2014.

Kenan Cengiz and Yusuf Özyörük, *Development of a navier-stokes solver for high-fidelity simulation of wind turbine noise*, In *7th Ankara International Aerospace Conference*, number 040, Ankara, September 2013.

Kenan Cengiz and Yusuf Özyörük, *A Helmholtz-type Numerical Simulation of Thermo-*

acoustic Instabilities in a 3-D Rijke Tube. In *49th AIAA/ASME/SAE/ASEE Joint Propulsion Conference*, number 4060, San Jose, CA, July 2013. American Institute of Aeronautics and Astronautics.

Kenan Cengiz and Yusuf Özyörük, *Development of a linear combustion instability tool for 3-d liquid-propellant engine geometries*, In *6th Ankara International Aerospace Conference*, number 32, Ankara, September 2011.

Kenan Cengiz and Yusuf Özyörük, *Doğrusal Yanma Kararsızlığı için Sayısal Analiz Programı Geliştirilmesi*, In *Ulusal Havacılık ve Uzay Kongresi*, number 094, Eskişehir, 2010.